UNIVERSITY OF CALIFORNIA SAN DIEGO

Measuring and Controlling Metabolic Heat in Biological Systems

A dissertation submitted in partial satisfaction of the requirements
for the degree Doctor of Philosophy

in

Materials Science and Engineering

by

Sahngki Hong

Committee in charge:

Professor Renkun Chen, Chair
Professor Ratneshwar Lal
Professor Christian Metallo
Professor Donald Sirbuly
Professor Sheng Xu

2018

Copyright

Sahngki Hong, 2018

All rights reserved.

The Dissertation of Sahngki Hong is approved, and it is acceptable in quality and form for publication on microfilm and electronically:

_____

_____

_____

_____

_____
Chair

University of California San Diego

2018

DEDICATION

Dedicated to my family for their unconditional love and supports.

TABLE OF CONTENTS

Signature Page..... iii

Dedication..... iv

Table of Contents..... v

List of Figures..... viii

Acknowledgements..... x

Vita..... xi

Abstract of the Dissertation..... xii

Chapter 1 Fundamentals of Heat in Living Organism..... 1

1.1 Introduction..... 1

1.2 Metabolic Heat Production of Living Organisms..... 2

1.3 Characterization of Cellular Heat Production by Calorimetry..... 5

1.4 Thermoregulation of Human Body..... 8

1.5 Indoor Climate Control and Personal Thermoregulation..... 10

1.6 Thesis Structure..... 11

Chapter 2 Wearable Thermoelectrics for Personalized Thermoregulation..... 14

2.1 Introduction..... 14

2.2 Design, Fabrication, and Characterization of Flexible TED..... 17

2.3 Power Generation Performance of Flexible TED..... 29

2.4 Cooling and Heating Performance of Flexible TED on Simulated Heater 32

2.5 Thermoregulation on Human Skin using Flexible TED..... 38

2.6 Integration of TED with Flexible Batteries for Mobile Thermoregulation 43

2.7 Materials and Methods..... 46
2.7.1 Fabrication of Flexible TED..... 46
2.7.2 Thermoelectric Characterization of TED..... 47
2.7.3 Measurement of Cooling/heating Performance of TED..... 47
2.7.4 Measurement of TED Performance on Human Subject..... 50
2.7.5 Fabrication of Flexible Battery Pack..... 50
2.7.6 Demonstration of Mobile Application of TED with Flexible Battery Pack..... 52
2.8 Conclusion..... 53
Chapter 3 Wearable Thermoelectrics for Thermal Camouflage..... 54
3.1 Introduction..... 54
3.2 Design..... 56
3.3 Active Thermal Camouflage..... 59
3.4 Anti-IR Reflection Property..... 62
3.5 Thermal Camouflage on Human Skin..... 64
3.6 Conclusion..... 67
Chapter 4 Single-cell Calorimetry..... 68
4.1 Introduction..... 68
4.2 Development of High-sensitivity Single-cell Calorimeter..... 72
4.3 Single-cell Trapping and Nutrient Supply..... 81
4.4 Single-cell Measurement Rate Measurement Results..... 87
4.5 Conclusion..... 92

4.6 Future Work: Investigation of Brown Adipocytes..... 93

Chapter 5 Conclusion..... 96

Reference..... 98

LIST OF FIGURES

Figure 2.1	TED design and fabrication process	23
Figure 2.2	Fabrication and characterization of TED	24
Figure 2.3	Optimization of the TED	25
Figure 2.4	Characterization of the TED	26
Figure 2.5	COMSOL modeling of the TED cooling effect	27
Figure 2.6	Power generation of the TED and its impact on active cooling	31
Figure 2.7	Cooling and heating performance	36
Figure 2.8	Comparison of TEDs	37
Figure 2.9	Demonstration of thermoregulation on human skin	41
Figure 2.10	Power consumption during the thermo-regulation of human skin	42
Figure 2.11	Temperature change during the mobile thermoregulation demonstration	45
Figure 2.12	PID control of the heat flux from the heater	49
Figure 3.1	A concept of thermal camouflage by the flexible TED	58
Figure 3.2	Active thermal camouflage by the TED	61
Figure 3.3	Anti-reflection property of the TED	63
Figure 3.4	Thermal camouflage on human skin	66
Figure 4.1	Design of the single-cell calorimeter and measurement platform	78
Figure 4.2	Thermal and mechanical modeling of the calorimeter for design optimization	79
Figure 4.3	Baseline stability and sensitivity of the calorimeter	80

Figure 4.4 Magnetic cell trapping and single-cell measurement..... 85

Figure 4.5 Oxygen consumption of *Tetrahymena* in microfluidic channel without flow..... 86

Figure 4.6 The influence of fluid flow and cell position on the calorimeter sensitivity..... 87

Figure 4.7 Metabolic rate measurement results..... 94

ACKNOWLEDGEMENTS

I would like to thank my advisor Prof. Renkun Chen, group members, friends, and family for all the supports and advices.

Chapter 2, in full, has been submitted for publication of the material, Sahngki Hong, Yue Gu, Joon Kyo Seo, Joseph Wang, Ping Liu, Y. Shirley Meng, Sheng Xu and Renkun Chen. The dissertation author was the primary investigator and the first author of this paper.

Chapter 3, in full, is currently being prepared for submission, Sahngki Hong and Renkun Chen. The dissertation author was the primary investigator and the first author of this paper.

Chapter 4, in full, is currently being prepared for submission, Sahngki Hong, Edward Dechaumphai, Courtney Green, Ratneshwar Lal, Christian Metallo and Renkun Chen. The dissertation author was the primary investigator and the first author of this paper.

Sahngki Hong

San Diego, CA

Dec, 2018

VITA

2002	Bachelor of Science, Korea University
2009	Master of Science, Korea University
2018	Doctor of Philosophy, University of California San Diego

FIELD OF STUDY

Major Field: Engineering

Studies in Materials Science and Engineering

Professor Renkun Chen

ABSTRACT OF DESERTATION

Measuring and Controlling Metabolic Heat in Biological Systems

by

Sahngki Hong

Doctor of Philosophy in Materials Science and Engineering

University of California San Diego, 2018

Professor Renkun Chen, Chair

Heat is one of the most important aspects of living organisms. Metabolic heat production and evaporative heat dissipation protect warm-blooded animals from adverse weather conditions. Heat management devices provide thermal comfort to human by climate control or thermal camouflage effect by blocking heat emission from the human body. Further, metabolism in living organisms can be investigated by monitoring heat signature because the metabolic heat production represents the overall enthalpy change during metabolic reactions in organisms. This dissertation presents two state-of-the-art devices and demonstrates their

applications: 1) a wearable thermoelectric device (TED) for personal thermoregulation and camouflage, and 2) high-resolution calorimeter for measurement of single-cell metabolic heat generation.

Personalized cooling/heating by TEDs can drastically reduce energy consumption with small cooling volume, meet individual cooling needs and camouflage heat emission from the human body. However, a TED with sufficient flexibility and temperature regulation performance has yet to be realized because of lack of optimization of the thermal and mechanical design. In the first part of the dissertation, we demonstrated a wearable TED that can deliver over 10 °C cooling effect with a high coefficient of performance (COP>1.5). Our TED is the first to achieve long-term active cooling with high flexibility, thanks to a novel design of double elastomer layers embedding an air gap insulation and high-ZT rigid TE pillars. The TED was also applied to thermal camouflage using the large temperature regulation window, which enables to match the heat signature of human body with background temperature.

The last part of the dissertation focuses on fundamental study of cellular metabolism using direct calorimetry techique. We developed high-resolution calorimeter sufficient to measure heat generation from a single cell for investigation of heterogeneous metabolic activities. This non-invasive and label-free calorimetry technic is optimized to study the cell metabolic heat production without alter the nature of cells. Our single-cell calorimeter achieved the power resolution as low as 0.6 nW using the innovative one-dimensional microfluidic tube design. Single-cell measurements using the calorimeter revealed that the relationship between metabolic rate and cell size of individual *Tetrahymena* follows the allometric scaling relationship.

Chapter 1

Fundamentals of Heat in Living Organisms

1.1 Introduction

Living organisms produce heat as a biproduct of metabolism and manage the body temperature by thermoregulation. Failure of heat management such as fever, hyperthermia, or hypothermia causes serious damages on living organisms; therefore, understanding of heat in living organisms is imperative[1]. Cellular metabolic heat generation represents the overall enthalpy change of metabolic reactions and contains useful information that cannot be provided by other metabolic products such as oxygen or carbon dioxide[2,3]. Direct calorimetry technique can measure this metabolic heat generation using thermally insulative reaction chamber and sensitive thermometer; however, the caloritmery platform that can measure heterogenous metabolic heat generation by individual cells has not been demonstrated yet because of the large parasitic heat loss and small heat generation from a single cell[4].

While this basal heat production is mainly caused by cellular metabolism, muscle activity, nonshivering thermogenesis, and thermogenic effect of food also result heat generation in organisms[5]. Most of the metabolic heat is generated in the deep organs, transferred to the skin, and eventually dissipated to surroundings. The thermal management system in human body can control this heat transfer/dissipation process using blood circulation or sweating to maintain the body core temperature[6]. However, although the human

body can manage the thermal condition in a wide range of ambient temperature, the thermal load for cooling or heating make human unpleasant. Thus, it is not surprising that the climate control such as heating, ventilation, and air conditioning account for more than 10% of overall energy consumed in US, which is equivalent to per capita energy consumption of ~1.5 kW[7]. Personalized climate control system may unlock the new possibility of saving tremendous amount of energy and meet the individuals' thermal needs; however, wearable thermal management system with sufficient cooling performance has yet to be developed.

This chapter describes the fundamental background of heat in living organisms in many aspects including cellular metabolism, metabolic heat production, thermoregulation of the human body, indoor climate control, and personal thermoregulation. The goal of this chapter is to provide a brief introduction of the motivations of my research in the wearable thermoelectric devices for personal thermoregulation and single-cell calorimeter for investigation of cellular metabolic heat generation.

1.2 Metabolic Heat Production of Living Organisms

In cellular metabolism, various metabolic pathways produce energy and materials which are essential for living organisms. When oragnisms ingest foods, glycolysis metabolizes glucose to pyruvate, and the pyruvate is completely oxidized to CO_2 in the presence of oxygen or converted to lactate when oxygen is limited. These two metabolic pathways called aerobic and anaerobic metabolism and play an important role in living organisms. Aerobic metabolism involves oxidative phosphorelation in mitochondria. During the oxidative phosphorelation, electrons are harvested from the oxidizable substrates and

transported through the electron transport chain, and this process eventually pump protons from mitichondiral matrix to the intermembrane space to generate proton gradient across the inner membrane. This proton gradient operates various cellular processes including ATP synthesis[8]. On the other hand, when oxygen is limited, the oxidative phosphorylation cannot take place. However, even under the condition, energy can still be produced by glycolysis because the metabolic reactions for the breakdown of glucose to pyruvate do not require oxygen. When the quantities of pyruvate and NADH (reduced nicotinamide adenine dinucleotide), another end product of the glycolytic reaction, begin to be excessive, these two products react with each other to form lactate, and the major portion of the pyruvate is converted to lactate under anaerobic conditions. This anaerobic metabolism is extremely inefficient; only 2 molecules of ATPs can be produced by one molecule of glucose in anaerobic metabolism while aerobic oxidative phosphorylation generates up to 36 molecules of ATPs with complete oxidation of one glucose molecule[9].

These metabolic reactions involve enthanlpy changes, which cause heat production; for example, the oxidation of glucose to CO_2 produces the heat of -2,803 kJ mol^{-1} [5]. Especially, mitochondrial respiration including the oxidative phosphorylation and proton leak through the inner membrane of mitochondria generation considerable amount of heat. The enthalpy caused by NADH combustion for proton pumping is approximately -250 kJ $molO^{-1}$, potential heat generation the proton gradient is about 150 kJ $molO^{-1}$, and the enthalpy of hydrolysis of synthesized ATP through the proton gradient is -40 kJ $molO^{-1}$. All the enthalpy changes during the reactions is dissipated as heat. ~80% of heat production in living organisms is estimated by these proton-related metabolic reactions including pump and transport. This heat production process related to the mitochondrial activity dominates the overall metabolic

rate when oragnisms are under resting conditions, and it called basal metabolic rate. In humans, the basal metabolic rate is about 58 W m^{-2}. The metabolic heat generation largely depends on the physical and thermal conditions of organisms; the heat production while the subject carries out normal daily activities may be 1.5–2.1 times higher than the basal metabolic rate[10].

The majority of this enhanced metabolic rate is caused by the activity of muscles, nonshivering thermogenesis, and the thermogenic effect of food. The muscle activity can increase the metabolic rate by 10 times compared to the basal metabolic rate during exercise. During this metabolism, the muscles consume extra oxygen to meet the large energy needs for contractions and generate more heat. In addition to the heat generation by metabolic reaction, the muscle activity causes the heat by frictions itself, and this friction also used by shivering thermogenesis to increase body temperature under cold environment. After the long period of the cold exposure, this shivering thermogenesis is gradually reduced and replaced by nonshivering thermogenesis. The nonshivering thermogenesis mainly occurs in brown fat cells. These cells untilize uncoupling protein to generate proton leak on the inner membrane of mitochondria, which uncouples the proton transport from ATP synthesis, and enhanced oxidative phosphorelation process to recover the reduced proton gradient causes maximal metabolic heat generation[11]. Lastly, feeding can stimulate the metabolic heat generation by ~25%. The mechanism of this heat generation include the stimulated ATP synthesis using the ingested food, hormonal changes, and temporal synthesis of storage compounds[5].

1.3 Characterizaiton of Cellular Heat Production by Calorimetry

The heat production by cellular metabolism represents the overall enthalpy change of all metabolic reactions while oxygen uptake or carbon dioxide emission only represent specific metabolism such as aerobic respiration. Thus, it provides valuable information that other techniques do not; for instance, anaerobic metabolism that does not consume oxygen can be characterized by comparing oxygen consumption rate and heat production. This oxycaloric equivalent (ratio of oxygen consumption rate and heat production) has theoretically -430 – -480 kJ $molO_2^{-1}$ based on the assumption that anaerobic metabolism is negligible[2], and provide the anaerobic contribution to the overall metabolic rate.

The heat generation by cellular metabolism can be directly measured by calorimetry technique, which measures temperature change of thermally isolated reaction chamber by metabolic heat generation of cells. The energy balance equation of a calorimeter can be defined as

$$V\Delta H\frac{dc}{dt} - G\Delta T = C\frac{d\Delta T}{dt}, \tag{1.1}$$

where V is chamber volume, ΔH is enthalpy of reaction, c is concentration of the reactant, t is time, G is thermal conductance between the chamber and a thermal reservoir, ΔT is temperature change due to the reaction, and C is heat capacity. For a steady-state condition with metabolic heat from a single cell (Q_{cell}), the energy balance equation can be simplified to

$$Q_{cell} = G\Delta T. \tag{1.2}$$

To measure the metabolic rate of cells, the sensitivity of the calorimeter (Q_s) must be smaller than Q_{cell}, which is in the range from a few picowatts to a few nanowatts. Q_s is dependant on the device conductance G and the minimum detectable temperature change (ΔT_{min}):

$$Q_s = G\Delta T_{min}. \tag{1.3}$$

Therefore, minimizing both G and ΔT_{min} is imperative to achieve better sensitivity.

Reduction of the thermal conductance involves minimization of three heat transfer modes: conduction (G_{cond}), convection (G_{conv}), and radiation (G_{rad}) heat losses. Assuming that there is a microflulidics-based calorimeter, from the point of view of heat conduction alone, conduction heat loss of the device can be minimized by using a suspended microfluidic tube structure because the structure maximized the cross-sectional area (A_c) to half tube length (L) ratio. The fluids and cells to transport put constraints on the cross-sectional area of the microfluidic tubes; hence restricted optimization to mainly material selection of the device. However, the longer microfluidic length increases the surface area of the devices and resulted in higher heat loss due to convection and radiation heat transfer. Such competing heat transfer modes put limitation on the parasitic heat loss that can be minimized. On the basis of suspended microfluidic structures under high vacuum assuming cells act as a point heat source, the heat loss from the biocalorimeter can be simplified using fin equation as followed: (see Chapter 4 for details)

$$G = 2mkA_c\left(\frac{e^{mL} + e^{-mL}}{e^{mL} - e^{-mL}}\right), \tag{1.4}$$

where $m = \sqrt{\frac{hP}{kA_c}}$, k is the effective thermal conductivity, P is the parameter of the microfluidic tube, and h is the effective radiation heat transfer coefficient ($h = 4\varepsilon\sigma T_{avg}^3$, where

ε is the effective emissivity). The calometer is then can be optimized to minimize parasitic heat loss based on the relationships between dimensions (length and cross-sectional area), emissivity, and thermal conductivity of the device shown in Eq. 1.4.

On the other hand, the ΔT_{min} relies on sensitivity of the thermometer, electrical noise, and temperature drift. The most sensitive and widely used thermometer is a thermopile that uses Seebeck effect to convert temperature signal to voltage signal. The high sensitivity of the thermopile can be achieved by using the materials with high Seebeck coefficient (S) and increasing number of junctions (n). However, it is worth to note that there is an optimum n for the best Q_s since exploiting more junctions will increase not only the sensitivity of the thermopile but also the conduction heat loss through the thermopile. In addition, the many junctions inevitably increase the electrical resistance of the thermopile that results large electrical noise. The electrical noise (V_n) composed of Johnson noise ($V_{n,Johnson}$), flicker noise ($V_{n,flicker}$), and amplifier noise ($V_{n,amp}$):

$$V_n = V_{n,Johnson} + V_{n,flicker} + V_{n,amp}. \quad (7)$$

The Johnson noise, which is thermal agitation of electrons, is proportional to the square root of the electrical resistance ($V_{n,johnson} = \sqrt{4k_B TR\Delta f}$, where k_B is Boltzmann constant, T is temperature, R is electrical resistance, and Δf is bandwidth). The flicker noise (1/f noise) in resistors is known as originating from charge trapping/detrapping or carrier mobility fluctuation and proportional to the electrical resistance[12]. The flicker noise increases at low frequency and is inevitable for DC measurement. The amplifier noise is generated by the amplifier during amplifying the voltage signal from the thermopile. Since the three noises

are a function of Δf, low-pass filter which filters high frequency noise and truncates the bandwidth can reduce the noise as well as eliminates the 60 Hz noise from the power sources.

1.4 Thermoregulation of Human Body

Human body has beautifully designed temperature control system, which allow a naked person to maintain the body core temperature within 36–38 °C at ambient temperature ranging from 13 °C to 54 °C. In principal, heat production in human body is a by-product of metabolism, and majority of heat is produced from the organs deep inside of human body and transferred to the skin. Hence, the heat loss of human body can be determined by heat conduction rate from the body core to the skin as well as heat dissipation rate from the skin to the ambient. The heat conduction rate from the body core to the skin is mainly controlled by blood circulation through blood vessels. As a result of the blood flow rate control, the heat conductance through skin can be changed by ~8 times from vasoconstricted to vasodilated condition[1]. The effective thermal conductivity of human tissue including the blood circulation has a maximum value of 2.8 W m^{-1} K^{-1} at hot condition and minimum value of 0.3 W m^{-1} K^{-1} at cold condition[13]. On the other hand, the heat dissipation from the skin to ambient including radiation heat loss (54–60%), convection heat loss (~25%), evaporation of sweat (~7%), and breathing (~14%). Among the heat loss mechanism, human body can control the evporation by regulating sweat rate in the range from 0.3 to 12.0 mL min^{-1}. This evaporation heat loss dissipates 0.58 kcal for each gram of evaporated sweat. While the human skin and breathing evaporate 600–700 mL of sweat per day, which is equivalent to

~10 W m^{-2} of heat loss, under a typical resting condition, the heat loss by evaporation of sweat can be increased up to ~250 W m^{-2} during very heavy activity.

These blood flow and sweat rate is controlled by nervous feedback mechanisms and temperature-regulating centers placed in the hypothalamus to maintain body temperature constant. The hypothalamic preoptic area detects temperature by large numbers of heat- and cold-sensitive neurons; also, temperature receptors in the skin detects temperature. The hypothalamic temperature centers regulate the body temperature using these temperature signals. When the hypothalamic temperature centers perceive high temperature, the human body increase blood flow and sweat rate and decrease heat production. When the control system detects low temperature, on the other hand, the human body response opposite way: suppress the blood flow and sweat rate and increase heat production by shivering and nonshivering thermogenesis.

Despite of this self-thermoregulation system in human body, there is a range of environmental conditions that human feel comfortable. The comfortable air temperature for a naked human ranging from 26–29 °C and the corresponding skin temperature is around 32–34 °C[14,15] depending on metabolic rate, humidity and body parts. The thermal sensation and comfortness of human body can be estimated with predicted mean vote index (PMV) and predicted percentage dissatisfied index (PPD), respectively. The PMV index can predicts the response of a people to a certain environment condition using the seven points ASHRAE (American Society of Heating, Refrigerating and Air conditioning Engineers) thermal sensation scale, which scales the thermal sensation from a level -3 to +3, representing from cold to hot respectively. Similarly, PPD predics thermal comfort of a people and is largely related to PMV; the most people feel comfortable at neutral ambient temperature. The

thermally neutral and comfortable ambient temperature window is only ±1 °C[14,15], and individual body parts have their own local comfort temperatures[14,15]. For instance, the thermal comfort temperature for head (~21 °C) is much lower than that for foot (~29°C). Therefore, it is challenging to maintain human body thermally comfortable without external thermoregulation system.

1.5 Indoor Climate Control and Personal Thermoregulation

Thermal sensation is one of the most important aspects of our daily lives; however, the range of ambient temperature that human feel comfortable is very narrow as previously discussed. Therefore, thermoregulation of a human body largely relies on climate control of buildings or vehicles, and the indoor temperature is set to satisfy occupants. However, various needs of the indoor temperature depending on outdoor weather conditions or individual preferences suggest the difficulty of indoor climate control. For instance, the indoor thermal comfort temperature varies from 21 °C to 28 °C depending on outdoor temperature[16], and occupants have various thermal sensation even at the optimized indoor temperature[17]. Since current indoor climate control systems heat and cool entire space, it is difficult to meet all the thermal needs.

In addition to the aspect of thermal comfort, the traditional climate control systems waste huge energy by heating and cooling almost empty spaces in buildings or vehicles whereas peoples occupy only small space. It is thus not surprising that the traditional systems consume more than 10% of primary energy usage in developed countries. In addition, the energy demand is expected to grow rapidly in the coming decades in developing economies,

such as India and China, where the air conditioning system are being increasingly deployed. The rising demand on climate control not only poses a grand challenge on energy supply but also raises severe environmental concerns, as illustrated by the recent Kigali Amendment to Montreal protocol aiming to curb the emission of hydrofluorocarbons from air conditioners, which have global warming potentials over 1,000.

Personalized climate control presents an attractive, paradigm-shifting cooling technology, as it could reduce the cooling volume and the associated energy demand by orders of magnitude compared to the centralized space cooling technologies. As such, personalized thermo-regulation has become an intensively pursued research subject in recent years, as evidenced by recent publications in this area, such as IR transparent textiles[18,19], radiative cooling polymers[20], and electrocaloric device[21]. However, none of these strategies can achieve large and active cooling in a controllable manner under ubiquitous environments. For instance, the textiles can only work for passive cooling or heating; radiative cooling requires a large view factor to the sky; and the electrocaloric effect only achieved small cooling (temperature difference < 2 °C) and required several kilovolts of voltage, making it unsuitable for wearable applications. Therefore, personalized air conditioning technology have plenty of room for improvement and great opportunity for substantial energy saving and personal thermal comfort.

1.6 Thesis Structure

In this thesis, I will first discuss about a wearable thermoelectric device (TED) for personal thermoregulation (Chapter 2). In the chapter, I will demonstrate a wearable TED

that can deliver over 10 °C cooling effect with a high coefficient of performance (COP>1.5). The TED achieved long-term active cooling with high flexibility, thanks to a novel design of double elastomer layers embedding an air gap insulation and high-ZT rigid TE pillars. The TED can be integrated into a wearable garment and exhibited excellent personal thermoregulation performance on human skin in the large ambient temperature range of 22 °C to 36 °C. The low power consumption of the TED, which is a few orders of magnitude lower than the conventional climate control system (~1.5 kW per capita), will be also discussed in detail.

Using this wearable TED and the thermoelectric cooling/heating effect, I will further discuss about personal thermal camouflage technique (Chapter 3). Although majority of IR camouflage techinic relies on IR emissivity manipulation, which performance can be easily degraded by contamination of the surface or reflection of hot/cold spots in nature, direct temperature control to manipulate IR emission has a unique advantage: wide camouflage temperature window and high-emissivity property that enables reflection. The direct temperature control by TED only demonstrated previously for vehicles; however, thermal management on human skin is much more challenging because of the strict temperature requirement of a human body. In the chapter, I will demonstrate a wearable and active thermal camouflage TED responding to background temperature change on human skin.

Lastly, in Chapter 4, I will present the first demonstration of single-cell metabolic heat measurement by our novel chip-calorimeter possessing 0.6 nW of high sensitivity. The innovative one-dimensional design reduced thermal conductance as low as 2.5 $\mu W\ K^{-1}$ and enabled to measure a few nanowatts of small heat production by single *Tetrahymena thermophila*. Single-cell measurements using our calorimeter revealed that the relationship

between metabolic rate and cell size of individual *Tetrahymena* follows the three-quarter power allometric law. Finally, a mitochondrial uncoupling agent dosed to single *Tetrahymena* through the microfluidic channel, and measurement of spare respiratory capacity (SRC) will be demonstrated.

Chapter 2

Wearable Thermoelectrics for Personalized Thermoregulation

2.1 Introduction

Thermoregulation plays a vital role in human comfort and heath but also contributes significantly to energy consumption. The heating and cooling of buildings alone currently accounts for more than 10% of the total energy consumed globally[7], and this high level of energy consumption and the accompanying environmental impact, i.e., the emission of potent global warming gases, are expected to increase dramatically with the rapid growth of economies[22]. Climate control systems are also used to achieve thermal comfort in electric vehicles; however, these systems can drain up to 40% of battery power in adverse weather conditions, presenting a major roadblock to achieving long driving ranges[23].

The ongoing effort to reduce the energy consumption of climate control systems has mainly focused on the development of more efficient thermoregulation technologies[24]. However, a substantial amount of energy is being wasted by traditional climate control systems, as they heat/cool entire buildings or vehicles even though the occupants only occupy a small space. The large amount of wasted energy is evident when considering the great disparity between the human metabolic rate (100–150 W)[25] and the per capita heating,

ventilation, and air conditioning (HVAC) energy consumption rate in the United States (~1.5 kW)[7]. Moreover, it is difficult to set the temperature of an entire building or vehicle to ensure the thermal comfort of all the occupants or passengers as thermal comfort conditions can vary significantly from person to person[17]. In addition to the implications for the energy efficiency of buildings and vehicular thermal envelops, there is also tremendous interest in achieving optimal thermal comfort for various outdoor application scenarios, such as those encountered in sports, military, special occupations, and health care[26].

Recently, there has been growing interest in personal thermoregulation devices[19,27], which can deliver a precise thermal dose to target spots on individuals and consequently reduce the heating or cooling volume by orders of magnitude compared with building/vehicular-level thermal envelops. These devices are also useful for outdoor heating or cooling, where centralized heater or AC are not available. Heating garments that exploit Joule heating, such as metallic nanowire meshes[27], are an example of such devices. However, the development of active cooling garments is far more challenging and largely unexplored as most current cooling devices are bulky and difficult to integrate into a garment. For instance, commercially available cooling vests contain bulky fluidic channels for coolant circulation or water/ice packs, and their cooling power is not adjustable[26]. Given these inherent drawbacks of fluidic-based personal cooling garments, current studies are primarily focused on solid-state technologies such as electrocaloric[28], magnetocaloric[29], and thermoelectric cooling systems[30]. Nevertheless, despite extensive material-level studies, wearable devices with high cooling performance have yet to be demonstrated. Active cooling was recently demonstrated in miniaturized electrocaloric devices[31] with a high voltage (~10 kV); however, the temperature drop remained small (1.4 °C).

Thermoelectric devices (TEDs) are especially attractive for personalized cooling application as they are solid state with small form factors and the cooling power is readily adjustable. Although there has been substantial work on flexible TEDs for wearable applications[32-52], the majority of these devices have only achieved power generation by harnessing body heat[34-52] or have shown limited cooling effect with the assistance of bulky heat sinks (such as water gels or fans)[46,47]. To the best of our knowledge, *none of these wearable TEDs have shown long-term (e.g., > 1 h) active cooling* without the use of bulky heat sinks. Even though various wearable TE power generators can in principle be used for cooling, the requirement of achieving active cooling, that is, pumping the heat from the cold to hot side, is substantially more stringent. A wearable TED capable of power generation is not necessarily suitable for active cooling: the Peltier cooling power on the cold side must overcome the parasitic heating effects of both the heat conduction from the hot side and Joule heating; in addition, the heat pumped to the hot side must be efficiently dissipated into the environment (hence the need for bulky heat sinks). Fundamentally, the devices must possess high performance (measured by the TE figure of merit, ZT) with a suitable thermal design. Some previously reported TEDs have only shown power generation capability[34-45,48-52]; however, none have exhibited sustainable active cooling performance without the aid of a water heat sink[46,47], primarily because of the low performance of flexible TE materials (e.g., polymers or organic/inorganic hybrids[53] with $ZT < 0.42$) or unoptimized thermal design for cooling even with high-performance Bi–Te-based TE materials[34-43].

Herein, we designed and demonstrated the *first* flexible and wearable TED with long-term (> 8 h) and large (> 10 °C) active cooling effect by addressing the aforementioned challenges. Our TED design utilizes an innovative fabrication scheme of sandwiching rigid

inorganic high-ZT TE pillars between stretchable elastomer sheets and, by virtue of the novel thermal design, demonstrates a large cooling effect of more than 10 °C to the skin without the use of any heat sinks. Although active cooling data is not available for previously reported wearable TEDs, our flexible TED exhibits higher power output when used as a power generator from body heat than previous TEDs (up to 4.5–25.1 μW cm^{-2} in our TED vs. 10^{-3} to 2.28 μW cm^{-2} in previous TEDs[35-43]). We also integrated the TED into a wearable garment with long-term, energy-efficient cooling and heating effects on human skin: the garment kept the skin at the thermal comfort temperature of 32 °C while the ambient temperature varied within the large range of 22 °C to 36 °C. Finally, an all-flexible personalized thermoregulation package was demonstrated by integrating a flexible battery pack into the TED garment. Our flexible and high-performance TED design may pave the way for personalized cooling with the benefits of substantial energy savings and improved thermal comfort.

2.2 Design, Fabrication, and Characterization of Flexible TED

We utilized a novel concept of double elastomer layer design embedding an air gap insulation layer between two stretchable sheets and high-ZT inorganic TE pillars with optimized aspect ratio and spatial density. This design minimized the thermal leakage through the TED, eventually resulting in the high cooling performance, and maximized the device flexibility. A schematic illustration and photograph of our TED are presented in Fig. 2.1, A to C. To achieve mechanical flexibility and high cooling performance, we utilized the double elastomer layers design, sandwiching rigid TE pillars (1×1 mm^2 in cross section and 5 mm

in height, with a 3-mm gap between pillars) between two 1-mm-thick stretchable Ecoflex sheets separated by a 4-mm air gap (Fig. 2.1C). The top and bottom 0.5-mm-long segments of the TE pillars were embedded in the Ecoflex sheets. This double-layer design provides sufficient flexibility despite the rigidity and high aspect ratio of the TE pillars and greatly enhances the cooling effect. As shown in Fig. 2.1D, when the TED with the double-layer design is bent, the top stretchable sheet expands while the bottom sheet contracts, and our finite element simulation showed that the bending stiffness of the double-layer design is only 30% of the conventional single elastomer layer design (Fig. 2.1E), which can be found in majority of previous flexible TEDs[34-43,45]. The fabrication process of our TED is presented in Fig. 2.1F and described in detail in Materials and Methods. Photographs of the devices during the intermediate fabrication steps are shown in Fig. 2.2, A to D. Including all the components, the TED remains thin (6 mm) and light (0.56 g cm^{-2}) (see Fig. 2.2, E and F) compared to conventional cooling garments[26] or TEDs with bulky heat sinks[46,47].

The salient features of the thermal design in our TED include the high aspect ratio (height: width = 5:1) of the pillars with low spatial density (6.25%) and the large air gap between the stretchable sheets (4 mm), which result in small thermal conductance between the cold and hot sides of the TED. The finite element simulation also showed that the overall conductance of our TED design (G_{TED}) is ~ 30 W m^{-2} K^{-1}, which is 50% lower than that of the conventional single-layer design (Fig. 2.1E). This low G_{TED} is comparable to the heat transfer coefficient between the TED and air (h_{air} ~ 10–20 W m^{-2} K^{-1}) resulting from natural convection and radiation[54]. This thermal resistance matching ensures that the heat pumped from the cold (skin) side as well as the Joule heating will dissipate into the air rather than flowing back to the skin (Fig. 2.1C). If G_{TED} were substantially higher, an efficient heat sink

would be needed to match h_{air} with G_{TED}, such as that used in prior wearable TEDs[44-47]. However, there is also a limit to the continuous reduction of G_{TED} by applying taller and smaller pillars, as excessively taller and smaller pillars would result in larger electrical resistance and Joule heating and compromise the device flexibility and mechanical strength (Fig. 2.3 and Fig. 2.1E). In addition, the large distance between adjacent TE pillars requires efficient lateral heat spreading to ensure that a uniform temperature is maintained within each of the Ecoflex layers; this heat spreading was achieved by embedding AlN microparticles into the Ecoflex to increase its lateral thermal conductivity.

Our main strategy is to match thermal impedance between the TED and the environment. This is illustrated by the thermal balance of the TED for active cooling, which requires $T_{bare} > T_c$, where T_{bare} is the bare skin temperature without a TED or garment and T_c is the skin (cold side) temperature with TED cooling (Fig. 2.1C).

On the bare skin without the TED or garment:

$$Q_{skin} = h_{air}(T_{bare} - T_{air}) \tag{2.1}$$

where Q_{skin} is the metabolic heat from the skin, h_{air} is the heat transfer coefficient to the, air and T_{air} is the temperature of the air.

On the cold (skin) and hot sides of the TED:

$$Q_{skin} = Q_{P,c} - Q_{cond} - Q_J \tag{2.2}$$

$$Q_{air} = Q_{P,h} - Q_{cond} + Q_J \tag{2.3}$$

where $Q_{P,c}$ is the Peltier cooling effect ($Q_{P,c} = S \cdot I \cdot T_c$, where S is the Seebeck coefficient, I is the current, and T_c is the temperature of the cold side, i.e. the skin, Q_{cond} is the conductive heat from the hot to the cold sides of the TED ($Q_{cond} = G_{TED}(T_h - T_c)$, where G_{TED} is the

thermal conductance of the TED and T_h is the temperature of the hot side), Q_J is the joule heating of the TED ($Q_J = 0.5I^2R,$ where R is the resistance), Q_{air} is the heat dissipation to the air ($Q_{air} = h_{air}(T_h - T_{air})$), and $Q_{P,h}$ is the Peltier heating effect on the hot side ($Q_{P,h} = S \cdot I \cdot T_h$).

By combining Eqs. (2.1) and (2.2),

$$h_{air}(T_{bare} - T_{air}) = Q_{P,c} - G_{TED}(T_h - T_c) - Q_J \quad (2.4)$$

We know $T_h > T_{air}$ since $Q_{air} > 0$, and $T_{bare} > T_c$ for the any active cooling, which results in $T_{bare} - T_{air} > T_c - T_h$. Then,

$$G_{TED}(T_h - T_c) < h_{air}(T_h - T_c) + Q_{P,c} - Q_J \quad (2.5)$$

Eq. 2.5 can be summarized to

$$G_{TED} < h_{air} + \alpha \quad (2.6)$$

where α is a function of $Q_{P,c}$, Q_J, T_h, and T_c. Eq. 2.6 shows that a small G_{TED} is required relative to h_{air} for the active cooling. However, the thermal impedance mismatch between G_{TED} and h_{air} of commercial TEDs is large: commercial TEDs has G_{TED} greater than 1000 W m^{-2} K^{-1}, and h_{air} on the TED without heat sink under a typical indoor condition is 10 – 20 W m^{-2} K^{-1}. Therefore, these devices only work when there is an efficient heat sink (e.g., fin or fan), but the bulky heat sinks render the TEDs non-wearable.

The basic thermoelectric and mechanical characteristics of the fabricated flexible TED are shown in Fig. 2.4. As discussed, reducing G_{TED} is imperative to achieve active cooling without resorting to the use of bulky heat sinks. The measured G_{TED} was 32 W m^{-2} K^{-1} (Fig. 2.4A), which falls within the optimal range for the cooling of human skin at a typical metabolic rate (50–100 W m^{-2})[25]. The corresponding average thermal conductivity of

the TE pillars was determined to be 1.52 W $m^{-1} K^{-1}$. The average Seebeck coefficient (S) of the TED at the device-level was measured to be 196 μV K^{-1} $pillar^{-1}$ (Fig. 2.4B). Finally, the overall electrical resistance of the TED was measured to be 7.9 Ω, yielding an average electrical conductivity (σ) of 932 S cm^{-1}. The corresponding device-level ZT was determined to be 0.71 at room temperature. This ZT value is consistent with that of the constituent n- and p-type materials with the same compositions previously studied by us [48], indicating the minimal influence of our device fabrication process on the material properties as well as the high-quality interfaces for thermal and electrical transport.

The lateral thermal conductivity of the stretchable sheet (k_p) with embedded AlN particles (26 vol.%) was measured to be 0.77 W $m^{-1} K^{-1}$, which represents an approximately four-fold enhancement over that of pristine Ecoflex (0.20 W $m^{-1} K^{-1}$), as shown in Fig. 2.4C. Incorporating all of these material properties, our finite element simulation indicated that the flexible TED is expected to provide ~7 °C of maximum cooling with only natural convection and radiation (Fig. 2.4D and Fig. 2.5 for details). Our simulation also showed that the higher k_p achieved with the addition of the AlN microparticles reduces the peak-to-peak temperature variation on the stretchable sheets by up to 70% (from 2.7 °C to 0.7 °C) and, eventually, saves the power consumption by up to 40 % at 6.6 °C of TED cooling effect (Fig. 2.5B and E). In addition, the simulation results indicate that the thermal conductivity of our Ecoflex/AlN mixture layer (0.77 W $m^{-1} K^{-1}$) is sufficient to achieve minimal power consumption (or maximal cooling effect) because the temperature variation within the Ecoflex/AlN mixture layer is already sufficiently uniform (0.7 °C) compared to the temperature difference between the hot side and ambient (~10 °C) (Fig. 2.5F).

The flexibility and mechanical robustness of the TED were also demonstrated by monitoring the electrical resistance in real time under bending conditions using various bending radii (r). The resistance of the TED was stable when r was reduced to 20 mm (Fig. 2.4E), which represents the largest curvature of a human body. The resistance of the device was also stable during 1,000 bending cycles for r = 30 mm (Fig. 2.4F). These results demonstrate the excellent flexibility of the TED enabled by our double elastomer layer design embedding rigid TE pillars between two thin stretchable Ecoflex sheets.

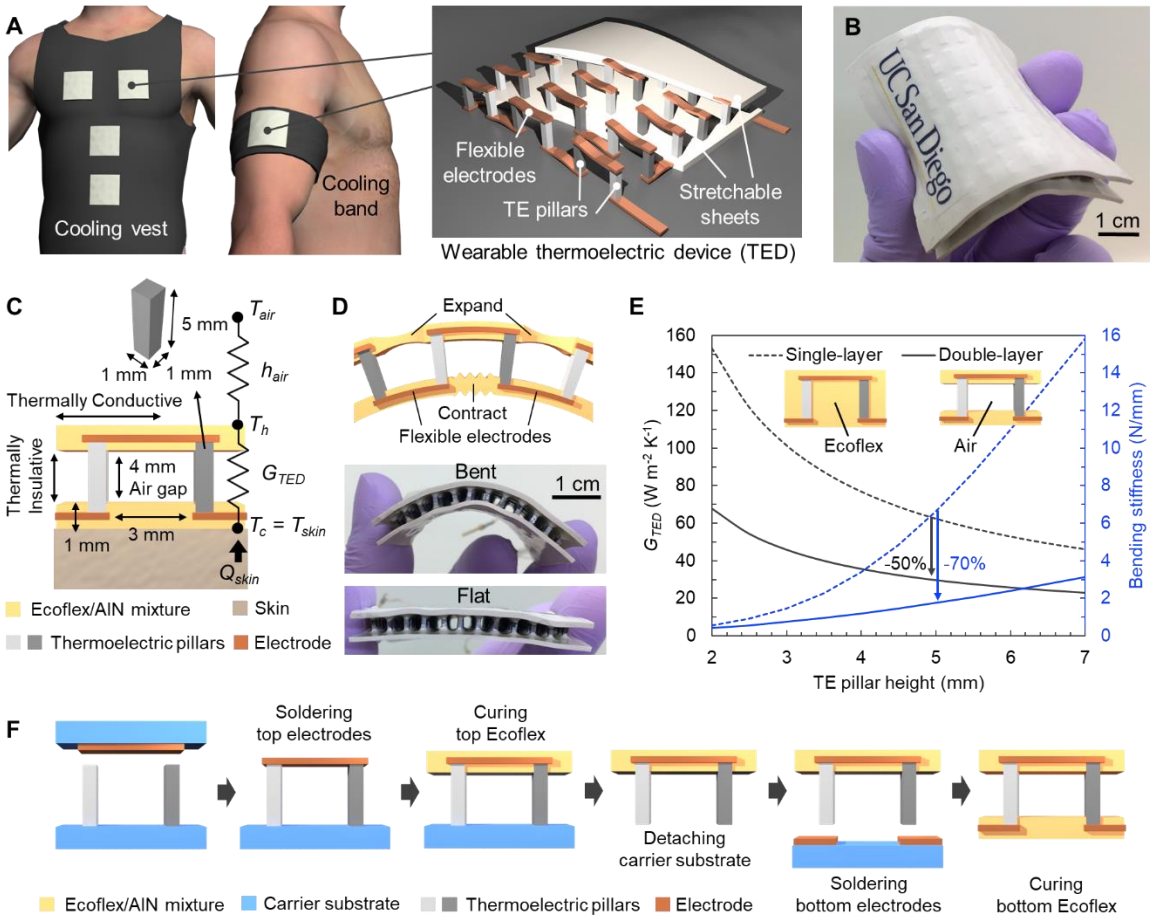


Figure 2.1 TED design and fabrication process. (**A**) Schematic illustration of cooling garments with wearable TEDs (left). The internal structure of the wearable TED with TE pillars connected by flexible copper electrodes and sandwiched between two stretchable sheets (right). (**B**) Photograph of the fabricated 5×5 cm^2 flexible TED. (**C**) Schematic illustration of TED design. The low thermal conduction inside the TED and high thermal conduction within the stretchable sheets are the key features of the design used to achieve the cooling effect. (**D**) Schematic diagram and photographs showing the flexibility of the TED. The double-layer design of stretchable sheets enhances the flexibility. During bending, the top stretchable sheet expands while the bottom stretchable sheet contracts. (**E**) Finite element simulation comparison of G_{TED} and the bending stiffness of double- and single-layer designs of flexible TEDs as a function of TE pillar height. The double-layer design reduces G_{TED} by 50% and the bending stiffness by 70% compared to those of the single-layer design. (**F**) Fabrication process of the TED (see Materials and Methods for details).

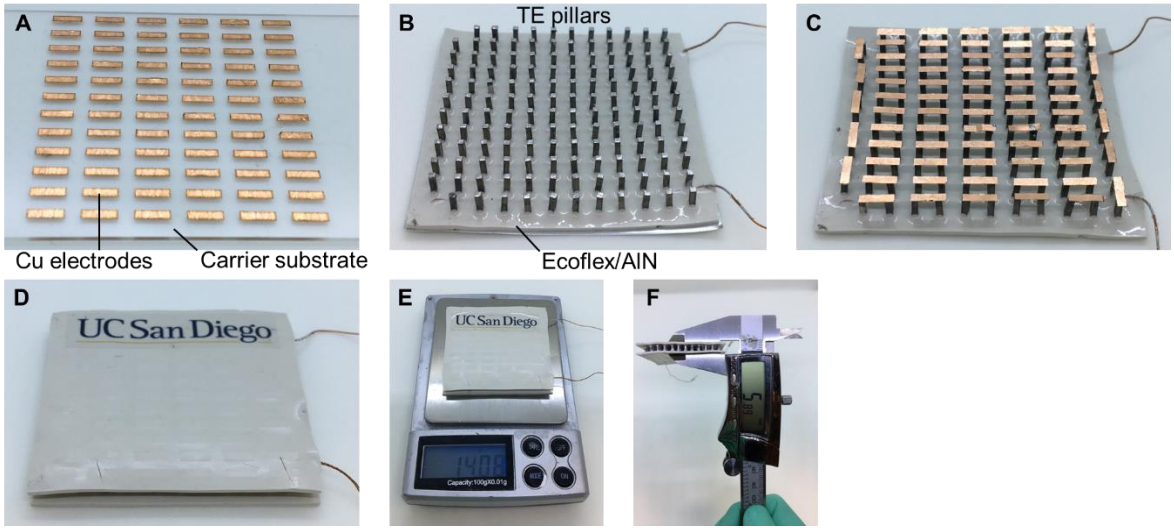


Figure 2.2 Fabrication and characterization of TED. (**A**) A carrier substrate with an array of copper electrodes. (**B**) An array of 142 TE pillars with the fabricated bottom layer including copper electrodes and AlN particles embedded in an Ecoflex stretchable sheet. (**C**) Soldered copper electrodes on the TE pillars. (**D**) Fabricated flexible TED by curing and cutting the Ecoflex/AlN mixture sheet. (**E**) Weight of the TED (14.1 g per device). (**F**) Thickness of the TED (~6 mm).

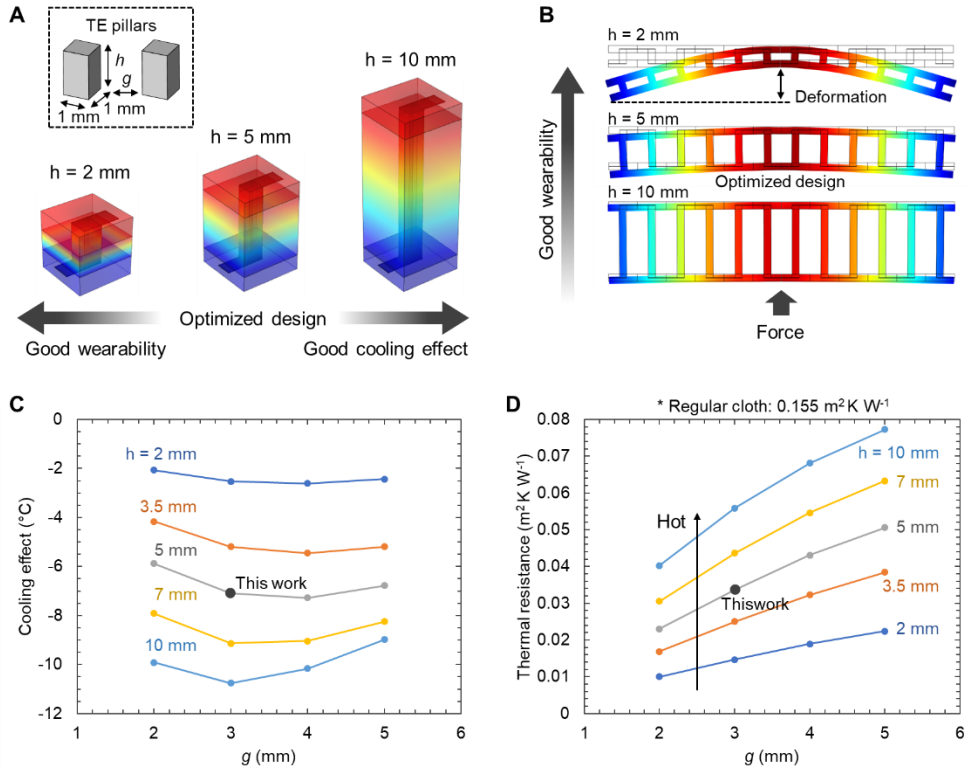


Figure 2.3 Optimization of the TED. (**A**) Heat transfer model in COMSOL to optimize the TED design. The model used various geometric parameters for the optimization including the height of TE pillars (h = 2, 3.5, 5, 7, and 10 mm) and the gap between TE pillars (g = 2, 3, 4, and 5 mm). (**B**) Mechanical model in COMSOL used in Fig. 2.1E. Bending stiffness was simulated by applying a force and monitoring the corresponding deformation. (**C**) Maximum cooling effects with various TE pillar height and TE gap (g) values. The cooling effect was enhanced with increasing h up to 10 mm while there was an optimum g to maximize the cooling effect. However, the h also has to be optimized since a large h resulted in poor wearability as shown in (B) and Fig. 2.1E. (**D**) The thermal resistance of TED with various h and g values. Larger h and g values led to higher thermal resistance of the TED impeding heat dissipation and skin thermal comfort at hot environment when the TED is not operating. Our TED design with h = 5 mm and g = 3 mm showed a thermal resistance of 0.035 m^2 K W^{-1}, which is only ~20% of the resistance of regular clothes (0.155 m^2 K W^{-1}).

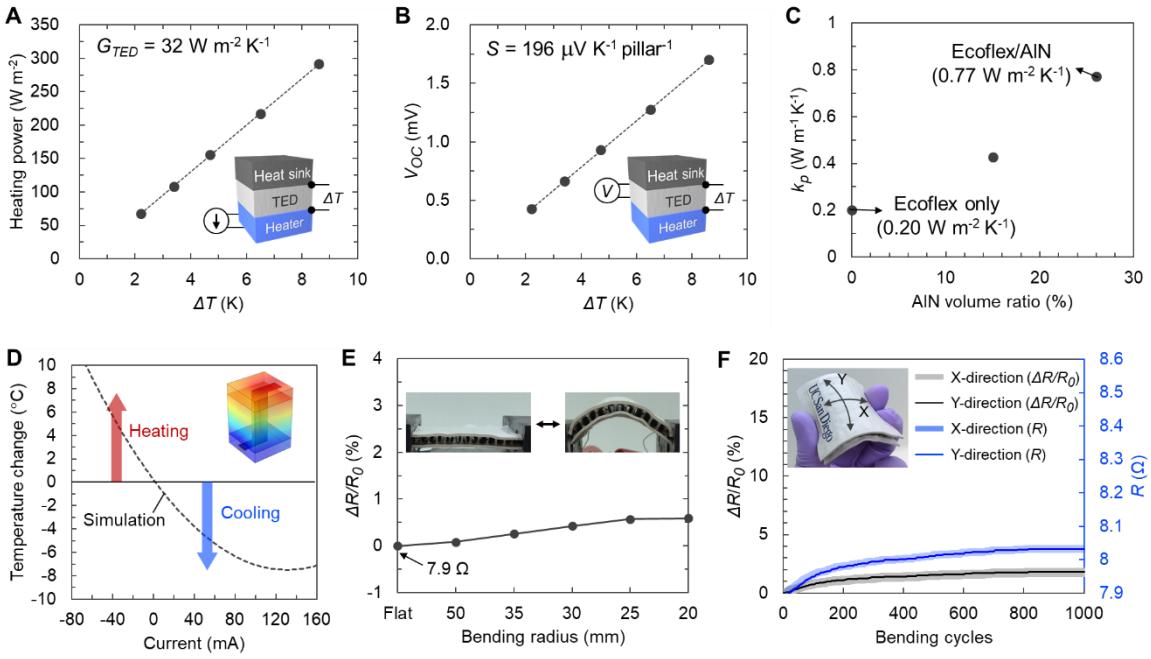
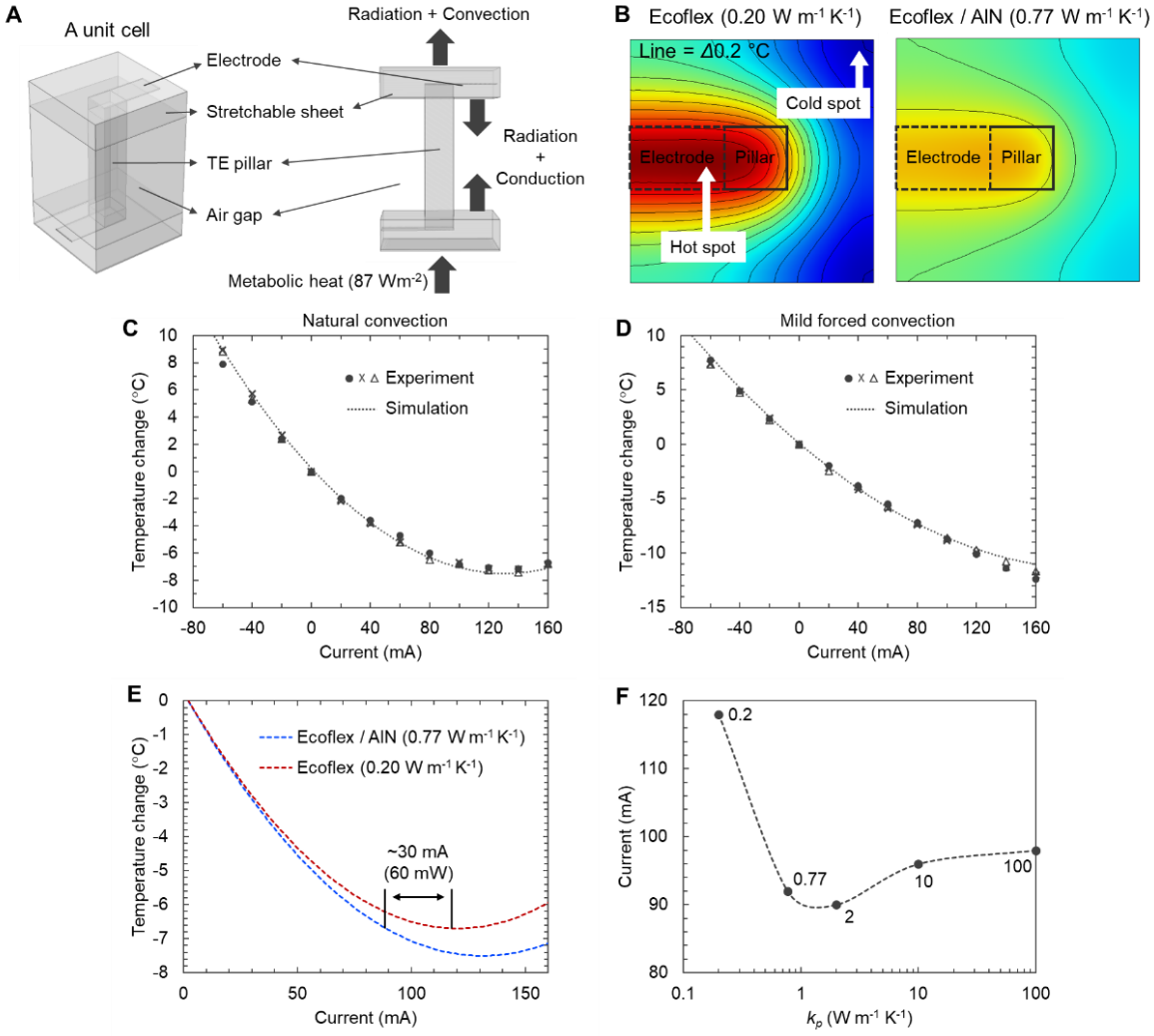


Figure 2.4 Characterization of the TED. (**A**) Measurement of the thermal conductance of the TED (G_{TED}). A G_{TED} value of 32 W m^{-2} K^{-1} was determined from the slope of the temperature differences between the cold and hot sides (ΔT) vs. the applied powers. (**B**) Measurement of device-level Seebeck coefficient (S = 196 μV K^{-1}) by comparing ΔT and corresponding open-circuit voltages (V_{OC}). (**C**) Thermal conductivity of the polymeric Ecoflex stretchable sheets (k_p) for various volume ratios of the Ecoflex and AlN microparticles. The mixture layer containing 26 vol.% of AlN microparticles exhibited k_p = 0.77 W m^{-1} K^{-1}, which is four times higher than that of pristine Ecoflex (k_p = 0.20 W m^{-1} K^{-1}). (**D**) Finite element simulation of cooling/heating effect with the measured TED parameters. More than 7 °C maximum cooling was estimated with only natural convection and radiation. (**E**) Electrical resistance (R) stability for various bending radii (r) from flat to 20 mm, where R_0 is R when the TED is flat, and ΔR is the difference between R and R_0. (**F**) Electrical resistance stability over 1,000 bending cycles with r = 30 mm.

Figure 2.5 COMSOL modeling of the TED cooling effect. (**A**) A unit cell of the TED with 1-mm thick top and bottom stretchable sheets, a TE pillar (1×1×5 mm), Cu electrodes (35 μm in thickness), and a 4-mm thick air gap. An empirical equation ($h_{conv} = 1.32(\Delta T/L)^{0.25}$) was applied to model the natural convection heat transfer to the air, where $\Delta T = T_h - T_{air}$, T_{air} is the ambient temperature, and L is the characteristic length. A heat flux of 87 W m^{-2} from the bottom of TED was used as the metabolic heat from a human body. Radiation between the cold and hot sides was also considered in addition to the conduction through the air gap since the radiation accounts for ~40% of the total heat transfer in the air gap. (**B**) Simulation results of temperature distribution in the heat spreading layers, made of either pristine Ecoflex (left) or an Ecoflex/AlN mixture (right). The pristine Ecoflex showed up to 2.7 °C temperature variations within the sheet, whereas the Ecoflex/AlN mixture had ~0.7 °C maximum temperature difference. (**C**) Comparison of experimental results and the simulation result under a natural convection condition. (**D**) Comparison of experimental results and the simulation result under a mild forced convection condition with ~5 km h^{-1} wind. Three experimental data points at each applied electric current were plot together in (C) and (D) and showed excellent match with the simulation result. The root mean square error of the experimental data points was less than 0.3 °C. (**E**) Simulation results of cooling effect with Ecoflex and Ecoflex/AlN mixture heat spreading layers. The high thermal conductivity of Ecoflex/AlN mixture layer reduces the power consumption of the TED by up to 40% (from 140 mW to 80 mW) at 6.6 °C of TED cooling effect. (**F**) Simulation results of power consumption at 6.6 °C of TED cooling effect with various thermal conductivity of the stretchable sheet (k_p). The results indicate that the power consumption of the TED with Ecoflex/AlN mixture layer (k_p = 0.77 W m^{-1} K^{-1}) almost reaches the minimum value. It is worth noting that the power consumption increase with the k_p higher than ~1.5 W m^{-1} K^{-1}, which is similar to the thermal conductivity of TE pillars, is because the heat flow through TE pillars easily dissipates at the interface of TE pillars and the stretchable sheets, and 0.5-mm-long segment of TE pillars embedded in the stretchable sheets cannot contribute the thermal insulation between cold and hot sides anymore.


A
A unit cell
Electrode
Stretchable sheet
TE pillar
Air gap
Radiation + Convection
Radiation
+
Conduction
Metabolic heat (87 Wm-2)
B
Ecoflex (0.20 W m-1 K-1)
Ecoflex / AlN (0.77 W m-1 K-1)
Line = Δ0.2 °C
Cold spot
Hot spot
Electrode
Pillar
C
Natural convection
Experiment
Simulation
Temperature change (°C)
Current (mA)
D
Mild forced convection
E
Ecoflex / AlN (0.77 W m-1 K-1)
Ecoflex (0.20 W m-1 K-1)
~30 mA
(60 mW)
F
Current (mA)
kp (W m-1 K-1)
0.2
0.77
2
10
100

2.3 Power Generation Performance of Flexible TED

With the use of the air gap insulation layer and the optimal thermal design of high-ZT TE pillars, our TED surpasses the performance of all previously reported flexible or wearable TEDs, which is the key reason why our device is capable of delivering the long-term active cooling effect. As none of the previous devices achieved active cooling effect without the use of heat sinks, here we demonstrate power generation from human body heat using our TED and directly compare it to that of previously reported flexible TEDs. During the measurement, our flexible TED was attached to the wearer's arm; the voltage, current, and temperature difference between the cold and hot sides (ΔT) were measured under various load resistances and thermal conditions. A schematic illustration of the measurement setup and the results are presented in Fig. 2.6, A to C. When the wearer was sitting stationary in an indoor environment at 22 °C, the maximum open-circuit voltage (V_{OC}) was 74.5 mV and the maximum power density of our flexible TED on 32 °C human skin was 4.5 μW cm^{-2}. This is the highest generated power density ever reported for wearable TE generators on human skin without heat sinks. Previous wearable TE generators based on a wide variety of materials and designs without heat sinks[35-43,50-52] have exhibited maximum power densities of up to 2.28 μW cm^{-2} on human skin[38], as summarized in Fig. 2.6D. Furthermore, the power density increased to 10.7 μW cm^{-2} when the wearer was walking at a speed of 5 km h^{-1} because of the increase in h_{air} (19.6 W m^{-2} K^{-1})[54] and to 25.1 μW cm^{-2} in a cold indoor environment (10 °C). The maximum power generation vs. ΔT on the skin followed the same trend as that on the heater setup (Fig. 2.6C).

The high performance in power generation of our flexible TED originated from the use of high-ZT inorganic TE materials in a flexible form and our optimal thermal design, namely, a low G_{TED} that matches human metabolic heat and natural convection conditions, which are also the two prerequisites to achieve active cooling on human skin without a heat sink, as discussed earlier. To further illustrate this point, we investigated the relationship between the power generation (Seebeck effect) and the cooling effect (Peltier effect) as a function of G_{TED} and ZT through simulation. We set the human metabolic heat (Q_{skin}) to 87 W m^{-2} and h_{air} to 10 W m^{-2} K^{-1} with natural convection and radiation. As shown in Fig. 2.6E, the power generation and cooling effect clearly followed the same increasing trend with decreasing G_{TED}. When the ZT of the TED was 0.7, the device only provided an appreciable (> 3 °C) cooling effect when G_{TED} was less than 120 W m^{-2} K^{-1}, which corresponds to a power generation density higher than 4 μW cm^{-2}. The required G_{TED} would be even lower if the device had a lower ZT. Because of the low power generation of most previous flexible TE generators without heat sinks (< 2.28 μW cm^{-2}), it was challenging to achieve an appreciable cooling effect on human skin.

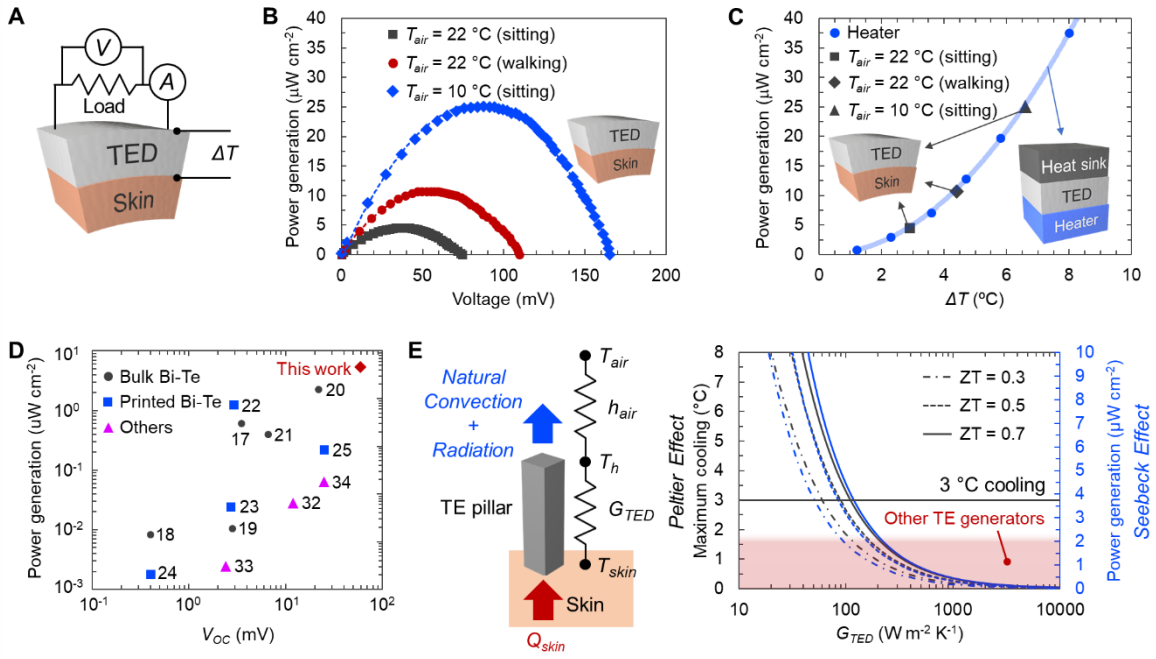


Figure 2.6 Power generation of the TED and its impact on active cooling. (**A**) Schematic diagram of the measurement setup used to monitor power generation on human skin. The voltage and current were measured with various load resistors while the TED was attached to the wearer's arm. (**B**) Power generation as a function of output voltage under various thermal conditions. (**C**) Summary of the maximum power generation from our TED on a heater or human skin. The maximum power generation on human skin was 4.5 μW cm^{-2} and the open-circuit voltage (V_{OC}) was 74.5 mV at room temperature (T_{air} = 22 °C) with natural convection (sitting). The power generation increased up to 10.7 μW cm^{-2} with mild forced convection (walking) and up to 25.1 μW cm^{-2} under cold condition (sitting, T_{air} = 10 °C). (**D**) Summary of power generation and V_{OC} of wearable TEDs from the literature. All the measurements were performed on human skin without heat sinks at room temperature. (**E**) Simulation results comparing cooling (Peltier effect, black) and power generation (Seebeck effect, blue) performance as functions of G_{TED} and ZT (right) and schematic illustration of the geometry and thermal conditions used in the simulation (left).

2.4 Cooling and Heating Performance of Flexible TED on Simulated Heater

We characterized the cooling and heating effect of the TED using a laboratory setup (Fig. 2.7A). The thin-film heater in the setup generated a heat flux of 87 W m^{-2} to simulate the typical metabolic rate from a human in an indoor environment [25]. The cooling and heating performance were evaluated by monitoring the temperature at the bottom of the TED (T_c) while a current (I) ranging from −60 to 140 mA was applied to the TED. The negative and positive current resulted in heating and cooling effects, respectively, as expected from the TED configuration. At each applied current, T_c began changing instantaneously and reached a plateau within a few minutes (Fig. 2.7B). When I = 140 mA, a large steady-state temperature reduction of 7.3 °C was achieved with only natural convection and radiation. This cooling effect could be maintained for an extended period (~8 h) (Fig. 2.7C).

The stabilized temperature change as a function of the applied current is displayed in Fig. 2.7D. As expected from our finite element model (Fig. 2.7D), T_c could be deterministically decreased or increased by applying positive or negative current, respectively, because of the Peltier and Joule heating effects. The cooling effect (T_c reduction) was eventually saturated and then diminished with increasing positive current because of the excessive Joule heating. Because of the flexibility of the TED, the cooling and heating effects did not change on a curved substrate with bending radii of 40 and 30 mm (Fig. 2.7E). We also determined the coefficient of performance (COP) of the devices (right axis in Fig. 2.7D), which is the ratio between the heat removed from the skin (87 W m^{-2}) and the applied electric power (see Materials and Methods for details). The COP values were measured to be 1.7 and

7.6 for 7 °C cooling and heating, respectively. The high COP values indicate a low power consumption of ~90 W for cooling and ~20 W for heating per person assuming total metabolic heat of ~150 W for a human body area of 1.8 m^2.

The operation of the TED was also tested under a mild convection condition with a wind speed of 5 km h^{-1}. This wind speed can be expected in certain indoor [55] and outdoor environments (e.g., walking) [54] and will lead to a moderate increase of h_{air}. As shown in Fig. 2.7F, the maximum cooling was greater than 13 °C, approximately twice that under the natural convection condition because of the more efficient heat dissipation to the air. Using COMSOL modeling, we determined that this temperature reduction corresponds to h_{air} of ~20 W m^{-2} K^{-1} (Fig. 2.5D), which is expected for the 5 km h^{-1} wind speed.

As previously discussed, the high performance of the TED can be attributed to the unique thermal design: thermal insulation between the cold and hot sides and lateral heat spreading within the Ecoflex/AlN layers. The TE pillars with a small height-to-width ratio in traditional TEDs result in large thermal leakage (large G_{TED}), which diminishes the cooling performance. To verify the thermal design concept, the cooling/heating performance of a commercial TED (430857-500, Laird Technologies) and three flexible TEDs with various pillar designs were characterized for comparison (Fig. 2.8A). A clear trend of enhanced cooling/heating effect was observed with increasing height-to-width ratios of the TE pillars, as shown in Fig. 2.8B. Similar trends were also observed with increasing gap between pillars and increasing lateral thermal conductivity of the elastomer sheets.

We further demonstrated thermoregulation performance of the TED, namely maintaining human skin temperature constant in the wide range of ambient temperature, with a realistic human skin setup (Fig. 2.7G). The setup simulated 37 °C of constant body core

temperature (T_{core}) using a feedback-controlled heater and heat transfer within human skin using a 1.2-cm thick PDMS layer, which has similar thermal conductance as that of the skin (G_{skin} = 11 – 17 W m^{-2} K^{-1} at comfortable conditions) [15]. A temperature-controlled chamber enveloped the setup and changed the ambient temperature during the demonstration. The TED and a PID controller were programed to maintain surface temperature of the PDMS layer (T_{skin}) constant while the ambient temperature was increased from 19 °C to 33 °C under the natural convection condition and from 15 °C to 36 °C under the mild forced convection condition (5 km h^{-1} wind).

As shown in Fig. 2.7H, within the entire ambient temperature range, the TED could maintain T_{skin} at its setpoint, the neutral skin temperature at the neutral ambient temperature (26 °C), by cooling and heating. The negative currents for TED heating or the positive currents for TED cooling were applied by the PID controller to compensate the lower or higher ambient temperature than the neutral ambient temperature, respectively. The results indicate that the TED thermoregulation can provide thermally comfortable condition to a human body in the 14 °C (19°C – 33 °C) of large ambient temperature window and the window can even broaden up to 21 °C (15°C – 36 °C) with the mild forced convection. The hottest ambient temperature (33 °C) under the natural convection condition was 7 °C higher than the neutral ambient temperature, and the TED cooling successfully maintained T_{skin} with 140 mA of applied current. This suggests 7 °C cooling effect of the TED, which matches with the maximum temperature drop shown in Fig. 2.7D. Under the mild forced convection condition, the cooling effect was even larger; the TED could maintain T_{skin} with 160 mA of applied current at the ambient temperature as high as 36 °C, which is 10 °C higher than the neutral ambient temperature. Considering the TED showed extra cooling effect when the

current was larger than 160 mA (Fig. 2.7F), the cooling effect of the TED under the mild forced convection condition can be greater than 10 °C.

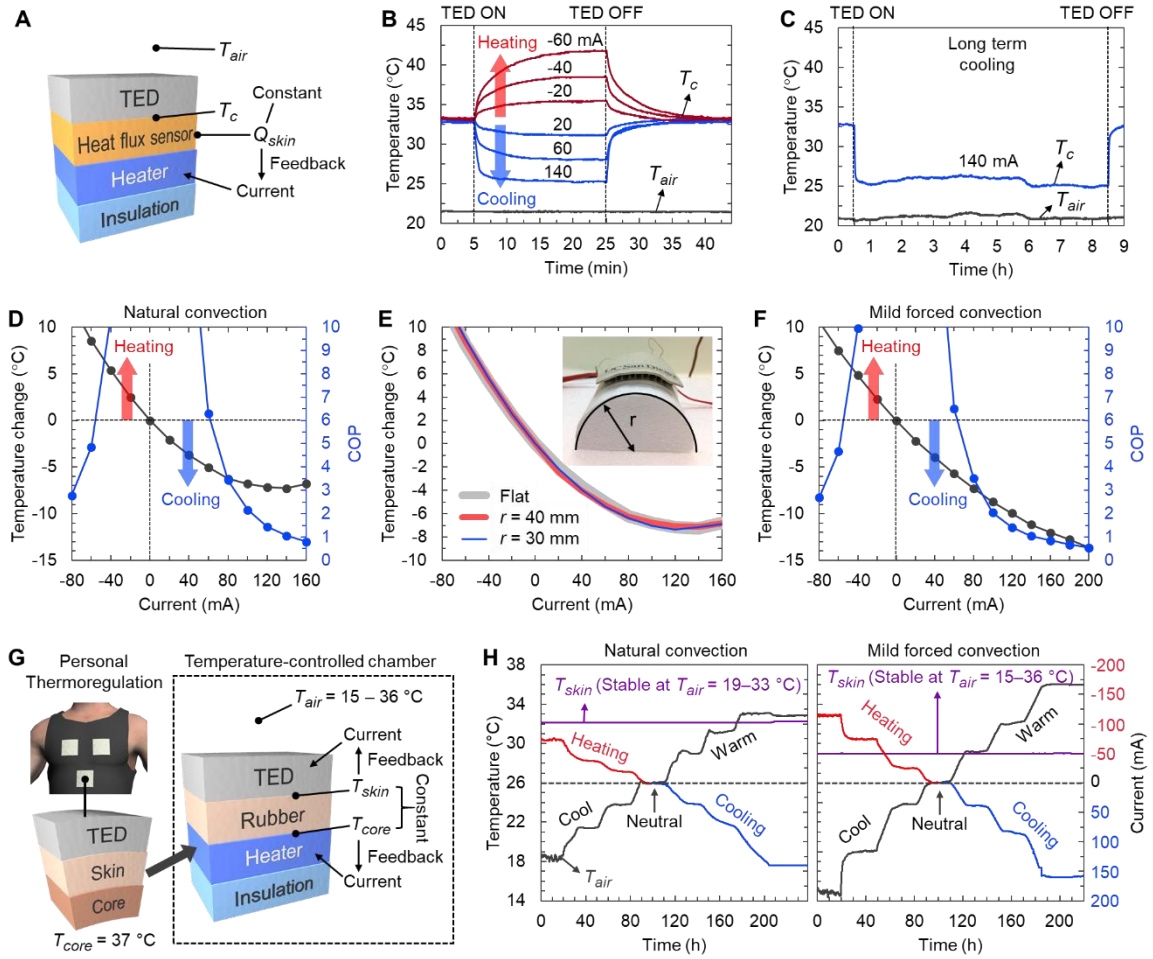


Figure 2.7 Cooling and heating performance. (**A**) Laboratory cooling/heating measurement setup. The heating power of a heater (Q_{skin}) was fixed at 87 W m^{-2} (measured by a heat flux sensor) to simulate the typical metabolic rate from a human. (**B**) Time-dependent cooling/heating effects from the TED. (**C**) Sustainable cooling effect for a long period (8 h) with an electrical current of 140 mA. (**D**) Summary of temperature changes (black) and COP (blue) during TED operation with natural convection. The maximum temperature decrease was 7.3 °C. (**E**) Summary of temperature changes (black) and COP (blue) during TED operation with mild forced convection (5 km h^{-1} wind). The maximum temperature decrease was more than 13.6 °C. (**F**) Cooling/heating effects for bending radii (r) of 30 and 40 mm, showing no change compared with those on the flat setup. The inset shows the measurement setup to test the cooling/heating effect of the TED under bending. (**G**) Schematic of a human skin setup to demonstrate TED thermoregulation. (**H**) Thermoregulation measurement results. The surface temperature of the PDMS layer (T_{skin}) was maintained by TED cooling and heating within the entire range of ambient temperature.

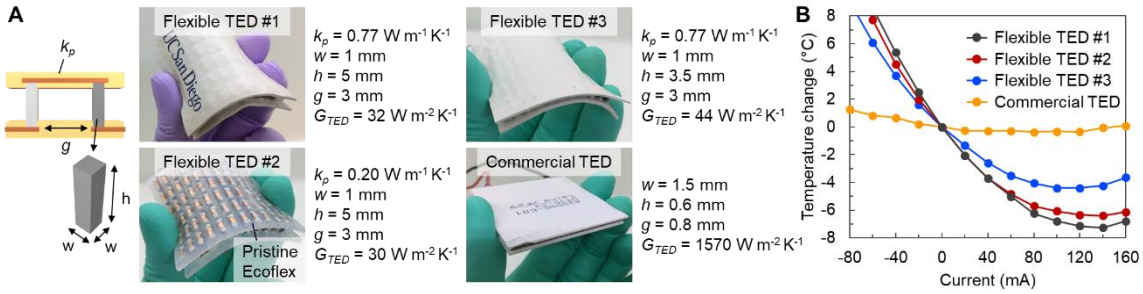


Figure 2.8 Comparison of TEDs. (**A**) Four TEDs with various TE pillar designs and thermal conductivity values of the stretchable polymer sheets (k_p). The four devices included three flexible TEDs and a commercial TED made of the same TE materials. The geometric and thermal parameters of the TEDs are summarized in the schematics. (**B**) Summary of cooling/heating effects. The flexible TEDs showed the maximum cooling of 4.6 °C (blue), 6.3 °C (red), and 7.3 °C (black) while the commercial TED (yellow) did not show any cooling effect. The significantly improved cooling in the flexible TEDs is attributed to our optimal thermal design featured with low G_{TED}.

2.5 Thermoregulation on Human Skin using Flexible TED

The flexibility of our TED makes it well suited for personalized thermoregulation as a wearable device. To demonstrate personalized thermoregulation on human skin under realistic conditions, we integrated the flexible TED into a garment and attached it onto the arm of a human subject. As shown in Fig. 2.9A, a thin porous mesh fabric was used to cover the TED without impeding the heat dissipation while an elastic nylon fabric was used to wrap the TED around the arm. A thermocouple was used to monitor the temperature of the skin covered by the TED (T_{skin}) while the subject was exposed to a controlled thermal environment within a wide temperature span of 22 °C to 36 °C. A PID controller was used to adjust the current applied to the TED to maintain T_{skin} at the comfort temperature (32 °C) regardless of the ambient temperature. At each ambient temperature set point (namely, 22 °C, 26 °C, 29 °C, 31 °C, 34 °C, and 36 °C), the current to the TED was initially turned off (TED OFF) during the first 5 min, and the corresponding T_{skin} was monitored, as shown in Fig. 2.9B. As expected, the T_{skin} largely followed the ambient temperature: T_{skin} varied from 28.5 °C to 34.3 °C as T_{air} was changed from 22 °C to 36 °C. After the first 5 min, the TED was turned on with its applied current automatically adjusted by the PID controller with a temperature set point of 32 °C. As shown in Fig. 2.9B, the measured skin temperature reached the set point within 2 min and then remained at the set temperature thereafter regardless of whether the ambient temperature was lower (heating from TED) or higher (cooling from TED). This fast thermal response from the TED followed the same behavior as the laboratory setup (Fig. 2.7B). The precise and adjustable skin temperature control offered by the TED highlights the unique

advantages of TE thermoregulation compared with other approaches, such as water or ice packs, which are not controllable.

We also used an infrared camera (E60, FLIR) to image the skin and TED to visualize the active heat pumping effect. Fig. 2.9C shows the TED hot-side temperature of approximately 42 °C for the maximum cooling condition, which illustrates the active heat pumping from the cold (skin) side to the hot side. The hot-side temperature is also consistent with h_{air} (~11 W m^{-2} K^{-1}) and the heat dissipation to the environment (skin metabolic heat plus TED power consumption, see note S2). Fig. 2.9D presents an IR image of the residual cooling effect on the skin immediately after removing the TED. The IR image clearly shows ~2.5 °C cooling on the skin under the area originally covered by the TED compared with the rest of the skin.

The achievement of precisely controllable thermoregulation using the flexible TED has significant implications, which can be best illustrated by the distinctly different skin temperature responses to ambient temperature variation with and without TED operation (Fig. 2.9E). The typical comfort temperature range of human skin is 31.5 °C to 32.5 °C, which corresponds to an ambient temperature range of 28 °C to 30 °C without the TED[15,56]. When the TED is operating, however, the skin temperature can be maintained at a constant comfort temperature of 32 °C even within the wider ambient temperature range of 22 °C – 36 °C, thus simultaneously broadening the comfortable ambient temperature zone from 2 °C (T_{air} = 28 °C – 30 °C) to 14 °C (T_{air} = 22 °C –36 °C) and enhancing the wearer's thermal comfort. This 14 °C of comfortable ambient temperature zone with the TED operation matches with the results obtained by our human skin setup (Fig. 2.7H). The broadening of the ambient temperature set points could lead to substantial energy savings for indoor centralized HVAC

systems, by as much as ~0.8 kW per person or 20% for a typical building, according to energy analysis[7,57]. Notably, this building-level energy savings is achieved with negligible energy consumption by the TED, as expected from the measured high COP of our TEDs (Fig. 2.7, D and 4F). We also directly measured the power consumption of the TED when cooling the skin, which was determined to be only about tens of watts per person, depending on the ambient temperature (see details in Fig. 2.10). Therefore, our results directly point to the tremendous energy savings potential offered by individualized thermoregulation using our flexible TEDs.

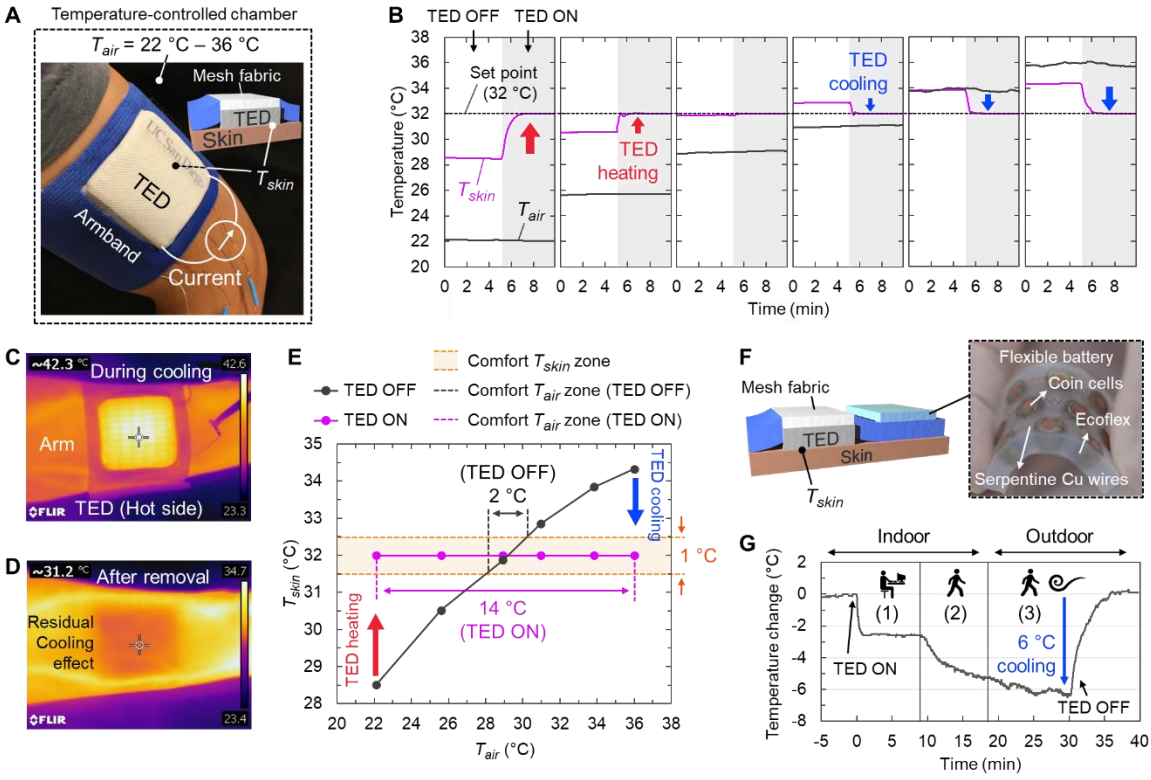


Figure 2.9 Demonstration of thermoregulation on human skin. (**A**) Photograph and schematic diagram of the TED armband. The wearer's arm was encompassed by a controlled thermal environment. (**B**) Change in T_{skin} under various T_{air} conditions before and after TED operation. Without TED operation, T_{skin} varied from 28.5 °C to 34.3 °C while T_{air} changed from 22 °C to 36 °C. With active thermoregulation of the TED, T_{skin} converged to the preset comfort temperature (32 °C) under all the T_{air} conditions. (**C**) Infrared image of the TED armband (hot side) during cooling (I = 160 mA) on the subject's arm. (**D**) Infrared image of the skin after removing the TED armband, showing residual cooling effect. (**E**) Summary of T_{skin} as a function of T_{air} with and without TED operation. The cooling and heating of the TED broadened the comfortable ambient temperature zone from 2 °C (T_{air} = 28 °C – 30 °C) to 14 °C (T_{air} = 22 °C – 36 °C). (**F**) Schematic of the TED armband integrated with the flexible battery pack (photograph). (**G**) Skin temperature change by TED cooling under three conditions: (1) sitting indoors, (2) walking indoors, and (3) walking outdoors under mild wind conditions. The maximum skin cooling effect was 6 °C.

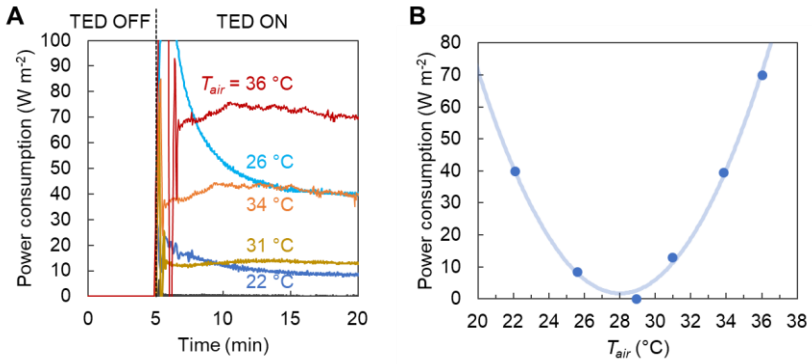


Figure 2.10 Power consumption during the thermo-regulation of human skin. (**A**) Power consumption of the TED during thermoregulation at various air temperatures T_{air}. (**B**) Summary of the power consumption as a function of T_{air}.

2.6 Integration of TED with Flexible Batteries for Mobile Thermoregulation

We also demonstrated the mobility of our wearable TED by integrating it with a flexible battery pack to produce an all-flexible personalized thermoregulation device. The power pack was fabricated by embedding ten coin-cell batteries into an Ecoflex matrix and connecting them to each other with serpentine copper electrodes such that their flexibility matched that of the TED (see Materials and Methods for details)[58]. Fig. 2.9F shows an integrated cooling armband with the flexible battery pack. The device was tested under three realistic conditions to investigate the effect of various convection and metabolic conditions, as shown in Fig. 2.9G and Fig. 2.11: 1) sitting in an indoor environment without wind to represent typical office conditions; 2) walking indoors at a speed of ~5 km h^{-1} to test the cooling effect under enhanced metabolic rate and convection conditions; and 3) walking outdoors at a speed of ~5 km h^{-1} under mild wind conditions to verify the feasibility of the TED for outdoor usage (see Materials and Methods for details).

When the TED was initially turned on with the flexible battery pack (I = 120 mA), the skin temperature decreased rapidly by up to 2.5 °C, which matches well with the temperature drop shown in Fig. 2.9B and E. This temperature drop was stable as long as the wearer was sitting still (condition 1). When the wearer started walking under the second condition, the temperature drop doubled, up to ~5 °C, because of the forced convection effect during walking, which is consistent with the trend observed in the laboratory setup under the mild forced convection condition (Fig. 2.7F). The last condition additionally increased the temperature drop to up to 6 °C because of the even higher convection effect from the synergy

of walking and the wind outside. This 6 °C skin cooling effect of the 5×5 cm^2 TED consumed only ~180 mW of power, or 1.8 Wh of energy for 10-h operation, which can be supplied by ~9 g of batteries (assuming a battery energy density of ~200 Wh kg^{-1})[59]. Considering a cooling vest made of 144 of such TEDs to cover the hotspots of on the skin (e.g., back, chest, and abdomen) with an area of ~3600 cm^2 (~20% of the total body area), the power consumption is calculated to be ~26 W. Moreover, under the mild forced convection, the power consumption of the cooling vest is expected to be reduced by ~45%, to ~14.3 W, based on the results from the laboratory setup (Fig. 2.7F). This energy consumption can be readily supplied by a battery pack with a weight of ~430 grams for approximately 6 hours of operation.

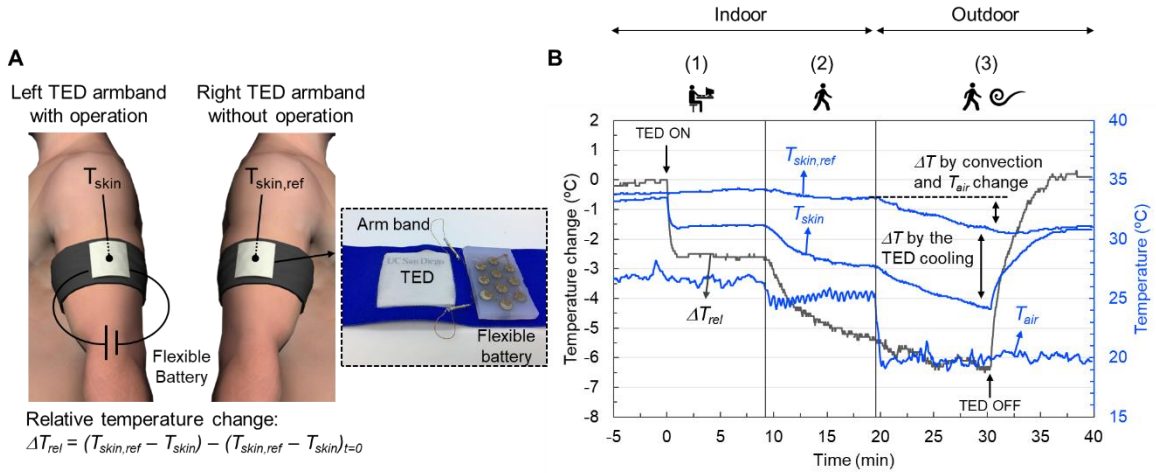


Figure 2.11 Temperature change during the mobile thermoregulation demonstration. (**A**) Schematics of the demonstration setup with two identical TED armband worn on both arms, but the TED on the left armband was operating (i.e., applied with current from the flexible batter) and the other TED on the right armband was not operationg and used as a reference. The relative temperature change was determined by subtracting T_{skin} from $T_{skin,ref}$ to exclude possible skin temperature changes caused by changes in air temperature, convection heat transfer coefficients, and metablic rates. The inset shows the integrated TED arm band with the flexible battery pack. (**B**) Measured temperature during the demonstration. T_{skin} and $T_{skin,ref}$ were almost the same before and after demonstration because the TED armbands and heat generation from both arms are identical. $T_{skin,ref}$ drifted as changing thermal conditions, and compensate the change to extract the active cooling effect from the TED.

2.7 Materials and Methods

2.7.1 Fabrication of Flexible TED

The processes used to fabricate the flexible TED are schematically illustrated in Fig. 2.1F. First, commercial TE alloys were cut into pillars that were 1×1 mm^2 in area and 5 mm in height. The TE pillars were aligned into a 12×12 array with 3-mm spacing between adjacent pillars. The array was attached to a carrier substrate using a thermal responsive adhesive as the first step. A Cu film (35 μm in thickness) with a solvent-soluble adhesive was attached to another carrier substrate for the fabrication of the top electrodes. The Cu film on the carrier substrate was cut into individual electrodes (1.5 mm in width and 5.5 mm in length) for each pair of TE pillars, and the residual Cu film was removed from the carrier substrate (Fig. 2.2A). A polyimide tape was attached to the electrodes as a solder mask opening only the parts that contact with the TE pillars. The Cu electrodes on the carrier substrate were soldered to the TE pillar array using a soldering paste (Fig. 2.2C). After detaching the carrier substrate and solder mask from the Cu electrodes by soaking the device in acetone, a SiO_2 layer (200 nm) was deposited onto the electrodes to improve the adhesion with the stretchable polymer sheet. Next, 1-mm-thick Ecoflex 00-30A/B (Smooth-on) containing 26 vol.% of AlN powder (10 μm in diameter, Sigma-Aldrich) was cured, embedding the electrodes and the small segment (0.5 mm) of TE pillars. The Ecoflex and AlN powder mixture film with the electrodes and TE pillars was cut to dimensions of 5×5 cm^2, and the carrier substrate for the TE pillars was detached by applying heat to melt the heat-responsive adhesive. The aforementioned process was repeated for the bottom layer fabrication.

2.7.2 Thermoelectric Characterization of TED

The thermal conductance of the TED (G_{TED}) was measured by applying heating power (Q) to the TED and measuring the temperature difference between the hot and cold sides ($\Delta T = T_h - T_c$, where T_h is the hot-side temperature and T_c is the cold-side temperature.). G_{TED} was calculated using $G_{TED} = d(Q)/d(\Delta T)$. The Seebeck coefficient (S) was also measured using the same setup by additionally measuring V_{OC} of the TED for various temperature differences. The device-level average Seebeck coefficient was calculated from the slope of V_{OC} vs. ΔT, namely, $S = d(V_{OC})/d(\Delta T)$. The thermal conductivity of the stretchable Ecoflex sheets (k_p) was measured using the same method as that used for the G_{TED} measurement, and the measurement was calibrated with standard polymer samples, including pristine Ecoflex (k_p = 0.20 W m^{-1} K^{-1}).

2.7.3 Measurement of Cooling/heating Performance of TED

For the laboratory setup shown in Fig. 2.7A, a thin film heater and a heat flux sensor (PHFS-01, FluxTeq) were used to simulate metabolic heat from a human body. During the measurement, the heater power was PID controlled to maintain a constant heat flux (Fig. 2.12). A polystyrene foam insulation layer was placed underneath the heater to prevent parasitic heat loss. A thermocouple was placed under the TED to measure T_c, and the other thermocouple was located ~20-cm away from the TED to monitor the ambient temperature (T_{air}). The cooling and heating effect at each electrical current was measured for 60 min: 20 min for pre-stabilization of the temperature without an electrical current, 20 min of TED operation with the current ranging from −80 mA to 160 mA (−80 mA to 200 mA for the

forced convection condition), and 20 min of post-stabilization of temperature after switching off the electrical current. The temperature change in the summary results (e.g., Fig. 2.7D) was defined by the temperature difference of T_c shortly before switching on and off the TED. The cooling/heating measurements were repeated three times (Fig. 2.9C and D), and the root mean square error was less than 0.3 °C. The temperature increased when a negative current was applied to the TED and decreased when a positive current was applied. For cooling, with increasing current, the temperature decreased almost linearly because of the Peltier effect and then began to saturate and eventually increased because of the excessive Joule heating. However, when a negative current was applied for heating, the temperature continued rising without saturation as the electrical current decreased because of the combined Peltier and Joule heating effects.

The COP was determined using

$$COP = \frac{Q_{skin}}{W} = \frac{Q_{skin}}{SI\Delta T + I^2R}, \tag{2.7}$$

where Q_{skin} is the metabolic heat from a human body ($Q_{skin} = 87\ W\ m^{-2} \times A$), A is the area of the TED, W is the supplied power, I is the applied electrical current, and R is the internal electrical resistance of the TED.

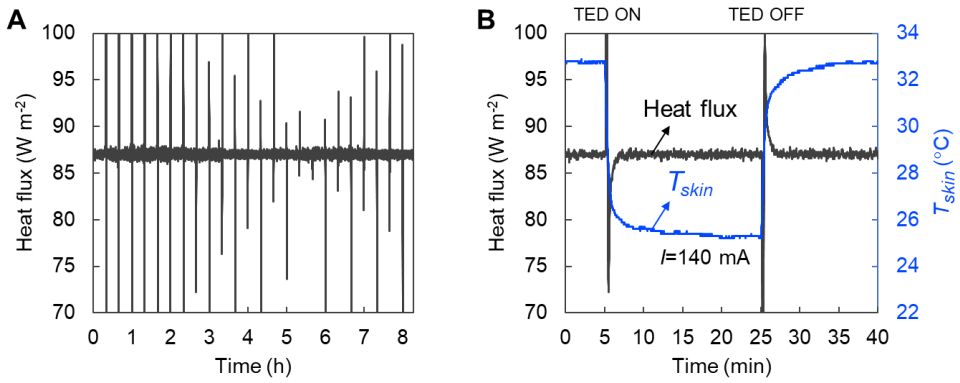


Figure 2.12 PID control of the heat flux from the heater. (**A**) Measured heat flux applied to the heater during cooling/heating measurement. The heating power was maintained at a constant 87 W m^{-2} value using a PID controller, with the feedback from the heat flux sensor. (**B**) An example of heat flux recovery graph with the PID controller after switching on/off the TED. When the TED was switched on at the electrical current of 140 mA, the cooling of the T_{skin} increased the heat flux from the insulation layer to the TED bottom. On the contrary, switching off the TED decreased the heat flux. The PID controller recovered the heat flux within two minutes.

2.7.4 Measurement of TED Performance on Human Subject

The armband was fabricated by attaching a piece of mesh fabric (90% nylon and 10% spandex) onto a square hole (~6×6 cm^2) of a nylon elastic fabric strip with fabric adhesive. The TED was sandwiched between the mesh fabric and skin during the measurement. A healthy male subject with normal body mass index was recruited, and the cooling/heating effect of the TED armband was measured on the wearer's arm, as shown in Fig. 2.9A. A temperature-controlled chamber was designed to locally regulate the ambient temperature (T_{air}) near the arm considering the small areal density of the TED relative to the surface of a human body. T_{air} in the chamber was controlled by a heater with thermally insulating fabric covering the chamber to prevent heat loss. A small hole in the chamber was prepared to place the subject's arm. Before the measurement, the subject sat and relaxed under a thermal comfort condition while placing an arm in the chamber and waited for more than 1 h for stabilization of the metabolic condition and T_{air} in the chamber. There were no sources of forced airflow such as movement of the subject or ventilation during the measurement. The current applied to the TED was PID controlled to maintain T_{skin} at the comfort temperature of 32 °C (Fig. 2.9B). After T_{skin} reached steady state, T_{skin} and T_{air} were recorded for 10 min, and the TED was switched after 5 min.

2.7.5 Fabrication of Flexible Battery Pack

A piece of copper sheet (20-μm thick, Oak-Mitsui, Inc.) was first spin-coated with amic acid precursor [poly(pyromellitic dianhydride-co-4,40-oxydianiline), HD-PI2545, HD MicroSystems] followed by soft baking at 110 °C for 3 min and at 150 °C for 1 min to fully

remove the solvents. The thickness of the polyimide (PI) film after baking was 2 μm, which was determined from the spin-coating parameters (4000 rpm, 1 min). Hard baking of the PI film was performed at 300 °C for 1 h in a nitrogen gas oven to achieve complete crosslinking and curing of the PI. The copper/PI sheet was then laminated on a piece of glass slide coated with polydimethylsiloxane (PDMS, Sylgard 184 silicone elastomer, 15:1) with the PI layer contacting the PDMS. Before lamination, both the PI and PDMS surfaces were activated with ultraviolet (UV) light (PSD series Digital UV Ozone System, Novascan) for 2 min. The island-bridge serpentine structure was designed with AutoCAD software and then patterned using pulsed laser ablation (Laser Mark's) on the copper sheets. The laser parameters (central wavelength of 1059–1065 nm, power of 0.228 mJ, frequency of 35 kHz, speed of 300 mm s^{-1}, and pulse width of 500 ns) were optimized for the copper sheet ablation. In a coin-cell battery array, two such electrodes, a cathode (+) and an anode (−), are needed. The patterned electrode was then transfer-printed with water-soluble tape (3M) to a silicone superstrate/substrate (300 μm, Ecoflex, Smooth-On Inc.) with the PI layer contacting the silicone layer. The Ecoflex superstrate was prepared by mixing two parts of its precursor components (1:1 volume ratio), spin coating at 100 rpm for 1 min, and crosslinking on a hotplate at 60 °C for 30 min. To improve the bonding strength between PI and the Ecoflex layer, UV activation was applied followed by baking at 80 °C for 10 min in a convection oven. The water-soluble tape was rinsed off with deionized water.

For these tests, we adopted coin-cell batteries operated by an aqueous-based electrolyte (XR48, ZPower LLC.). These batteries provide a stable and non-flammable electrochemistry, which is suitable for wearable applications. The coin cells were connected

in parallel and bonded to the first copper electrode with a silver-epoxy conductive adhesive (EPO-TEK H20E, Epoxy Technology) at 80 °C for 4 h in a convection oven. The second electrode was aligned with the pre-bonded coin cells under a stereomicroscope and bonded with the silver-epoxy adhesive using the same method. Next, two copper wires were soldered to the specific island pads on both the anodic and cathodic copper electrodes. Then, the gap between the sandwiched device was filled with Ecoflex and cured at room temperature for 4 h. Finally, a free-standing stretchable coin-cell battery array was obtained after removing the two pieces of glass slides.

2.7.6 Demonstration of Mobile Application of TED with Flexible Battery Pack

Two identical TED armbands were prepared for this demonstration. The TED armbands were attached to both of the subject's arms; one of the TEDs was operated using the flexible battery pack during the demonstration while the other was not operated (Fig. 2.11A). Along with the skin temperature under the TED with operation (T_{skin}), the skin temperature under the TED without operation ($T_{skin,ref}$) was monitored as a reference to compensate for the passive cooling/heating effects by thermal condition changes (e.g., wind, ambient temperature, or metabolic heat generation). The relative temperature change (ΔT_{rel}) from the active TED cooling was calculated using $\Delta T_{rel} = (T_{skin,ref} - T_{skin}) - (T_{skin,ref} - T_{skin})_{t=0}$. The similar T_{skin} and $T_{skin,ref}$ values before and after measurement (Fig. 2.11B) indicate that both arms and TEDs were exposed to identical thermal conditions (e.g., thermal insulation and metabolic heat generation).

2.8 Conclusions

In summary, we developed, for the first time, a flexible and wearable TED with large, sustainable, controllable cooling and heating effect with a high COP for personalized thermoregulation. The TED is sufficiently thin, flexible, light, and readily embeddable into a garment. The wearability of the TED is uniquely achieved by eliminating the need for the large heat sinks (e.g., fin or fan) typically employed in traditional devices and by exploiting high-aspect-ratio TE pillars with an air gap to achieve low thermal conductance in the TED. We achieved a large cooling effect of up to 13 °C in the TED without the use of a heat sink, which will provide sufficient thermoregulation for human thermal comfort. We also integrated the thermoelectric devices into a wearable garment and demonstrated the long-term, energy-efficient cooling and heating effects on human skin: the garment maintained the skin at the comfort temperature of 32 °C while the ambient temperature varied from 22 °C to 36 °C. The high COP of the TED and the localized cooling capability offer tremendous energy savings potential for personalized cooling compared with traditional centralized space cooling approaches. Thus, wearable garments based on the TED developed in this work may revolutionize the century-old cooling technology for climate control in buildings and vehicles.

Chapter 2, in full, has been submitted for publication of the material, Sahngki Hong, Yue Gu, Joon Kyo Seo, Joseph Wang, Ping Liu, Y. Shirley Meng, Sheng Xu and Renkun Chen. The dissertation author was the primary investigator and the first author of this paper.

Chapter 3

Wearable Thermoelectrics for Thermal Camouflage

3.1 Introduction

Camouflage is an essential skill commonly seen in nature[60-63] and technical/scientific applications[64,65], matching the intensity and patterns of a certain spectrum range (e.g., visible, infrared (IR), radar radiations) with surroundings. While visual camouflage has exploited for a few million years of human history and achieved success[64-66], thermal camouflage suddenly attracted great attention for a recent century owing to the development of IR surveillance technology[67-70]. However, the thermal camouflage technology is still primarily limited by the intrinsic difficulty of handling IR radiation, intimately connecting with temperature and emissivity (ε) by Stefan-Boltzmann law. The objects desired to be hidden (e.g., a human body or a vehicle) emit IR rays by themselves unlike visible light, and control of the IR radiation and the consequent temperature change of the objects affect their functions, for instance, blocking the heat from the vehicles causes overheating or cooling the surface of a human body leads hypothermia[6].

Due to the given inherent limitations, past studies have been focused on cheating IR detectors by manipulating emissivity[71-80] or conduction[81-85], avoiding the direct temperature

control. Notably, the emissivity manipulation has been served as a golden standard with both pre-controlled[77-80] or adjustable emissivity coatings[71-76] whereas the manipulation of conduction is still investigated in a fundamental level under only precisely controlled conditions such as conductive medium with a uniform temperature profile. Although many studies showed thermal camouflage effect with the emissivity manipulation, the camouflage effect can be largely interrupted by surrounding conditions due to inherent high reflectance (low emissivity) for mitigating the IR radiation from the objects to be hidden. For instance, a reflection of hot/cold spots in nature (e.g., the sun or sky) or contamination with high emissivity materials (e.g., raindrops or dust)[86,87] possibly ruins the camouflage effect. Further, the temperature range that can cheat IR detectors with the emissivity manipulation are limited; the maximum temperature cannot be higher than the temperature of heat sources when the IR emission is 100% ($\varepsilon = 1$), and minimum temperature cannot be lower than the ambient temperature when the IR reflection is 100% ($\varepsilon = 0$).

Recently, some studies suggested possibilities of non-reflective and active IR camouflage by direct manipulation of the surface temperature of the objects such as injecting hot or cold liquid through microfluidic channels on a soft robot's skin[64] or utilizing thermoelectric devices (TEDs) on vehicles[88] or blankets[89]. However, although those technics were successfully demonstrated on machines, active IR camouflage on a human body remains a great challenge due to the poor wearability and portability of the previous approaches; they need bulky fluidic channels with a pump system or rigid TEDs with large heat sinks that are not suitable for a wearable application. In contrast, the flexible TED that we previously demonstrated have shown sufficient wearability, portability, and temperature-

regulation performance without bulky heat sinks, which is suitable for a personal thermal camouflage by controlling the surface temperature of the flexible TED.

Here, we demonstrated personal thermal camouflage based on the flexible TED which is adaptable to the background temperature changes. The TED is sufficiently thin, portable, and flexible to be embedded in a garment thanks to the optimized thermal and mechanical designs. The TED provided active and precise thermal camouflage hiding heat from a heater setup under various background temperature. The camouflage effect was not interrupted by the reflection of surroundings since the TED has low IR reflectance. Finally, we also demonstrated the camouflage effect on human skin with an armband embedding the TED supported by a flexible phase change material (PCM) heat absorbing layer. This novel wearable thermal camouflage may pave the way for personalized and environment adaptable thermal camouflage.

3.2 Design

Thermal camouflage requires to adapt thermal patterns of the object to the background where the background thermal radiation varies depending on the materials and thermal conditions (e.g., hot rocks under the sun or cool plants with evaporation). The active thermal camouflage with the TED can be done by controlling the surface temperature of the TED (T_{TED}) and matching it with the background temperature (T_{back}) to hide the metabolic heat from a human body as illustrated in Fig. 3.1A. In our previous study [ref], we showed that the flexible TED was able to eliminate heat sinks which hinder the wearability by reducing thermal conductance between cold and hot sides (G_{TED}) with thin thermoelectric

pillars (1×1 mm^2 in area and 5 mm in height) and large air gaps between them (Fig. 3.1C). The TED was highly durable under bending stress (Fig. 3.1B) because the top and bottom stretchable polymer sheets (Ecoflex and AlN particles mixture) expand or contract, absorbing the most of bending stress and protecting the embedding rigid TE pillars from the mechanical stress. AlN particles in Ecoflex improves lateral heat conduction within the top and bottom sheets for efficient heat spreading to prevent the heat on the hot side flowing backward to the cold side that also accounts for the high thermo-regulation performance without heat sinks.

The TED was able to adjust the surface temperature by more than ±15 °C (Fig. 3.1D). When the metabolic rate from a human body with light activity (50 – 100 Wm^{-2}) and a mild convection with the heat transfer coefficient from the TED to the air (h_{air}) of 10 – 20 $Wm^{-2}K^{-1}$, the temperature difference between the T_{TED} and the ambient temperature (T_{air}) is expected to range from 2.5 °C to 10 °C depending on the thermal conditions. Considering the 15 °C cooling on the TED surface, the camouflage can be sufficiently operated in the most of conditions including the case when the T_{back} is even lower or higher than T_{air} due to solar radiation or evaporative cooling.

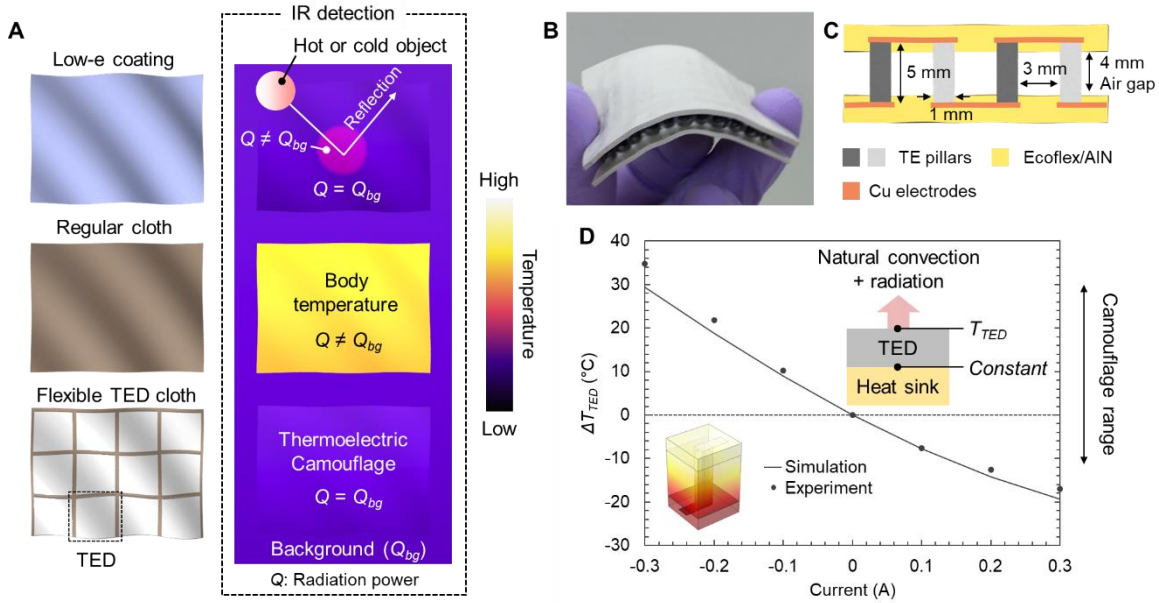


Figure 3.1 A concept of thermal camouflage by the flexible TED. (**A**) Schematics of thermal camouflage with the low-e coating and flexible TED cloth. While the regular cloth cannot hide radiation power from a human body and the low-e coating reflects cold and hot spots of surroundings, the flexible TED cloth can camouflage the human body by Peltier cooling/heating without reflection. (**B**) Photograph of the fabricated flexible TED. (**C**) The design of our TED. High flexibility and cooling/heating performance were achieved by high performance (ZT = 0.71) and large height (5 mm) to area (1×1 mm^2) ratio TE pillars sandwiched by two stretchable sheets (Ecoflex and AlN particles mixture) with a large air gap. Also, the Ecoflex and AlN particles mixture heat spreading layers enable the TED flexible. (**D**) Experiment and simulation results of the temperature change on top of the TED (ΔT_{TED}) as a function of electrical current. The inset schematic shows the measurement system. The bottom temperature of the TED was maintained by a heat sink, and electrical currents were applied to the TED, resulting in Peltier cooling/heating on top of the TED. The camouflage temperature range was more than ±15 °C.

3.3 Active Thermal Camouflage

We demonstrated the active thermal camouflage performance of our TED compared with the low emissivity (low-e) film, which has been served as a golden standard of passive thermal camouflage. As displayed in Fig. 3.2A, both the TED and the low-e film were placed on a heater maintaining its surface temperature at 28 °C to mimic metabolic heat generation from a human body in rest. The heater was suspended on a temperature controller (20×20 cm^2) covered with high emissivity polymer tape to simulate background temperature change. IR camera (E40, Flir) recorded the temperatures while T_{back} changes in the range of 14 – 34 °C at the constant ambient temperature (T_{air} = 20 °C). The details of the measurement setup and concept are described in Fig. 3.2E and F. While the TED interacted with ambient with the heat transfer coefficient of $h_{air} \approx 10$ $Wm^{-2}K^{-1}$ with natural convection and mild ventilation in the laboratory, low-e film had convection heat transfer (h_{rad}) without radiation due to its low emissivity, which results in the surface temperature of 28 °C ($T_{low\text{-}e}$). The temperature change of the temperature controller did not affect the temperature of the heater setup due to the air gap between the heater and the temperature controller and an insulation layer at the bottom of the heater (Fig. 3.2E).

As displayed in Fig. 3.2B, when $T_{air} = T_{back}$, the low-e film was camouflaged despite its higher surface temperature ($T_{low\text{-}e}$) compared to T_{back} since the film reflects the thermal radiation from surroundings (T_{air}), instead of emitting its thermal radiation (Fig. 3.2F). The TED also showed the camouflage effect by controlling T_{TED} and emitting the thermal radiation matched with the background (Fig. 3.2E). However, when T_{back} was changed, the camouflage effect was not maintained in the case of low-e film while the TED was able to

camouflage with excellent temperature uniformity (Fig. 3.2C and D). During the camouflage, the temperature distribution on the TED was ±0.4 °C in terms of root mean square error as displayed with the temperature histogram in the inset graph of Fig. 3.2C. Since the temperature distribution was originated from the convective heat transfer at the side of the TED, even more accurate and uniform camouflage effect can be expected with larger TED. Fig. 3.2G shows the comparison of T_{TED}, T_{back}, and T_{air} as a function of time. As increasing T_{back} from 14 °C to 34 °C for 5 min, T_{TED} followed T_{back} by controlling the input power to the TED.

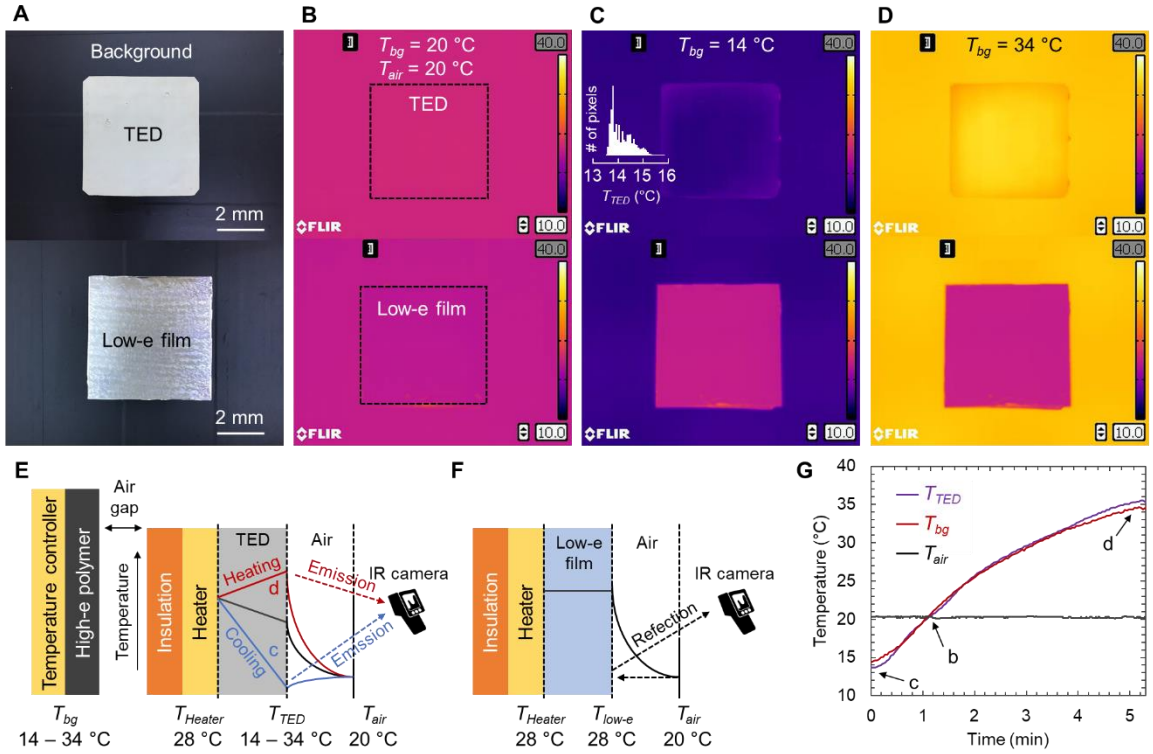


Figure 3.2 Active thermal camouflage by the TED. (**A**) Photographs of the TED (top) and low-e film (bottom) on the measurement setup. (**B**) IR images of the TED and low-e film with the same T_{back} and T_{air} of 20 °C. Both devices showed the camouflage effect. (**C and D**) IR images of the TED and low-e film at T_{back} = 14 °C (c) and 34 °C (d). The TED displayed the camouflage effect while the low-e film did not. (**E**) Schematic of the measurement setup with the TED. The heater temperature (T_{heater}) maintained at 28 °C to simulate human skin with clothing, and a temperature controller with high emissivity coating controlled T_{back} to demonstrate background condition change. The TED matched T_{TED} with T_{back} by Peltier cooling or heating. (**F**) Schematic of the measurement setup with the low-e film. While the surface temperature of the low-e film (T_{low-e}) was 28 °C, the IR camera read T_{air} instead of T_{low-e} due to its high reflectance. (**G**) Temperature change during the measurement. T_{TED} matched well with T_{back} within the background temperature of 14 – 34 °C.

3.4 Anti-IR Reflection Property

As discussed, one of the issues of the emissivity manipulation technology is that it needs low emissivity to block the thermal emission from a human body, resulting in inevitable reflection of surroundings. This high reflectance causes noticeably different thermal pattern compared to the background when there are hot or cold spots in nature such as the sun (4000 K) or sky (4 K); the reflection will be even easier to be captured by IR detector when human moves due to the change of the reflected thermal radiation. We demonstrated the issue caused by the low emissivity as shown in Fig. 3.3 Since the surface of the TED was composed of high emissivity polymer ($\varepsilon_{polymer} = 0.93$), the TED did not reflect the thermal radiation from a hand above the TED (Fig. 3.3C) while the low-e film which has $\varepsilon_{low\text{-}e} = 0.04$ obviously reflected the radiation from the hand (Fig. 3.3D), which was certainly detectable by an IR camera. The reflected thermal radiation of the hand showed the exact skin temperature (34 °C) suggesting the imperfection of the emissivity manipulation camouflage technic.

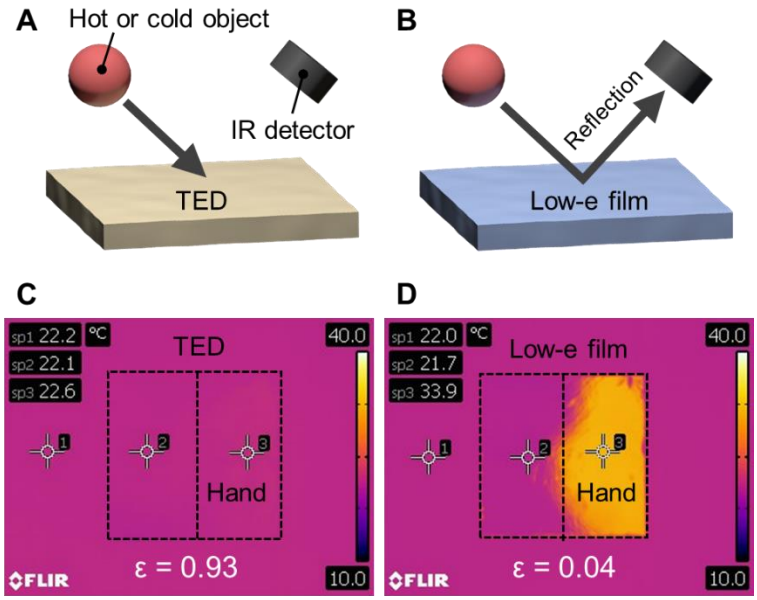


Figure 3.3 Anti-reflection property of the TED. (**A and B**) Schematics of IR reflection of hot or cold spots in nature that possibly ruins thermal camouflage effect. (**C**) IR image of the TED with high-emissivity polymer for anti-reflection. When a hand was placed above the TED to verify the reflection, the temperature reading of IR camera did not change. (**D**) IR image of the low-e film. Obvious IR reflection of the hand was observed.

3.5 Thermal Camouflage on Human Skin

We demonstrated the camouflage effect of the TED on human skin. The TED armband was fabricated for the demonstration: a regular fabric was used to wrap the TED around the wearer's wrist, and a mesh fabric was covered the TED to attach it on the armband without impeding the camouflage effect (Fig. 3.4A). Also, the low-e film was attached to the wrist as a comparison. The TED represented sufficient flexibility to conformally cover the wrist which has the bending radius of around 20 mm. During the test, the thermal conditions

(i.e., T_{air} and h_{air}) was maintained similar to the heater setup. As shown in Fig. 3.4D, T_{skin} without TED was 34 °C when the wearer in the thermally comfortable condition. After wearing the TED armband, T_{back} was changed from 16 °C to 38 °C; the TED was controlled to match T_{TED} with T_{back} (Fig. 3.4C). The results on human skin were consistent with the results on the heater: the TED showed the camouflage effect in the all range of T_{back} (Fig. 3.4E–G) while the low-e film only displayed the camouflage effect when $T_{back} = T_{air}$ since the film reflects the surrounding temperature.

During the thermal camouflage on skin, T_{skin} was maintained at its thermal comfort temperature of 34 °C despite the Peltier cooling or heating (Fig. 3.4C) without any harmful effect on skin. This temperature stability underneath the TED was mainly realized by a flexible phase change layer (PCL) between the TED and the fabric, which absorbed or emitted the heat to compensate for a temperature change from Peltier effect. The PCL was fabricated by embedding 2 g of phase change particles (MPCM28D, Microtek) in 3 g of Ecoflex. Theoretically, this 2 g of phase change particles can absorb ~400 J of energy and maintain the skin temperature for more than 20 min, however, more importantly, this PCL

can be replaced by any heat absorbing/emitting layers such as coolant circulation film or having a ventilation through the gap between the TED and skin.

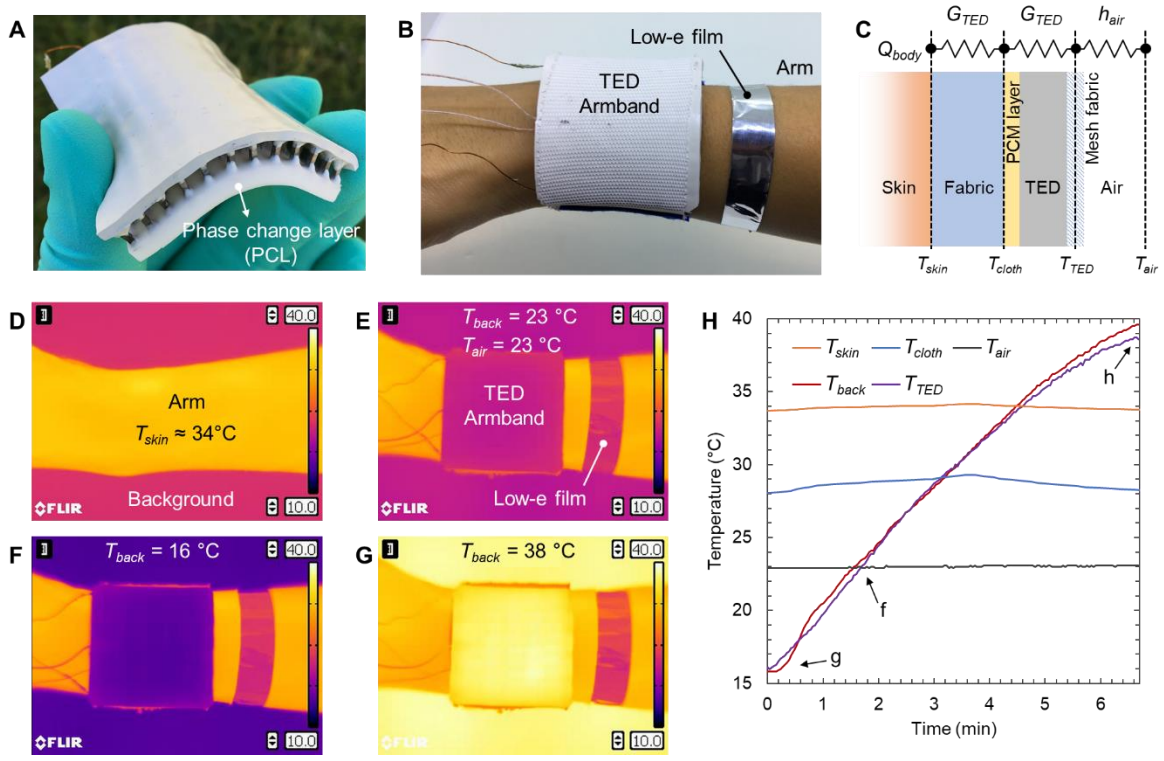


Figure 3.4 Thermal camouflage on human skin. (**A**) Photograph of the TED with phase change layer (PCL) as a flexible heat sink. (**B**) Photograph of the TED armband and low-e film on a wrist. (**C**) Schematic of the armband. A regular fabric wrapped around the wrist and the TED was attached on the armband with a mesh fabric. PCL absorbed or emitted energy to maintain the skin temperature (T_{skin}). (**D**) IR image of the wrist of a wearer. (**E-G**) IR images of the TED on human skin at T_{back} = 23, 16, and 38 °C respectively. Thermal camouflage effect was maintained in all the range of T_{back}. (**H**) Temperature changes during the measurement. T_{TED} and T_{back} matched well in T_{back} range of 16 – 38 °C (-7 °C and +15 °C compared to T_{air}) while PCM layer prevented T_{skin} change. (**I**) Long-term camouflage effect on the skin with PCM layer. The PCM layer containing 2 g of phase change particles maintained the camouflage effect for more than 30 min without overheating of T_{cloth}.

3.6 Conclusion

In summary, we developed a wearable and temperature adaptable thermal camouflage device based on thermoelectrics. Our flexible TED showed great temperature-regulation properties by optimization of thermal design: minimization of G_{TED} and maximization of lateral heat spreading within cold and hot sides. The TED showed highly accurate thermal camouflage effect in the T_{back} range of 16 – 38 °C (-7 – +15 °C compared to T_{air}) on human skin with the uniform temperature distribution on the TED (±0.4 °C). In addition, the TED camouflage assisted by PCL had minimal impact on human thermal condition, representing negligible T_{skin} change. The camouflage effect was not ruined by reflection due to its anti-reflection property (high emissivity) while the camouflage with the emissivity manipulated film (low emissivity) was easily interrupted by surroundings.

Chapter 3, in full, is currently being prepared for submission, Sahngki Hong and Renkun Chen. The dissertation author was the primary investigator and the first author of this paper.

Chapter 4

Single-cell Calorimetry

4.1 Introduction

Many biological reactions are tied inherently to heat generation or absorption, which can be measured by calorimetric methods[90]. Metabolic activities of microorganisms also involve heat generation as a product of adenosine triphosphate (ATP) synthesis and oxidative phosphorylation[91,92]. Calorimetry is powerful tool to investigate the metabolic activities since it is a non-invasive and label-free technique, which allow to monitor the metabolic behavior in real time without altering the nature of microorganisms[93-95]. Bacteria detection and cancer analysis are well-studied calorimetric applications. Calorimetry can diagnose bacterial disease by detecting metabolic heat of bacteria in patient's blood and even detect antibiotic resistance through dosage of drug options[96-99]. Abnormal metabolic activity of cancer cells also can be investigated by calorimetry and a large amount of research has been devoted to comprehending the relationship of metabolic heat and cancer[9,100-102].

Currently, the metabolic heat of cells is measured by averaging across the entire population of numerous cells. However, the average cell property does not represent that of individual cells[103,104] since the cells are heterogenous in many aspect such as type and amount of proteins[105,106], respiration rate[107], size and mechanical property[108], and division time[109], which are related to cell metabolism. Especially, heterogeneity of mitochondria such as diverse membrane potential, redox states, and calcium level causes various metabolic

behaviors of individual cells[110]. Calorimetry has a unique advantage to investigate these metabolic heterogeneities compared to other methods; for instance, calorimetry can provide the overall metabolic information including anaerobic metabolism which cannot be detected by oxygen consumption rate analysis[3,4,111]. However, whereas the heterogeneities have been widely investigated by optical[112], chemical[113], electrical[114] or mechanical[108] single-cell analysis (namely, cytometry), a method that can measure single-cell heat production has yet to be developed. This is mainly because the sensitivity of classical calorimeters is insufficient to measure the metabolic heat from a single cell. This poor sensitivity can be attributed to the inherent difficulty in measuring heat; various parasitic heat loss mechanisms such as conduction, convection, and radiation easily dissipate the tiny amount of heat from a single cell.

Hence, efforts to enhance the calorimeter sensitivity (Q_s) centered on minimizing thermal conductance (G) to suppress the parasitic heat loss as well as reducing minimum detectable temperature (T_{min}), where the sensitivity is determined by G and T_{min} ($Q_s = G \times T_{min}$). Especially, introduction of microfabrication technology to calorimeter enabled to integrate high-resolution temperature sensors and microfluidics-based sample transport system on thermally insulative thin membrane, resulting in significant improvement of the calorimeter sensitivity[115-125]. In addition to the high-sensitivity, the chip-calorimeters fabricated by this microfabrication technology also provide accurate sample handling and visualization: dosing stimuli onto microorganism or monitoring morphological change and population of cells in real time without disturbance of measurement[126,127].

This chip-calorimeters have evolved for a few decades to measure metabolic heat production by microorganisms. The most sensitive cell metabolic heat measurement was demonstrated by Johannessen et al.[126] with a chip-calorimeter possessing the sensitivity of as low as 13 nW. The calorimeter was able to measure 16.3 nW of metabolic heat from ten brown adipocytes stimulated with noradrenaline. A few years later, the state-of-the-art chip calorimeter with the sensitivity of 4.2 nW was developed by Lee et al.[115]. They achieved lowest thermal conductance by virtue of low thermal conductance backbone membrane in vacuum environment. However, the sensitivity is still larger than heat production by single cells even in cells with high metabolic rate such as *Tetrahymena* (~3 nW)[128-130]. Although Inomata et al.[131] detected unusually high metabolic heat from a single brown adipocyte more than 1 μW (a thousand times larger than other calorimetry results)[126,132], for a decade, no calorimeter has demonstrated better sensitivity than 4.2 nW[115] and measurement of normal single-cell metabolic heat ranging from a few picowatts to a few nanowatts.

Here, we present the first chip-calorimeter that can measure single-cell metabolic heat generation with 0.6 nW of high sensitivity. We achieved an order of magnitude greater sensitivity through an innovative one-dimensional suspended microfluidics design and a stable measurement platform with vacuum environment. Our magnetic cell trapping approach allows for reliable measurement without perturbation by the movement of cells and with supplement of sufficient amount of nutrients and oxygen to cells. Single-cell measurements using the calorimeter revealed that the metabolic rate and cell size of individual *Tetrahymena thermophila* follows the three-quarter power allometric scaling relationship. Finally, a mitochondrial uncoupling agent carbonyl cyanide 4-

(trifluoromethoxy)phenylhydrazone (FCCP) was dosed through the microfluidic channel to stimulate metabolic heat generation of *Tetrahymena* and analyze spare respiratory capacity (SRC). Given the potential to investigate the metabolic rate of each individual single cell, our single-cell calorimeter will open up a wide range of possible fundamental research to answer biological questions and provide an excellent platform for future biomedical applications.

4.2 Development of High-sensitivity Single-cell Calorimeter

Minimization of thermal conductance and minimum detectable temperature is imperative in development of high-sensitivity calorimeter. Our single-cell calorimeter achieved ultra-low thermal conductance by virtue of the novel one-dimensional suspended microfluidic tube design (Fig. 4.1A). This one-dimensional suspended design with small cross-sectional and surface area and long half tube length (L = 2.5 mm) significantly reduced conduction and radiation heat loss. In addition, a parylene backbone layer not only provided high mechanical strength and transparency but also large thermal insulation property because of its low thermal conductivity. The parylene backbone layer had the minimal width (120 μm) and thickness (12 μm) to form the microfluidic tube and embeds a temperature sensor with a narrow margin to create the one-dimensional design (Fig. 4.1B). The microfluidic channel had cross-sectional area of 35×50 μm^2, which is compatible for most cell sizes (< 35 μm in diameter). The entire tube structure is suspended on the silicon wafer with ~200 μm gap and surrounded by high vacuum environment (< 0.1 mTorr)[115] to eliminate convection heat loss.

A Bi-Pt thermopile and Pt heater were embedded in the parylene layer underneath the microfluidic channel as a temperature sensor and to characterize the calorimeter (Fig. 4.1C). The reference and measuring junctions of the thermopile were placed on Si wafer and the middle of the suspended tube (Fig. 4.1A), respectively. The thermopile measured the temperature difference (ΔT) between the measuring junctions (T_{mea}) and reference junctions (T_{ref}) while Pt heater measured the average temperature within the suspended tube and applied heat to the tube for device characterization. The thermopile was designed by optimizing the conflicting two variables, thermal conductance and temperature sensitivity.

For instance, thermal conductance rises as increasing the number of thermopile junctions for better temperature sensitivity, and electrical noise (e.g., Johnson noise or 1/f noise) of the thermopile, which diminishes temperature sensitivity, increases as reducing the width of thermopile layers to lower thermal conductance[12]. Our optimized thermopile was composed of four pairs of Bi and Pt thin films (Fig. 4.1C), and the root mean square voltage noise of the measurement system including the thermopile, an operational amplifier (CS3002, Cirrus Logic) and a low-pass filter (0.016 Hz of cutoff frequency) was 19 nV.

The overall thermal conductance of our calorimeter including the aforementioned components and water in the microfluidic channel was estimated as a function of the half tube length using a fin equation,

$$G = 2mkA_c\left(\frac{e^{mL} + e^{-mL}}{e^{mL} - e^{-mL}}\right) \tag{4.1}$$

where $m = \sqrt{\frac{hP}{kA_c}}$, k is the thermal conductivity, A_c is the cross-sectional area, P is the perimeter of the microfluidic tube, and h is radiation heat transfer coefficient ($h = 4\varepsilon\sigma T_{avg}^3$, where σ is the Stefan-Boltzmann constant, ε is the emissivity, and T_{avg} is the average temperature). The equation showed that the overall thermal conductance saturates at L = ~2.5 mm where radiation heat loss starts to get more dominant than conduction heat loss because of the large surface area (Fig. 4.2A). The estimated overall thermal conductance with 2.5 mm of half tube length is expected to be 2.48 μW K^{-1}. It is worth noting that our calorimeter design almost reaches the limit of the optimization because the most dominant factor contributing the overall thermal conductance is water (48%, Fig. 4.2B).

The Eq. 4.1 was derived from an energy balance equation for the differential element (Fig. 4.2A):

$$q_x = q_{x+dx} + dq_{rad} \tag{4.2}$$

where

$$q_x = -kA_c \frac{dT}{dx}, \tag{4.3}$$

$$q_{x+dx} = q_x + \frac{dq_x}{dx}dx = -kA_c \frac{dT}{dx} - k\frac{d}{dx}\left(A_c \frac{dT}{dx}\right)dx, \tag{4.4}$$

$$dq_{rad} = hdA_s(T - T_\infty), \tag{4.5}$$

where q_x is the heat flux into the differential element, q_{x+dx} is the heat flux out of the differential element, k is the effective thermal conductivity of the calorimeter, A_c is the cross-sectional area of the calorimeter, h is the radiation heat transfer coefficient, dA_s is the surface area of the differential element, T is the temperature of the differential element, and T_∞ is the ambient temperature. By substitute Eq. 4.3, 4.4 and 4.5 into Eq. 4.2, the new expression can be written as,

$$-kA_c \frac{dT}{dx} = -kA_c \frac{dT}{dx} - k\frac{d}{dx}\left(A_c \frac{dT}{dx}\right)dx + hdA_s(T - T_\infty), \tag{4.6}$$

Assuming A_c is constant, the $dA_s = Pdx$, where P is the cross-sectional parameter, then the equation can be simplified and rearranged as

$$0 = \frac{d^2T}{dx^2} - \frac{hP}{kA_c}(T - T_\infty). \tag{4.7}$$

Now, let $T(x) - T_\infty = \theta(x)$. Eq. 4.7 can be rewritten as

$$0 = \frac{d^2\theta(x)}{dx^2} - m^2\theta(x), \tag{4.8}$$

where $m = \sqrt{\frac{hP}{kA_c}}$. By solving the linear homogenous second-order differential equation using the boundary conditions,

a) at $x = 0$, $\theta(0) = 0$,

b) at $x = L$, $\frac{d\theta(x)}{dx} = \frac{q}{kA_c}$,

Eq. 4.8 can be derived as:

$$\frac{q}{kA_c} = mC_1e^{mL} - mC_2e^{-mL}, \tag{4.9}$$

where,

$$C_1 = \frac{q}{kA_cm(e^{mL} - e^{-mL})}, \tag{4.10}$$

$$C_2 = -\frac{q}{kA_cm(e^{mL} - e^{-mL})}. \tag{4.11}$$

Therefore, the analytical solution for the temperature profile of the suspended tube with a point heat source can be rearranged and expressed as:

$$\theta(x) = \left(\frac{q}{kA_cm}\right)\left(\frac{e^{mx} - e^{-mx}}{e^{mL} + e^{-mL}}\right). \tag{4.12}$$

This analytical equation considers only a half of the suspended tube in actual calorimeter design. Therefore, the heat generation, q, has to be reduced by half to achieve the same temperature increase in the actual geometry. Then, the temperature in the middle of the tube is

$$\theta_{max} = \left(\frac{q/2}{kA_cm}\right)\left(\frac{e^{mL} - e^{-mL}}{e^{mL} + e^{-mL}}\right), \tag{4.13}$$

Finally, the thermal conductance ($G = q/\theta_{max}$) can be expressed as:

$$G = 2mkA_c\left(\frac{e^{mL} - e^{-mL}}{e^{mL} + e^{-mL}}\right). \quad (4.1)$$

The fabricated device was loaded in our measurement platform (Fig. 4.1D and E), which designed to minimize baseline temperature drift and provide the high vacuum environment. The baseline drift caused by external temperature agitation have diminished the sensitivity of previous chip-calorimeters[115,116,122-124] whereas the baseline stability is imperative to monitor long-term biological phenomena such as cell metabolism, division or differentiation[133]. We minimized the baseline drift by three-levels of insulation layers, temperature controllers, and radiation shields as well as stable and leakage-free fluid control system. With the measurement platform, the baseline temperature of our calorimeter was stable for a long period of time (10 hours, Fig. 4.3A) and under light irradiation or fluid flow.

The sensitivity of our calorimeter was demonstrated by heating the suspended tube with the Pt heater and monitoring voltage from the Bi-Pt thermopile. The heating power absorbed by the measuring junctions (Q_{abs}) gradually increased from 0 to 4 μW, and the voltage output from the thermopile was collected for 5 min at each absorbed power. Voltage output from the thermopile was converted to temperature signal (ΔT) by Seebeck coefficient (S = 229 μV K^{-1}), and average ΔT and root-mean-square temperature noise of each measurement was plotted (Fig. 4.3B). The measured thermal conductance of our calorimeter was 2.51 μW K^{-1} ($G = dQ_{abs}/d\Delta T$), and consistent with the analytical estimation by Eq. 4.1 (2.48 μW K^{-1}). This thermal conductance is approximately 6 times lower than that of the state-of-the-art chip-calorimeter (16 μW K^{-1})[115]. The root-mean-square temperature noise (T_{noise}) was approximately 80 μK for 5 min, and the corresponding sensitivity of our single-

cell calorimeter was 0.6 nW ($Q_s = G \times 3T_{noise}$), considering 3:1 signal to noise ratio. This sensitivity is an order of magnitude better than that of the state-of-the-art on-chip calorimeters (5–13 nW)[115,126]. As summarized in Fig. 4.3C, our single-cell calorimeter has achieved sufficient sensitivity to measure metabolic rate of single cells such as protozoa[128-130,134] or stimulated mammalian cells[126,132,135], which could not be measured by previous calorimeters[115-127,131].

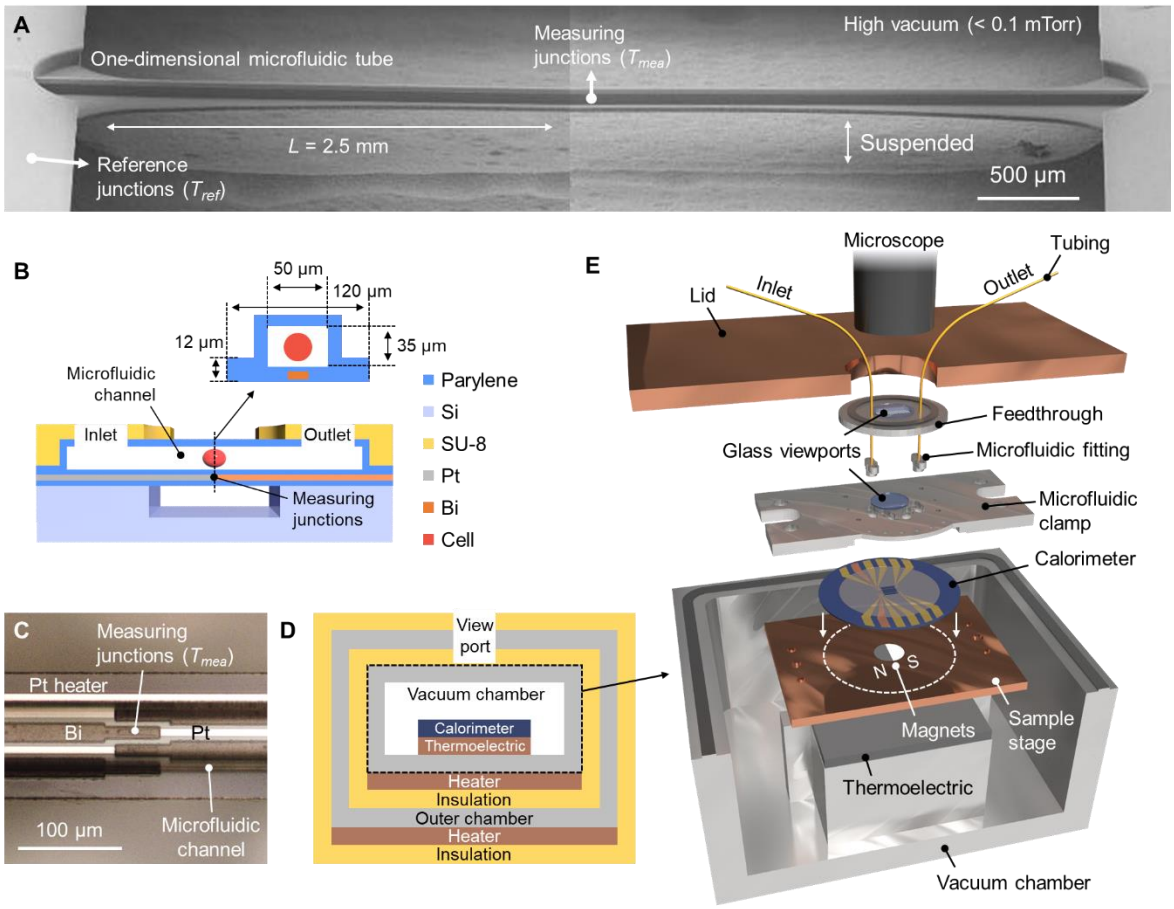


Figure. 4.1 Design of the single-cell calorimeter and measurement platform. (**A**) SEM image of the calorimeter with a 5-mm long one-dimensional suspended microfluidic tube. The suspended tube is surrounded by vacuum environment to eliminate convection heat loss. (**B**) Cross-sectional schematic of the calorimeter. A parylene tube with inner size of 35×50 μm^2 embeds a Bi-Pt thermopile as a temperature sensor. (**C**) Photograph of the middle of the suspended tube, including measuring junctions of the Bi-Pt thermopile and a Pt heater. (**D**) Schematic of thermal insulation layers of the measurement platform with three temperature-controlled layers (an outer chamber, vacuum chamber, and sample stage). (**E**) Illustration of components in the vacuum chamber. The sample stage, where the calorimeter (2-inches wafer) is placed on, provide high-stability of the temperature by thermoelectric controller. The custom-made microfluidic clamp covers the calorimeter to provide insulation against thermal radiation and fluid connection between microfluidic channels and external tubes. Vacuum-tight feedthrough and fittings ensure leakage-free fluid control. Glass viewports on the lid and microfluidic clamp enables to monitor the calorimeter during measurement.

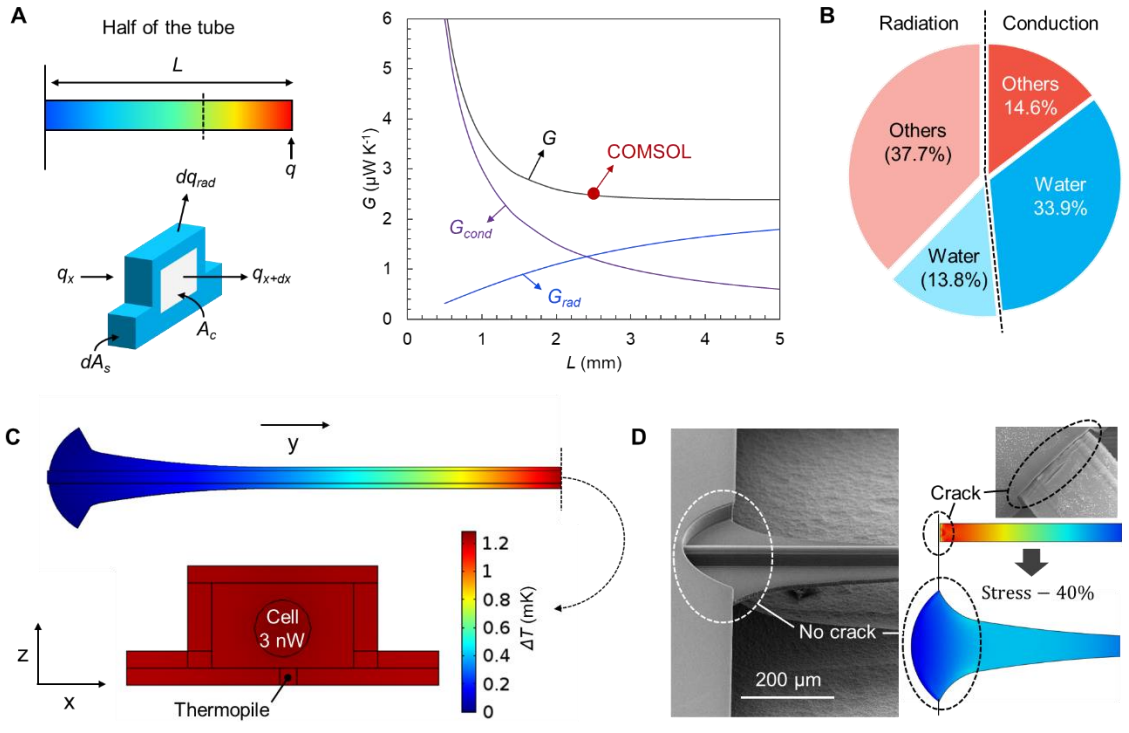


Figure. 4.2 Thermal and mechanical modeling of the calorimeter for design optimization. (**A**) Estimation of overall thermal conductance (G) of the calorimeter. The fin equation Eq. 4.1 was used for the design optimization. G saturated to 2.48 μW K^{-1} at 2.5 mm of the half tube length (L). COMSOL model reflecting the actual device geometry with a widened edge design also estimated similar overall thermal conductance (G = 2.51 μW K^{-1}) at L = 2.5 mm. (**B**) Components that cause parasitic heat loss in the calorimeter. Radiation and conduction through water account for about a half of the total heat loss. (**C**) The COMSOL model of the calorimeter. The simulation result shows that the temperature uniformity (the minimum temperature divided by the maximum temperature) within the cross-section of the suspended tube is more than 98%. This uniformity ensures that the temperature measured by the measuring junctions of Bi-Pt thermopile represents a cell temperature regardless of x- and z-axis position of the cell. (**D**) Mechanical modeling to optimize interconnection design between the suspended and unsuspended parts. The widened edge design reduced the mechanical stress of the interconnection by 40%.

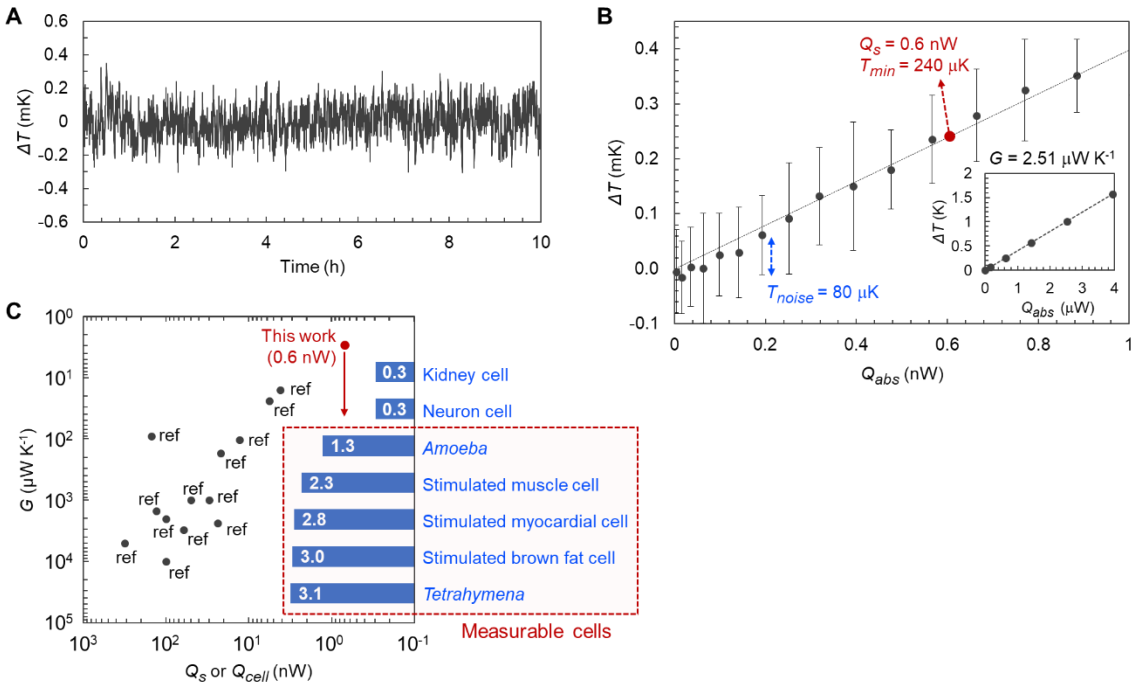


Figure. 4.3 Baseline stability and sensitivity of the calorimeter. (**A**) Baseline stability for 10 h. (**B**) Response of the calorimeter to Joule heating by the Pt heater. Average ΔT and root-mean-square temperature noise for 5 min was plotted as a function of absorbed power by measuring junctions of the thermopile (Q_{abs}). The root-mean-square temperature noise (T_{noise}) was 80 μK, and thermal conductance of the calorimeter ($G = dQ_{abs}/d\Delta T$) was 2.51 μW K^{-1}. Corresponding calorimeter sensitivity was 0.6 nW, considering 3:1 signal to noise ratio. (**C**) Comparison of previous calorimeters and the single-cell calorimeter in terms of thermal conductance and sensitivity (Q_s).

4.3 Single-cell Trapping and Nutrient Supply

As a demonstration of our calorimeter and measurement platform, we measured metabolic heat generation from single *Tetrahymena thermophila* SB210. *Tetrahymena* is widely used as a model cell to study mammalian cells because it has high homology to mammalian cells not only responding to mammalian hormones but synthesizing the similar molecules (e.g. insulin)[136-141]. Therefore, their metabolism has been studied by monitoring their oxygen consumption[142-145], metabolic heat[128-130] or size of mitochondria[146] but none of the existing measurement platforms demonstrated single-cell metabolic rate analysis. Using our high-sensitivity single-cell calorimeter, we measured a few nanowatts of single *Tetrahymena* metabolic rate for the first time.

During the demonstration, *Tetrahymena* was trapped in the calorimeter for accurate measurement. Notably, *Tetrahymena* is difficult to be trapped because they move to find nutrients using cilia. To trap *Tetrahymena*, we applied the magnetic cell trapping system as schematically shown in Fig. 4.4A. As previously shown[147-149], *Tetrahymena* can take up iron oxide nanoparticles, and their movement can then be controlled by an external magnetic field. The ingested iron oxide nanoparticles were stored in cytoplasm; Fig. 4.4C clearly show the existence of iron oxide nanoparticles in *Tetrahymena* while the *Tetrahymena* without the particles have clean cytoplasm (Fig. 4.4B). It is worth noting that the iron oxide nanoparticles are not known to impair any cellular activity[149,150]. With an external magnetic field, the ingested iron oxide nanoparticles produce induced magnetic dipole and are aligned with the direction of magnetic force as shown in Fig. 4.4D. The *Tetrahymena* with the particles can be attracted and eventually trapped in an external magnetic field. Also, the induced magnetic

dipole in *Tetrahymena* attracts adjacent nanoparticles, and the particles restrict the movement of *Tetrahymena*.

We used two permanent magnets embedded in the sample stage to generate a magnetic field for cell trapping (Fig. 4.1E); the first magnet was placed the south pole upwards, and the second magnet placed north pole upwards next to the first magnet. The iron oxide nanoparticles were mixed with culture media, and *Tetrahymena* took up the particles before measurement. The cells containing the iron oxide nanoparticles were trapped at the interface of the two magnets where the highest magnetic field occurred. By alignment of the middle of calorimeter and the interface of two magnets (Fig. 4.1E and 4.4A), we were able to place and trap *Tetrahymena* on the measuring junctions of the thermopile.

As *Tetrahymena* was trapped, nutrients and oxygen had to be supplied to maintain their normal metabolism. Notably, oxygen is limited in the microfluidic channel because of its small volume and cross-sectional area to contain and diffuse sufficient amount of oxygen for *Tetrahymena*. The oxygen consumption of *Tetrahymena* is known to be 0.1–1.0 nLO_2 $cell^{-1}$ h^{-1} [142]; however, our analysis concluded that the amount of oxygen in the channel is not sufficient for a single *Tetrahymena* (Fig. 4.5). Furthermore, previous studies showed that the starved protozoa represent smaller metabolic rate compared to that of the normal protozoa[128,134,142]. To supply sufficient nutrient and oxygen, we applied 0.1 mm s^{-1} flow of the growth medium to trapped *Tetrahymena*. The oxygen supply by the flow is estimated to be approximately 3.4 nLO_2 h^{-1}, which is a few times larger than the oxygen consumption of a single *Tetrahymena*. This low flow rate was insufficient to overcome the magnetic force trapping *Tetrahymena*, so the trapped *Tetrahymena* was not moved by the flow during the measurement. In addition, the flow did not have a major influence on the calorimeter

sensitivity. We obtained the thermal conductance of the calorimeter with the flow using the same method as described in Fig. 4.3B. The thermal conductance with the flow was only increased by ~4% (from 2.51 μW K^{-1} to 2.62 μW K^{-1}) compared to the no flow condition (Fig. 4.6A).

The procedure and representative result of single-cell metabolic rate measurement are displayed in Fig. 4.4E and F, respectively. First, a single *Tetrahymena* was injected and trapped on the measuring junctions by introduction of a magnetic field. Then, the thermopile recorded the temperature signal with the cell (T_{cell}) while 0.1 mm s^{-1} flow of growth medium supplied sufficient amount of nutrient and oxygen. The uncoupling agent FCCP was dosed to the cell through the microfluidic channel when stimulated metabolic rate was required, and increased temperature signal with the stimulation (T_{FCCP}) was also recorded. After the measurement, the cell was removed from the calorimeter by a pulsed flow, which was sufficiently strong to overcome the magnetic force. Then, the temperature signal without the cell (T_{base}) was recorded as a baseline. In Fig. 4.4F, the sudden temperature change at 5th min was caused by the pulsed flow for cell removal.

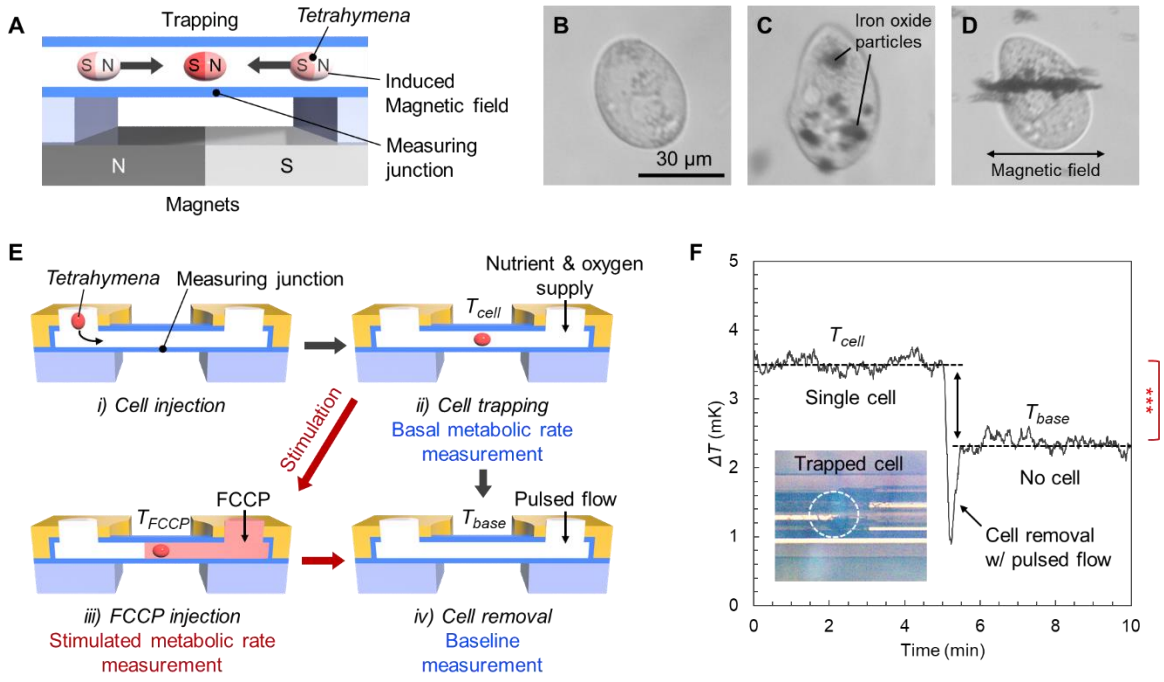


Figure 4.4 Magnetic cell trapping and single-cell measurement. (**A**) Illustration of the magnetic cell trapping. The external magnetic field generated by two magnets trapped a single cell, which internalized iron oxide nanoparticles, at the interface of the magnets, where showed highest magnetic field. (**B**) *Tetrahymena* before internalizing iron oxide nanoparticles. (**C**) *Tetrahymena* after internalizing iron oxide nanoparticles. (**D**) *Tetrahymena* with the iron oxide nanoparticles under external magnetic field. (**E**) Procedure of single-cell metabolic rate measurement: i) injection of a single *Tetrahymena* through the microfluidic channel, ii) trapping of the cell in the middle of the suspended tube by the magnetic field and measurement of the temperature with the cell (T_{cell}), iii) FCCP injection through the microfluidic channel to stimulate cell metabolism and measurement of the temperature with the stimulation (T_{FCCP}), and iv) cell removal with a pulsed flow to measure baseline temperature (T_{base}). (**F**) Representative result of the temperature signal during single-cell measurement. The inset photograph shows *Tetrahymena* during the measurement.

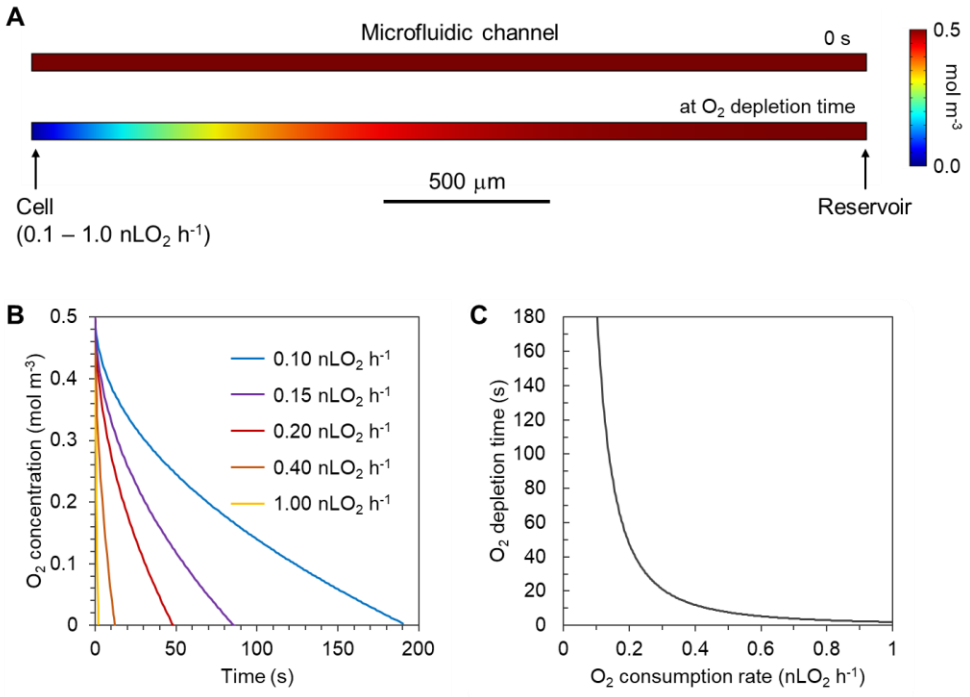


Figure 4.5 Oxygen consumption of *Tetrahymena* in microfluidic channel without flow. (**A**) COMSOL model of the oxygen consumption and diffusion, where oxygen solubility in water is 8 mg L^{-1}, oxygen consumption of *Tetrahymena* is 0.1–1.0 nLO_2 h^{-1} and oxygen diffusion rate in water is 2×10^{-5} cm^2 s^{-1}. (**B**) Oxygen concentration near *Tetrahymena* as a function of time. (**C**) Oxygen depletion time, when oxygen concentration reaches zero, as a function of oxygen consumption rate of *Tetrahymena*.

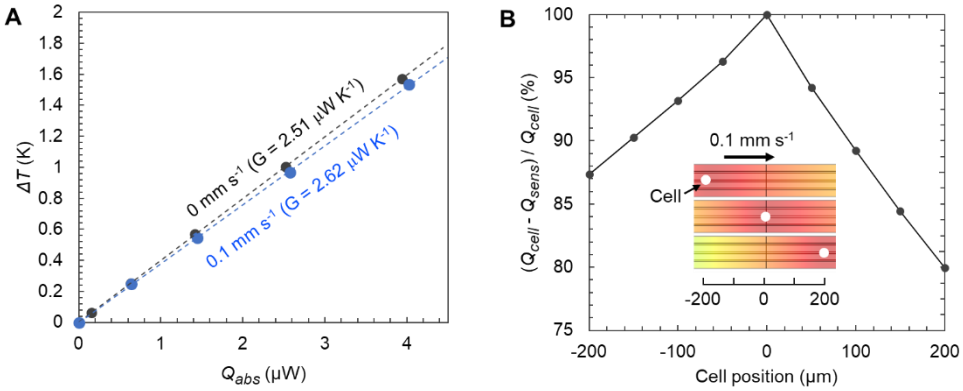


Figure 4.6 The influence of fluid flow and cell position on the calorimeter sensitivity. (**A**) Thermal conductance of the calorimeter with 0.1 mm s^{-1} of growth medium flow. (**B**) Estimation of heat signal change depending on cell position. COMSOL model was used for the estimation. The result suggests that the measured heat signal by the calorimeter can be 20% lower than actual metabolic heat from a single cell when the cell is located 200 μm apart from the measuring junctions.

4.4 Single-cell Metabolic Rate Measurement Results

We successfully measured metabolic rate of single cells. The temperature signal of thermopile when a cell trapped in the calorimeter (T_{cell}) was higher than the baseline temperature after removing the cell (T_{base}). This temperature difference ($T_{cell} - T_{base}$) indicates heat production by cellular metabolic activity of a single *Tetrahymena* and can be converted to metabolic rate ($Q_{cell} = G \times (T_{cell} - T_{base})$). As displayed in the inset graph of Fig. 4.7A, the average basal metabolic rate of *Tetrahymena* was 1.9±0.7 nW cell^{-1}, which is consistent with published values, ranging from 1 nW to 6 nW cell^{-1} [128-130]. We also measured heat generation (Q) by two and three live cells and dead cells for the comparison with that by a single cell, and representative heat signals are displayed in Fig. 4.7B. The results show clear increase of the heat generation (Q) from ~2 nW (one cell) to ~6 nW (three cells) with injecting more cells and no heat generation from dead cells, which suggest that the heat signals resulted from cell metabolism.

This basal metabolic heat is mainly produced by mitochondrial activity such as oxidative phosphorylation, generating proton gradient across the inner membrane of mitochondria, and synthesis of ATP using the proton gradient[5]. Therefore, mitochondria content in cells largely affect the basal metabolic heat generation[130]. As this mitochondria content increases as growth of cytoplasm[146], the metabolic rate is estimated to be a function of cell size during their growth phases (G1 to G2 phases before division)[151]. In fact, this allometric scaling relationship between metabolic rate and body size have been largely studied in a wide range of organisms from the smallest unicellular microorganism[142] to the largest mammal[152] and known to follow three-quarter power relationship,

$$B = B_0 V^{3/4} \quad (3)$$

where, B is the basal metabolic rate, B_0 is the normalization coefficient, and V is the body size. This powerful relationship can be also applied to mitochondria, which are the basic units of metabolism, and even to molecules of the respiratory complex in the mitochondria[152].

The previous studies of cellular allometric scaling relationship have focused on the relationship between groups of cells[142,152] because conventional metabolic rate measurement system can only measure the average value of groups of cells. However, the metabolic rate change of individual cells during growth have yet to be investigated due to the lack of single-cell measurement system and was only assumed by studying synchronous cultures[130] or optical method[146]. Interestingly, during our single-cell measurement, we found that the metabolic rate of *Tetrahymena* was correlated with cell size (Fig. 4.7B), and the trend approximately followed the three-quarter allometric scaling relationship (Fig. 4.7C). As representative results shown in Fig. 4.7B, a small cell (9×10^3 μm^3) generated the metabolic heat of 0.9 nW while a large cell (35×10^3 μm^3) produced the heat of as high as 3.3 nW, showing distinct difference ($p < 0.001$) in their heat signal. This result suggests that not only between different species or groups of cells[142] but also individual cells during growth follows the three-quarter relationship as increasing cell size, which is difficult to be observed by conventional method.

Further, we stimulated the metabolism of *Tetrahymena* by the uncoupling agent FCCP. The magnetic trap enabled to inject FCCP without losing the trapped cell. For initial few minutes after trapping a single *Tetrahymena*, the heat signal from the cell showed typical basal metabolic rate as shown in Fig. 4.7D. However, as injecting FCCP into the calorimeter,

the heat generation from the cell gradually increased and eventually saturated in 1–2 min. It is worth noting that the FCCP injection did not affect the device sensitivity, as previously described (ESI† Fig. S6a), because of the low flow rate (0.1 mm s^{-1}). This stimulated heat signal was collected for ~3 min, and then the baseline was measured after removing the cell with the pulsed flow. As a result of the FCCP stimulation, the basal metabolic rate of *Tetrahymena* increased ~1.9-fold.

While the majority of metabolic heat generation coupled to ATP synthesis in a normal condition of cells[5], FCCP can uncouple respiratory chain from ATP synthesis by direct transport of protons across the inner membrane of mitochondria and eventually dissipate the proton gradient. This uncoupled respiration can maximize the mitochondrial metabolic activity, which provides useful information of cellular metabolism[8]. For instance, the large SRC (ratio of maximal, Q_{max}, and basal metabolic rate, Q_{cell}) of more than 5.0, which can be seen in post-mitotic cells such as adipocytes, myocytes or neurons, means the cells can appropriately respond to an increased ATP demand and withstand periods of stress (inset of Fig. 4.7D). In contrast, the most of proliferative cells exhibits lower SRC of less than 3.0 because of the high basal metabolism to meet the energy demands of cell division. In case of *Tetrahymena*, although one of the study reported six-fold of large oxygen consumption rate increase with FCCP treatment[143], other studies showed SRC of about 1.5–3.0[144,145]. Also, the most of proliferative unicellular as well as small multicellular organisms showed SRC of less than 3.0 as a response to FCCP; for instance, 1.4 for protozoa (e.g. *Trypanosoma cruzi*)[153], 1.5–3.0 for mammalian cells[8], 1.5–2.0 for a warm (*Caenorhabditis elegans*)[127,154]. The SRC of *Tetrahymena* measured by our calorimeter (1.9) was similar to the typical SRC of other proliferative cells. This result suggest that the *Tetrahymena* used in our demonstration were

in normal growth condition which large amount of metabolic energy already was being used for their replication.

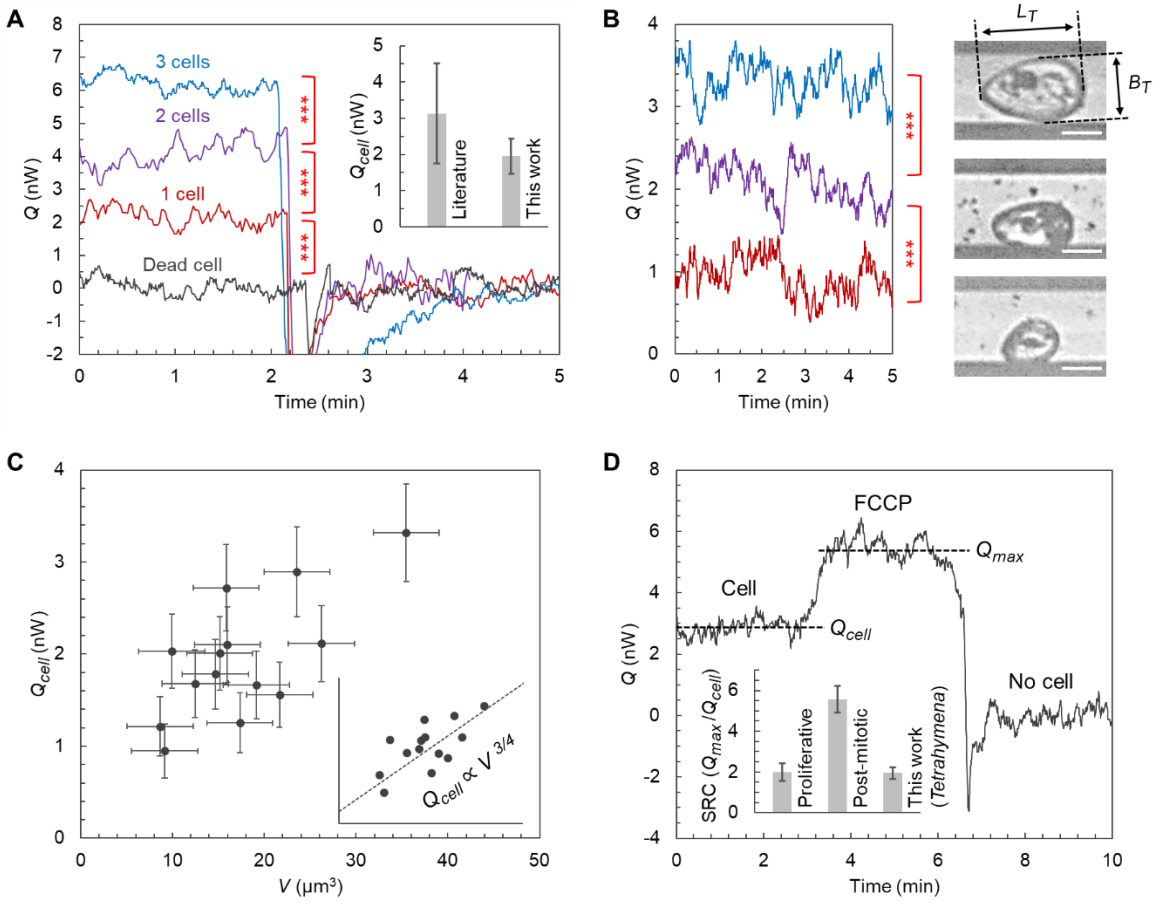


Figure 4.7 Metabolic rate measurement results. (**A**) Basal metabolic rate (Q_{cell}) of one, two, three live cells and a dead cell. Clear increase of heat signal was observed as increasing number of cells while a dead cell showed no heat signal (***$p < 0.001$). The inset graph shows the comparison of *Tetrahymena* metabolic rate from literature (3.1±1.4 nW)[128-130] and this work (1.9±0.7 nW). (**B**) Metabolic rate of single *Tetrahymena* with various cell size. The large size cell (35×10^3 μm^3), the medium size cell (16×10^3 μm^3), and the small size cell (9×10^3 μm^3) showed metabolic rate of 3.3 nW, 2.1 nW, and 0.9 nW, respectively (***$p < 0.001$). (**C**) Summary of single-cell metabolic rate as a function of cell size (V). The inset shows logarithmic scale of the summary graph. The dotted line in the inset represents the three-quarter power allometric scaling relationship ($Q_{cell} \propto V^{3/4}$). (**D**) Spare respiratory capacity (SRC, ratio of maximal metabolic rate, Q_{max}, and basal metabolic rate) measurement by stimulation of cell metabolism by the mitochondrial uncoupling agent FCCP. The cell metabolic rate was increased with dosing FCCP to the cell at 3th min. The inset shows SRC of the *Tetrahymena* used in this study (1.9), general proliferating cells (< 3.0)[8,127,144,145,153,154] and post-mitotic cells (> 5.0)[8].

4.5 Conclusion

In summary, we developed high-sensitivity chip-calorimeter and demonstrated, for the first time, calorimetric measurement of heat production by single cells. Our innovative design with a one-dimensional suspended microfluidic tube enabled to significantly reduce calorimeter thermal conductance to as low as 2.51 $\mu W\ K^{-1}$ and achieve 0.6 nW of high sensitivity sufficient for single cell metabolic rate measurement. Our demonstration of basal metabolic heat measurement of single *Tetrahymena* clarified the link between metabolic rate and cell size of individual single cells, which follows an allometric scaling relationship with the exponent of 0.6. Finally, we stimulated the metabolism by dosing the mitochondrial uncoupling agent FCCP through the microfluidic channel and analyzed SRC of *Tetrahymena*. These various demonstrations of single-cell metabolic rate measurement suggest that our novel single-cell calorimeter would lend insight into the extent and biological drivers of cellular heterogeneity.

4.6 Future Work: Investigation of Brown Adipocytes

Adipose tissues can store nutrient and generate heat. They have played important role for human survival in limited food supplies and cold ambient temperature. Now, understand of adipose tissues become a more important issue as they cause obesity, which is connected to lots of metabolic diseases. Since adipose tissues store excessive energy in the form of lipid, the imbalance between energy supply and consumption results obesity. Therefore, many studies tried to find a way to increase the energy consumption by adipocytes to reduce lipid. Adipose tissues are known to have two types, white adipose tissue (WAT) and brown adipose tissue (BAT), with different functions. WAT, which causes obesity, has one large lipid droplet to store vast amount of nutrients while BAT has multiple lipid droplets and can generate heat by consumption of the lipid. Since BAT is possible to function as a natural anti-obesity and treat obesity-related metabolic diseases, it is important to understand the differenctiation and conversion process of WAT and BAT.

Recently, the third type of adipocyte, which called beige adipocyte, was discovered[155]. The beige adipocyte represents the gene expression of uncoupling protein 1 (UCP1), which is a unique biomarker of BAT[156]; therefore this adipocyte is known to have thermogenic function as well. The beige adipocyte arises through the transdifferentiation of existing WAT or differentiation from pre-adipocytes, and notably the transdifferentiation called “browning” process meaning that conversion of WAT to beige adipocyte with brown-like function. Extensive studies revealed that the browning process is caused by cold exposure[157] or β3-adrenergic activators[158]. However, the mechanism of the browning process and the appearance of brown-like function in beige adipocytes have not largely understanded yet. For

instance, there are unanimous view of the mechanism of browning prcess[159,160] and actual thermogenic function of beige adipocyte[161].

While the thermogenic function of BAT is significantly related to UCP1 gene expression[162], some studies showed that the induction of UCP1 gene expression during the browning process may not directly represent the improvement of thermogentic potential in beige adipocytes[161,163]. The studies suggested that if UCP1 gene expression is used to measure the thermogenic effect, it can be over-estimated. As an evidence, the respiration rate measurement of WAT and beige adipocyte by indirect calorimetry showed no significant difference while UCP1 gene expression represented 150-fold induction after the browning process[162]. The extremely low UCP1 gene expression in WAT, which cause no much absolute difference even with 150-fold induction[110], is one possible reason of the discrepancy between the induction of UCP1 gene expression and actual respiration rate increase. Further investigation is required whether the induced UCP1 is sufficient for mitochondria in beige adipocyte and how they are activated. Therefore, intensive calorimetric analysis is necessary to directly measure thermogenic function of beige adipocyte along with gene expression analysis.

On the other hand, lineage-tracing of individual cells is also important to monitor the transdifferentiation or *de novo* differentiation in adipose tissues. In addition, single-cell level analysis is required to investigate the cellular origin, molecular identity, and mechanism of browning process and thermogenesis because of the heterogeneity of adipocytes in adipose tissue depots[164]. Therefore, many studies used the lineage-tracing by labeling cells with permanent fluorescence[159,165] or single-cell level gene and molecular analysis[164]. However, the current lineage-tracing and single-cell analysis suffer from lack of real-time non-

destructive method, only providing gene expression or morphological information, which are not sufficient to show actual thermogenic effect of adipocytes.

Therefore, there is urgent need of alternative method to investigate adipocytes and their browning process. Our single-cell calorimeter can be one of the unique tools for the purpose as the calorimeter can grow a single cell in its microfluidic channel and monitor the heat generation during the transdifferentiation or *de novo* differentiation of adipocytes. As shown in our demonstration with *Tetrahymena*, the calorimeter can supply neutrient or stimuli during cell culture and measure heat signal with a few hundred picowatts resolution, which is sufficient to measure activated adipocyte thermogenesis (a few nanowatts). By analysis of adipocytes with controlled environment and stimuli using the single-cell calorimeter, the systematical investigation of browning or whitening processes is possible, which may open up the new possibility to cure obesity and improve human health.

Chapter 4, in full, is currently being prepared for submission, Sahngki Hong, Edward Dechaumphai, Courtney Green, Ratneshwar Lal, Christian Metallo and Renkun Chen. The dissertation author was the primary investigator and the first author of this paper.

Chapter 5

Conclusion

This dissertation presented the investigation of metabolic heat production and thermal management in organisms using novel thermoelectric and calorimetric devices. The general overview of heat generation/transfer in organisms and thermoregulation/climate-control for thermal comfort were introduced in Chapter 1. In a subsequent chapter (Chapter 2), the wearable TED for personal thermoregulation was developed by exploiting double layers of elastomer heat spreading layers embedding an air gap insulation layer and high-ZT bulk TE pillars. We demonstrated more than 10 °C of high cooling effect without harnessing bulk heat sinks using our wearable TED. The TED was sufficiently flexible to be embedded in a garment and exhibited high thermoregulation effect, which maintains human in a thermally comfortable condition in the wide range of ambient temperature (> 14 °C). The power consumption of the personal thermoregulation by our TED was a few orders of magnitude lower than the per capita energy consumption is US (~1.5 kW). In Chapter 3, we applied the wearable TED for personal thermal camouflage. The device delivered precise and sufficient temperature control for the thermal camouflage effect and was capable of matching the temperature of human body with background temperature ranging from 16 to 38 °C.

The Chapter 4 focuses on the development of single-cell calorimeter and measurement of metabolic heat production of individual unicellular organisms. We demonstrated the finest power resolution of microfluidics-based calorimeter of 0.6 nW using one-dimensional suspended microfluidic tube in vacuum environment. Metabolic rate of

single *Tetrahymena* was measured with assistance of magnetic cell trapping system. The comparison of the measured metabolic rate by our calorimeter (direct calorimetry) and other indirect calorimetry suggested the possible existence of anaerobic metabolism in proliferating *Tetrahymena* under aerobic conditions. The metabolic rate of individual *Tetrahymena* was obviously correlated with cell size, following allometric scaling relationship with the exponent of 0.6. This trand suggests that the anaerobic metabolic rate in unicellular organisms increases as cell growth. Our single-cell calorimetry system was able to inject stimuli into the reaction chamber and monitor the change of heat signal by a single cell. Maximal metabolic rate of *Tetrahymena* stimulated by injection of the FCCP uncoupling agent showed that the *Tetrahymena* in the calorimeter has SRC of 1.9, which is similar to SRC of other proliferating cells.

In conclusion, the works presented in this dissertation demonstrated the development of novel thermoelectric and calorimetric devices with the finest performance and resolution, which unlocked the applications to personal thermoregulation and single-cell heat production analysis. The technologies we have developed may pave the way for improvement of human thermal comfort and broaden the knowledge of heat production in living organisms.

Reference

1 Benzinger, T. Heat and temperature fundamentals of medical physiology. *New York: Hutchinson & Ross* (1980).

2 Gnaiger, E. & Kemp, R. B. Anaerobic metabolism in aerobic mammalian cells: information from the ratio of calorimetric heat flux and respirometric oxygen flux. *Biochimica et Biophysica Acta (BBA)-Bioenergetics* **1016**, 328-332 (1990).

3 Maskow, T., Kemp, R., Buchholz, F., Schubert, T., Kiesel, B. & Harms, H. What heat is telling us about microbial conversions in nature and technology: from chip-to megacalorimetry. *Microb. Biotechnol.* **3**, 269-284 (2010).

4 Maskow, T., Schubert, T., Wolf, A., Buchholz, F., Regestein, L., Buechs, J., Mertens, F., Harms, H. & Lerchner, J. Potentials and limitations of miniaturized calorimeters for bioprocess monitoring. *Appl. Microbiol. Biotechnol.* **92**, 55 (2011).

5 Rolfe, D. & Brown, G. C. Cellular energy utilization and molecular origin of standard metabolic rate in mammals. *Physiol. Rev.* **77**, 731-758 (1997).

6 Herman, I. P. *Physics of the human body*. (Springer, Germany, 2016).

7 Kelso, J. D. *2011 Buildings Energy Data Book*. (U.S. Department of Energy, Washington, 2012).

8 Divakaruni, A. S., Paradyse, A., Ferrick, D. A., Murphy, A. N. & Jastroch, M. in *Methods Enzymol.* Vol. 547 309-354 (Elsevier, 2014).

9 Vander Heiden, M. G., Cantley, L. C. & Thompson, C. B. Understanding the Warburg effect: the metabolic requirements of cell proliferation. *science* **324**, 1029-1033 (2009).

10 Blaxter, K. *Energy metabolism in animals and man*. (CUP Archive, 1989).

11 Cannon, B. & Nedergaard, J. Brown adipose tissue: function and physiological significance. *Physiological reviews* **84**, 277-359 (2004).

12 Dutta, P. & Horn, P. Low-frequency fluctuations in solids: 1 f noise. *Rev. Mod. Phys.* **53**, 497 (1981).

13 Freitas, R. A. *Nanomedicine, volume I: basic capabilities*. (Landes Bioscience Georgetown, TX, 1999).

14 Fanger, P. O. *Thermal comfort. Analysis and applications in environmental engineering*. (Danish Technical Press, Copenhagen, Denmark, 1970).

15 Gagge, A. P., Stolwijk, J. & Hardy, J. Comfort and thermal sensations and associated physiological responses at various ambient temperatures. *Environ. Res.* **1**, 1-20 (1967).

16 de Dear, R. J. & Brager, G. S. Thermal comfort in naturally ventilated buildings: revisions to ASHRAE Standard 55. *Energ. Buildings* **34**, 549-561 (2002).

17 de Dear, R. J., Brager, G. S., Reardon, J. & Nicol, F. Developing an adaptive model of thermal comfort and preference. *ASHRAE transactions* **104**, 145-167 (1998).

18 Hsu, P. C., Song, A. Y., Catrysse, P. B., Liu, C., Peng, Y. C., Xie, J., Fan, S. H. & Cui, Y. Radiative human body cooling by nanoporous polyethylene textile. *Science* **353**, 1019-1023 (2016).

19 Hsu, P. C., Liu, C., Song, A. Y., Zhang, Z., Peng, Y., Xie, J., Liu, K., Wu, C. L., Catrysse, P. B., Cai, L., Zhai, S., Majumdar, A., Fan, S. H. & Cui, Y. A dual-mode textile for human body radiative heating and cooling. *Sci. Adv.* **3**, e1700895 (2017).

20 Zhai, Y., Ma, Y., David, S. N., Zhao, D., Lou, R., Tan, G., Yang, R. & Yin, X. Scalable-manufactured randomized glass-polymer hybrid metamaterial for daytime radiative cooling. *Science* **355**, 1062-1066 (2017).

21 Ma, R. J., Zhang, Z. Y., Tong, K. W., Huber, D., Kornbluh, R., Ju, Y. S. & Pei, Q. B. Highly efficient electrocaloric cooling with electrostatic actuation. *Science* **357**, 1130-+ (2017).

22 Chu, S. & Majumdar, A. Opportunities and challenges for a sustainable energy future. *Nature* **488**, 294 (2012).

23 Farrington, R. & Rugh, J. Impact of Vehicle Air-Conditioning on Fuel Economy, Tailpipe Emissions, and Electric Vehicle Range. NREL/CP-540-28960, http://www.nrel.gov/docs/fy00osti/28960.pdf (2000).

24 Goldstein, E. A., Raman, A. P. & Fan, S. H. Sub-ambient non-evaporative fluid cooling with the sky. *Nat. Energy* **2**, 17143 (2017).

25 Kenney, W. L., Wilmore, J. & Costill, D. *Physiology of sport and exercise 6th edition*. (Human kinetics, 2015).

26 Mokhtari Yazdi, M. & Sheikhzadeh, M. Personal cooling garments: a review. *J. Text. I.* **105**, 1231-1250 (2014).

27 Hsu, P. C., Liu, X. G., Liu, C., Xie, X., Lee, H. R., Welch, A. J., Zhao, T. & Cui, Y. Personal Thermal Management by Metallic Nanowire-Coated Textile. *Nano Lett.* **15**, 365-371 (2015).

28 Lu, S. G. & Zhang, Q. Electrocaloric materials for solid-state refrigeration. *Adv. Mater.* **21**, 1983-1987 (2009).

29 Moya, X., Kar-Narayan, S. & Mathur, N. D. Caloric materials near ferroic phase transitions. *Nat. Mater.* **13**, 439-450 (2014).

30 He, J. & Tritt, T. M. Advances in thermoelectric materials research: Looking back and moving forward. *Science* **357**, 6358 (2017).

31 Ma, R. J., Zhang, Z. Y., Tong, K. W., Huber, D., Kornbluh, R., Ju, Y. S. & Pei, Q. B. Highly efficient electrocaloric cooling with electrostatic actuation. *Science* **357**, 1130-1134 (2017).

32 Bahk, J.-H., Fang, H., Yazawa, K. & Shakouri, A. Flexible thermoelectric materials and device optimization for wearable energy harvesting. *J. Mater. Chem. C* **3**, 10362-10374 (2015).

33 Suarez, F., Nozariasbmarz, A., Vashaee, D. & Öztürk, M. C. Designing thermoelectric generators for self-powered wearable electronics. *Energy Environ. Sci.* **9**, 2099-2113 (2016).

34 Kim, S. J., Lee, H. E., Choi, H., Kim, Y., We, J. H., Shin, J. S., Lee, K. J. & Cho, B. J. High-Performance Flexible Thermoelectric Power Generator Using Laser Multiscanning Lift-Off Process. *ACS Nano* **10**, 10851-10857 (2016).

35 Suarez, F., Parekh, D. P., Ladd, C., Vashaee, D., Dickey, M. D. & Öztürk, M. C. Flexible thermoelectric generator using bulk legs and liquid metal interconnects for wearable electronics. *Appl. Energy* **202**, 736-745 (2017).

36 Jeong, S. H., Cruz, F. J., Chen, S., Gravier, L., Liu, J., Wu, Z., Hjort, K., Zhang, S.-L. & Zhang, Z.-B. Stretchable thermoelectric generators metallized with liquid alloy. *ACS Appl. Mater. Interfaces* **9**, 15791-15797 (2017).

37 Liu, H., Wang, Y., Mei, D., Shi, Y. & Chen, Z. Design of a wearable thermoelectric generator for harvesting human body energy. *Wearable Sensors and Robots*, 55-66 (2017).

38 Kim, C. S., Lee, G. S., Choi, H., Kim, Y. J., Yang, H. M., Lim, S. H., Lee, S.-G. & Cho, B. J. Structural design of a flexible thermoelectric power generator for wearable applications. *Appl. Energy* **214**, 131-138 (2018).

39 Wang, Y., Shi, Y., Mei, D. & Chen, Z. Wearable thermoelectric generator to harvest body heat for powering a miniaturized accelerometer. *Appl. Energy* **215**, 690-698 (2018).

40 Kim, S. J., We, J. H. & Cho, B. J. A wearable thermoelectric generator fabricated on a glass fabric. *Energy Environ. Sci.* **7**, 1959-1965 (2014).

41 Kim, M. K., Kim, M. S., Lee, S., Kim, C. & Kim, Y. J. Wearable thermoelectric generator for harvesting human body heat energy. *Smart Mater. Struct.* **23** (2014).

42 Lu, Z., Zhang, H., Mao, C. & Li, C. M. Silk fabric-based wearable thermoelectric generator for energy harvesting from the human body. *Appl. Energy* **164**, 57-63 (2016).

43 Jo, S., Kim, M., Kim, M. & Kim, Y. Flexible thermoelectric generator for human body heat energy harvesting. *Electron. Lett.* **48**, 1015-1017 (2012).

44 Eom, Y., Wijethunge, D., Park, H., Park, S. H. & Kim, W. Flexible thermoelectric power generation system based on rigid inorganic bulk materials. *Appl. Energy* **206**, 649-656 (2017).

45 Kim, C. S., Yang, H. M., Lee, J., Lee, G. S., Choi, H., Kim, Y. J., Lim, S. H., Cho, S. H. & Cho, B. J. Self-Powered Wearable Electrocardiography Using a Wearable Thermoelectric Power Generator. *ACS Energy Lett.* **3**, 501-507 (2018).

46 Park, H., Kim, D., Eom, Y., Wijethunge, D., Hwang, J., Kim, H. & Kim, W. Mat-like flexible thermoelectric system based on rigid inorganic bulk materials. *J. Phys. D: Appl. Phys.* **50**, 494006 (2017).

47 Park, H., Lee, D., Kim, D., Cho, H., Eom, Y., Hwang, J., Kim, H., Kim, J., Han, S. & Kim, W. High power output from body heat harvesting based on flexible thermoelectric system with low thermal contact resistance. *J. Phys. D: Appl. Phys.* **51**, 365501 (2018).

48 Shin, S., Kumar, R., Roh, J. W., Ko, D.-S., Kim, H.-S., Kim, S. I., Yin, L., Schlossberg, S. M., Cui, S. & You, J.-M. High-Performance Screen-Printed Thermoelectric Films on Fabrics. *Sci. Rep.* **7**, 7317 (2017).

49 Nan, K., Kang, S. D., Li, K., Yu, K. J., Zhu, F., Wang, J., Dunn, A. C., Zhou, C., Xie, Z. & Agne, M. T. Compliant and stretchable thermoelectric coils for energy harvesting in miniature flexible devices. *Sci. Adv.* **4**, eaau5849 (2018).

50 We, J. H., Kim, S. J. & Cho, B. J. Hybrid composite of screen-printed inorganic thermoelectric film and organic conducting polymer for flexible thermoelectric power generator. *Energy* **73**, 506-512 (2014).

51 Oh, J. Y., Lee, J. H., Han, S. W., Chae, S. S., Bae, E. J., Kang, Y. H., Choi, W. J., Cho, S. Y., Lee, J.-O. & Baik, H. K. Chemically exfoliated transition metal dichalcogenide nanosheet-based wearable thermoelectric generators. *Energy Environ. Sci.* **9**, 1696-1705 (2016).

52 Wu, Q. & Hu, J. A novel design for a wearable thermoelectric generator based on 3D fabric structure. *Smart Mater. Struct.* **26**, 045037 (2017).

53 Kim, G. H., Shao, L., Zhang, K. & Pipe, K. P. Engineered doping of organic semiconductors for enhanced thermoelectric efficiency. *Nat. Mater.* **12**, 719-723 (2013).

54 de Dear, R. J., Arens, E., Hui, Z. & Oguro, M. Convective and radiative heat transfer coefficients for individual human body segments. *Int. J. Biometeorol.* **40**, 141-156 (1997).

55 Baldwin, P. E. & Maynard, A. D. A survey of wind speeds in indoor workplaces. *Ann. Occup. Hyg.* **42**, 303-313 (1998).

56 Yao, Y., Lian, Z. W., Liu, W. W. & Shen, Q. Experimental study on skin temperature and thermal comfort of the human body in a recumbent posture under uniform thermal environments. *Indoor Built Environ.* **16**, 505-518 (2007).

57 Veselý, M. & Zeiler, W. Personalized conditioning and its impact on thermal comfort and energy performance–A review. *Renewable Sustainable Energy Rev.* **34**, 401-408 (2014).

58 Bandodkar, A. J., You, J. M., Kim, N. H., Gu, Y., Kumar, R., Mohan, A. V., Kurniawan, J., Imani, S., Nakagawa, T., Parish, B., Parthasarathy, M., Mercier, P. P., Xu, S. & Wang, J. Soft, stretchable, high power density electronic skin-based biofuel cells for scavenging energy from human sweat. *Energy Environ. Sci.* **10**, 1581-1589 (2017).

59 Van Noorden, R. A better battery. *Nature* **507**, 26 (2014).

60 Hanlon, R. Cephalopod dynamic camouflage. *Current Biology* **17**, R400-R404 (2007).

61 Cott, H. B. *Adaptive coloration in animals*. (Methuen; London, 1940).

62 Stuart-Fox, D. & Moussalli, A. Camouflage, communication and thermoregulation: lessons from colour changing organisms. *Philosophical Transactions of the Royal Society of London B: Biological Sciences* **364**, 463-470 (2009).

63 Ramachandran, V., Tyler, C., Gregory, R., Rogers-Ramachandran, D., Duensing, S., Pillsbury, C. & Ramachandran, C. Rapid adaptive camouflage in tropical flounders. *Nature* **379**, 815-818 (1996).

64 Morin, S. A., Shepherd, R. F., Kwok, S. W., Stokes, A. A., Nemiroski, A. & Whitesides, G. M. Camouflage and display for soft machines. *Science* **337**, 828-832 (2012).

65 Yu, C., Li, Y., Zhang, X., Huang, X., Malyarchuk, V., Wang, S., Shi, Y., Gao, L., Su, Y. & Zhang, Y. Adaptive optoelectronic camouflage systems with designs inspired by cephalopod skins. *Proceedings of the National Academy of Sciences* **111**, 12998-13003 (2014).

66 Heikenfeld, J., Zhou, K., Kreit, E., Raj, B., Yang, S., Sun, B., Milarcik, A., Clapp, L. & Schwartz, R. Electrofluidic displays using Young–Laplace transposition of brilliant pigment dispersions. *Nature Photonics* **3**, 292 (2009).

67 Rogalski, A. Infrared detectors: status and trends. *Progress in quantum electronics* **27**, 59-210 (2003).

68 Rogalski, A. *Infrared detectors*. (CRC press, 2010).

69 Dereniak, E. L. & Boreman, G. D. *Infrared detectors and systems*. (Wiley New York, 1996).

70 Rogalski, A. History of infrared detectors. *Opto-Electronics Review* **20**, 279-308 (2012).

71 Xiao, L., Ma, H., Liu, J., Zhao, W., Jia, Y., Zhao, Q., Liu, K., Wu, Y., Wei, Y. & Fan, S. Fast adaptive thermal camouflage based on flexible VO2/graphene/CNT thin films. *Nano letters* **15**, 8365-8370 (2015).

72 Ji, H., Liu, D., Cheng, H., Zhang, C., Yang, L. & Ren, D. Infrared thermochromic properties of monoclinic VO 2 nanopowders using a malic acid-assisted hydrothermal method for adaptive camouflage. *RSC Advances* **7**, 5189-5194 (2017).

73 Qu, Y., Li, Q., Cai, L., Pan, M., Ghosh, P., Du, K. & Qiu, M. Thermal camouflage based on the phase-changing material GST. *Light: Science & Applications* **7**, 26 (2018).

74 Salihoglu, O., Uzlu, H. B., Yakar, O., Aas, S., Balci, O., Kakevov, N., Balci, S., Olcum, S., Süzer, S. & Kocabas, C. Graphene Based Adaptive Thermal Camouflage. *arXiv preprint arXiv:1804.11004* (2018).

75 Xu, C., Stiubianu, G. T. & Gorodetsky, A. A. Adaptive infrared-reflecting systems inspired by cephalopods. *Science* **359**, 1495-1500 (2018).

76 Chandrasekhar, P., Zay, B. J., Birur, G. C., Rawal, S., Pierson, E. A., Kauder, L. & Swanson, T. Large, Switchable Electrochromism in the Visible Through Far-Infrared in Conducting Polymer Devices. *Advanced Functional Materials* **12**, 95-103 (2002).

77 Gupta, K., Nishkam, A. & Kasturiya, N. Camouflage in the non-visible region. *Journal of Industrial Textiles* **31**, 27-42 (2001).

78 Zhang, H. & Zhang, J. C. Near-infrared green camouflage of cotton fabrics using vat dyes. *Journal of the Textile Institute* **99**, 83-88 (2008).

79 Rubežienė, V., Padleckienė, I., Baltušnikaitė, J. & VARNAITĖ, S. Evaluation of camouflage effectiveness of printed fabrics in visible and near infrared radiation spectral ranges. *Material Sciences Medziagotyra* **14**, 361-365 (2008).

80 Milewski, S., Dulski, R., Kastek, M., Trzaskawka, P., Barela, J. & Firmanty, K. in *Electro-Optical and Infrared Systems: Technology and Applications VIII.* 81850V (International Society for Optics and Photonics).

81 Han, T., Bai, X., Gao, D., Thong, J. T., Li, B. & Qiu, C.-W. Experimental demonstration of a bilayer thermal cloak. *Physical review letters* **112**, 054302 (2014).

82 Li, Y., Bai, X., Yang, T., Luo, H. & Qiu, C.-W. Structured thermal surface for radiative camouflage. *Nature communications* **9**, 273 (2018).

83 Xu, H., Shi, X., Gao, F., Sun, H. & Zhang, B. Ultrathin three-dimensional thermal cloak. *Physical Review Letters* **112**, 054301 (2014).

84 Schittny, R., Kadic, M., Guenneau, S. & Wegener, M. Experiments on transformation thermodynamics: molding the flow of heat. *Physical review letters* **110**, 195901 (2013).

85 Han, T., Bai, X., Thong, J. T., Li, B. & Qiu, C. W. Full control and manipulation of heat signatures: Cloaking, camouflage and thermal metamaterials. *Advanced Materials* **26**, 1731-1734 (2014).

86 Takashima, T. & Masuda, K. Emissivities of quartz and Sahara dust powders in the infrared region (7–17 μ). *Remote Sensing of Environment* **23**, 51-63 (1987).

87 Viehmann, W. & Eubanks, A. G. Effects of surface contamination on the infrared emissivity and visible-light scattering of highly reflective surfaces at cryogenic temperatures. (1972).

88 Sjölund, P. Device for signature adaptation and object provided with such a device. United States patent US9360279B2 (2016).

89 Hughes, R. Personal portable blankets as an infrared shielding device for field activities. United States patent US7102814B1 (2006).

90 Ladbury, J. E. & Doyle, M. L. *Biocalorimetry 2: applications of calorimetry in the biological sciences*. (John Wiley & Sons, 2004).

91 Darnell, J. E., Lodish, H. F. & Baltimore, D. *Molecular cell biology*. (Scientific American Books New York, 1990).

92 Chance, B. & Williams, G. The respiratory chain and oxidative phosphorylation. *Adv. Enzymol. Relat. Areas Mol. Biol.* **17**, 65-134 (1956).

93 Lee, W., Lee, J. & Koh, J. Development and applications of chip calorimeters as novel biosensors. *Nanobiosens. Dis. Diagn.* **1**, 17-29 (2012).

94 Braissant, O., Wirz, D., Göpfert, B. & Daniels, A. Biomedical use of isothermal microcalorimeters. *Sensors* **10**, 9369-9383 (2010).

95 Wadsö, I. Microcalorimetric techniques for characterization of living cellular systems. Will there be any important practical applications? *Thermochim. Acta* **269**, 337-350 (1995).

96 Baldoni, D., Hermann, H., Frei, R., Trampuz, A. & Steinhuber, A. Performance of microcalorimetry for early detection of methicillin resistance in clinical isolates of Staphylococcus aureus. *J. Clin. Microbiol.* **47**, 774-776 (2009).

97 Lerchner, J., Mueller-Hagen, D., Roehr, H., Wolf, A., Mertens, F., Mueller, R., Witte, W. & Klare, I. Chip-calorimetric evaluation of the efficacy of antibiotics and bacteriophages against bacteria on a minute-timescale. *J. Therm. Anal. Calorim.* **104**, 31-36 (2011).

98 Trampuz, A., Salzmann, S., Antheaume, J. & Daniels, A. U. Microcalorimetry: a novel method for detection of microbial contamination in platelet products. *Transfusion* **47**, 1643-1650 (2007).

99 Braissant, O., Wirz, D., Göpfert, B. & Daniels, A. U. Use of isothermal microcalorimetry to monitor microbial activities. *FEMS Microbiol. Lett.* **303**, 1-8 (2010).

100 Monti, M., Brandt, L., Ikomi-Kumm, J. & Olsson, H. Microcalorimetric investigation of cell metabolism in tumour cells from patients with non-Hodgkin lymphoma (NHL). *Scand. J. Haematol.* **36**, 353-357 (1986).

101 Cantor, J. R. & Sabatini, D. M. Cancer cell metabolism: one hallmark, many faces. *Cancer discovery* (2012).

102 Karnebogen, M., Singer, D., Kallerhoff, M. & Ringert, R.-H. Microcalorimetric investigations on isolated tumorous and non-tumorous tissue samples. *Thermochim. Acta* **229**, 147-155 (1993).

103 Carlo, D. D. & Lee, L. P. Dynamic single-cell analysis for quantitative biology. *Anal. Chem.* **78**, 7918–7925 (2006).

104 Lidstrom, M. E. & Meldrum, D. R. Life-on-a-chip. *Nat. Rev. Microbiol.* **1**, 158 (2003).

105 Cohen, D., Dickerson, J. A., Whitmore, C. D., Turner, E. H., Palcic, M. M., Hindsgaul, O. & Dovichi, N. J. Chemical cytometry: fluorescence-based single-cell analysis. *Annu. Rev. Anal. Chem.* **1**, 165-190 (2008).

106 Zhang, Z., Krylov, S., Arriaga, E. A., Polakowski, R. & Dovichi, N. J. One-dimensional protein analysis of an HT29 human colon adenocarcinoma cell. *Anal. Chem.* **72**, 318-322 (2000).

107 Etzkorn, J. R., Wu, W.-C., Tian, Z., Kim, P., Jang, S.-H., Meldrum, D. R., Jen, A. K. & Parviz, B. A. Using micro-patterned sensors and cell self-assembly for measuring the oxygen consumption rate of single cells. *J. Micromech. Microeng.* **20**, 095017 (2010).

108 Gossett, D. R., Henry, T., Lee, S. A., Ying, Y., Lindgren, A. G., Yang, O. O., Rao, J., Clark, A. T. & Di Carlo, D. Hydrodynamic stretching of single cells for large population mechanical phenotyping. *Proc. Natl. Acad. Sci. U. S. A.* **109**, 7630-7635 (2012).

109 Strovas, T. J., Sauter, L. M., Guo, X. & Lidstrom, M. E. Cell-to-cell heterogeneity in growth rate and gene expression in Methylobacterium extorquens AM1. *J. Bacteriol.* **189**, 7127-7133 (2007).

110 Kuznetsov, A. V. & Margreiter, R. Heterogeneity of mitochondria and mitochondrial function within cells as another level of mitochondrial complexity. *Int. J. Mol. Sci.* **10**, 1911-1929 (2009).

111 Criddle, R., Fontana, A., Rank, D., Paige, D., Hansen, L. & Breidenbach, R. Simultaneous measurement of metabolic heat rate, CO2 production, and O2 consumption by microcalorimetry. *Anal. Biochem.* **194**, 413-417 (1991).

112 Perfetto, S. P., Chattopadhyay, P. K. & Roederer, M. Seventeen-colour flow cytometry: unravelling the immune system. *Nat. Rev. Immunol.* **4**, 648 (2004).

113 Wu, H., Wheeler, A. & Zare, R. N. Chemical cytometry on a picoliter-scale integrated microfluidic chip. *Proc. Natl. Acad. Sci. U. S. A.* **101**, 12809-12813 (2004).

114 Werdich, A. A., Lima, E. A., Ivanov, B., Ges, I., Anderson, M. E., Wikswo, J. P. & Baudenbacher, F. J. A microfluidic device to confine a single cardiac myocyte in a sub-nanoliter volume on planar microelectrodes for extracellular potential recordings. *Lab Chip* **4**, 357-362 (2004).

115 Lee, W., Fon, W., Axelrod, B. W. & Roukes, M. L. High-sensitivity microfluidic calorimeters for biological and chemical applications. *Proc. Natl. Acad. Sci. U. S. A.* **106**, 15225-15230 (2009).

116 Recht, M. I., De Bruyker, D., Bell, A. G., Wolkin, M. V., Peeters, E., Anderson, G. B., Kolatkar, A. R., Bern, M. W., Kuhn, P. & Bruce, R. H. Enthalpy array analysis of enzymatic and binding reactions. *Anal. Biochem.* **377**, 33-39 (2008).

117 Torres, F. E., Kuhn, P., De Bruyker, D., Bell, A. G., Wolkin, M. V., Peeters, E., Williamson, J. R., Anderson, G. B., Schmitz, G. P. & Recht, M. I. Enthalpy arrays. *Proc. Natl. Acad. Sci. U. S. A.* **101**, 9517-9522 (2004).

118 Wang, L., Sipe, D. M., Xu, Y. & Lin, Q. A MEMS thermal biosensor for metabolic monitoring applications. *J. Microelectromech. Syst.* **17**, 318-327 (2008).

119 Verhaegen, K., Baert, K., Simaels, J. & Van Driessche, W. A high-throughput silicon microphysiometer. *Sens. Actuators, A* **82**, 186-190 (2000).

120 Hartmann, T., Barros, N., Wolf, A., Siewert, C., Volpe, P., Schemberg, J., Grodrian, A., Kessler, E., Hänschke, F. & Mertens, F. Thermopile chip based calorimeter for the study of aggregated biological samples in segmented flow. *Sens. Actuators, B* **201**, 460-468 (2014).

121 Lerchner, J., Wolf, A., Schneider, H.-J., Mertens, F., Kessler, E., Baier, V., Funfak, A., Nietzsch, M. & Krügel, M. Nano-calorimetry of small-sized biological samples. *Thermochim. Acta* **477**, 48-53 (2008).

122 Zhang, Y. & Tadigadapa, S. Calorimetric biosensors with integrated microfluidic channels. *Biosens. Bioelectron.* **19**, 1733-1743 (2004).

123 Xu, J., Reiserer, R., Tellinghuisen, J., Wikswo, J. P. & Baudenbacher, F. J. A microfabricated nanocalorimeter: design, characterization, and chemical calibration. *Anal. Chem.* **80**, 2728-2733 (2008).

124 Chancellor, E., Wikswo, J., Baudenbacher, F., Radparvar, M. & Osterman, D. Heat conduction calorimeter for massively parallel high throughput measurements with picoliter sample volumes. *Appl. Phys. Lett.* **85**, 2408-2410 (2004).

125 Fiorino, A., Thompson, D., Yadlapalli, S., Jiang, C., Shafer, O. T., Reddy, P. & Meyhofer, E. Parallelized, real-time, metabolic-rate measurements from individual Drosophila. *Sci. Rep.* **8**, 14452 (2018).

126 Johannessen, E. A., Weaver, J. M., Bourova, L., Svoboda, P., Cobbold, P. H. & Cooper, J. M. Micromachined nanocalorimetric sensor for ultra-low-volume cell-based assays. *Anal. Chem.* **74**, 2190-2197 (2002).

127 Krenger, R., Lehnert, T. & Gijs, M. A. Dynamic microfluidic nanocalorimetry system for measuring Caenorhabditis elegans metabolic heat. *Lab Chip* **18**, 1641-1651 (2018).

128 Chen, X., Feng, W. & Yu, Y. Studies on the nongrowth metabolism of the different strains of Tetrahymena cells by isothermal microcalorimetry. *J. Therm. Anal. Calorim.* **115**, 2145-2149 (2014).

129 Chang-Li, X., Day-Ung, S., Zhau-Hua, S., Song-Sheng, Q., Yu, G. & Bing, L. Microcalorimetric studies on Tetrahymena pyriformis: part 1. Growth metabolic power and thermal equations. *Thermochim. Acta* **183**, 117-123 (1991).

130 Lloyd, D., Phillips, C. A. & Statham, M. Oscillations of respiration, adenine nucleotide levels and heat evolution in synchronous cultures of Tetrahymena pyriformis ST prepared by continuous-flow selection. *Microbiology* **106**, 19-26 (1978).

131 Inomata, N., Toda, M. & Ono, T. Highly sensitive thermometer using a vacuum-packed Si resonator in a microfluidic chip for the thermal measurement of single cells. *Lab Chip* **16**, 3597-3603 (2016).

132 Tanaka, E., Yamakawa, A., YAMAMURA, M., El, N., Nadia, E. B., ITO, K. & NAKANO, S. Regulation of heat production of brown adipocytes via typical and atypical β-adrenoceptors in the rat. *Jpn. J. Physiol.* **45**, 1043-1051 (1995).

133 Agathocleous, M. & Harris, W. A. Metabolism in physiological cell proliferation and differentiation. *Trends Cell Biol.* **23**, 484-492 (2013).

134 Nässberger, L. & Monti, M. Assessment of overall metabolism inAmoeba proteus measured by a microcalorimetric method. *Protoplasma* **123**, 135-139 (1984).

135 Hall, J. E. *Guyton and Hall textbook of medical physiology e-Book*. (Elsevier Health Sciences, 2015).

136 Kohidai, L. & Csaba, G. EVects of the mammalian vasoconstrictor peptide, endothelin-1, on Tetrahymena pyriformis GL, and the immunocytological detection of endogenous endothelin-like activity. *Comp. Biochem. Physiol. C. Pharmacol. Toxicol. Endocrinol* **111**, 311-316 (1995).

137 Köhidai, L., Vakkuri, O., Keresztesi, M., Leppäluoto, J. & Csaba, G. Melatonin in the unicellular Tetrahymena pyriformis: effects of different lighting conditions. *Cell Biochem. Funct.* **20**, 269-272 (2002).

138 Csaba, G. & Pállinger, É. Is there a hormonal network in Tetrahymena? A systematic investigation of hormonal effects on the hormone content. *Cell Biochem. Funct.* **26**, 303-308 (2008).

139 Le Roith, D., Shiloach, J., Roth, J. & Lesniak, M. A. Evolutionary origins of vertebrate hormones: substances similar to mammalian insulins are native to unicellular eukaryotes. *Proc. Natl. Acad. Sci. U. S. A.* **77**, 6184-6188 (1980).

140 LeRoith, D., Liotta, A., Roth, J., Shiloach, J., Lewis, M., Pert, C. & Krieger, D. Corticotropin and β-endorphin-like materials are native to unicellular organisms. *Proc. Natl. Acad. Sci. U. S. A.* **79**, 2086-2090 (1982).

141 Csaba, G. The unicellular Tetrahymena as a model cell for receptor research. *Int. Rev. Cytol* **95**, 327-377 (1985).

142 Fenchel, T. & Finlay, B. Respiration rates in heterotrophic, free-living protozoa. *Microb. Ecol.* **9**, 99-122 (1983).

143 Prikhodko, E., Brailovskaya, I., Korotkov, S. & Mokhova, E. Features of mitochondrial energetics in living unicellular eukaryote Tetrahymena pyriformis. A model for study of mammalian intracellular adaptation. *Biochemistry (moscow)* **74**, 371-376 (2009).

144 Conner, R. & Cline, S. Iron deficiency and the metabolism of Tetrahymena pyriformis. *J. Protozool.* **11**, 486-491 (1964).

145 Hamburger, K. & Zeuthen, E. Synchronous divisions in Tetrahymena pyriformis as studied in an inorganic medium: The effect of 2, 4-dinitrophenol. *Exp. Cell Res.* **13**, 443-453 (1957).

146 Kolb-Bachofen, V. & Vogell, W. Mitochondrial proliferation in synchronized cells of Tetrahymena pyriformis: A morphometric study by electron microscopy on the biogenesis of mitochondria during the cell cycle. *Exp. Cell Res.* **94**, 95-105 (1975).

147 Kimura, T., Sato, Y., Kimura, F., Iwasaka, M. & Ueno, S. Micropatterning of cells using modulated magnetic fields. *Langmuir* **21**, 830-832 (2005).

148 Kim, D. H., Cheang, U. K., Kőhidai, L., Byun, D. & Kim, M. J. Artificial magnetotactic motion control of Tetrahymena pyriformis using ferromagnetic nanoparticles: A tool for fabrication of microbiorobots. *Appl. Phys. Lett.* **97**, 173702 (2010).

149 Rifkin, J. L. & Ballentine, R. Magnetic fettering of the ciliated protozoon Tetrahymena pyriformis. *Trans. Am. Microsc. Soc.*, 189-197 (1976).

150 Jeng, H. A. & Swanson, J. Toxicity of metal oxide nanoparticles in mammalian cells. *J. Environ. Sci. Health, Part A: Toxic/Hazard. Subst. Environ. Eng.* **41**, 2699-2711 (2006).

151 Cleffmann, G., Reuter, W. & Seyfert, H. Increase in macromolecular amounts during the cell cycle of Tetrahymena: a contribution to cell cycle control. *J. Cell Sci.* **37**, 117-124 (1979).

152 West, G. B., Woodruff, W. H. & Brown, J. H. Allometric scaling of metabolic rate from molecules and mitochondria to cells and mammals. *Proc. Natl. Acad. Sci. U. S. A.* **99**, 2473-2478 (2002).

153 Shah-Simpson, S., Pereira, C. F., Dumoulin, P. C., Caradonna, K. L. & Burleigh, B. A. Bioenergetic profiling of Trypanosoma cruzi life stages using Seahorse extracellular flux technology. *Mol. Biochem. Parasitol.* **208**, 91-95 (2016).

154 Koopman, M., Michels, H., Dancy, B. M., Kamble, R., Mouchiroud, L., Auwerx, J., Nollen, E. A. & Houtkooper, R. H. A screening-based platform for the assessment of cellular respiration in Caenorhabditis elegans. *Nat. Protoc.* **11**, 1798 (2016).

155 Wu, J., Boström, P., Sparks, L. M., Ye, L., Choi, J. H., Giang, A.-H., Khandekar, M., Virtanen, K. A., Nuutila, P. & Schaart, G. Beige adipocytes are a distinct type of thermogenic fat cell in mouse and human. *Cell* **150**, 366-376 (2012).

156 Nicholls, D. G., Bernson, V. S. & Heaton, G. M. in *Effectors of Thermogenesis* 89-93 (Springer, 1978).

157 Barbatelli, G., Murano, I., Madsen, L., Hao, Q., Jimenez, M., Kristiansen, K., Giacobino, J., De Matteis, R. & Cinti, S. The emergence of cold-induced brown adipocytes in mouse white fat depots is determined predominantly by white to brown

adipocyte transdifferentiation. *American Journal of Physiology-Endocrinology and Metabolism* **298**, E1244 (2010).

158 Himms-Hagen, J., Melnyk, A., Zingaretti, M., Ceresi, E., Barbatelli, G. & Cinti, S. Multilocular fat cells in WAT of CL-316243-treated rats derive directly from white adipocytes. *American Journal of Physiology-Cell Physiology* **279**, C670-C681 (2000).

159 Rosenwald, M., Perdikari, A., Rülicke, T. & Wolfrum, C. Bi-directional interconversion of brite and white adipocytes. *Nature cell biology* **15**, 659 (2013).

160 Lee, Y.-H., Petkova, A. P., Mottillo, E. P. & Granneman, J. G. In vivo identification of bipotential adipocyte progenitors recruited by β3-adrenoceptor activation and high-fat feeding. *Cell metabolism* **15**, 480-491 (2012).

161 Keipert, S. & Jastroch, M. Brite/beige fat and UCP1—is it thermogenesis? *Biochimica et Biophysica Acta (BBA)-Bioenergetics* **1837**, 1075-1082 (2014).

162 Matthias, A., Ohlson, K. B., Fredriksson, J. M., Jacobsson, A., Nedergaard, J. & Cannon, B. Thermogenic responses in brown fat cells are fully Ucp1-dependent UCP2 or UCP3 do not substitute for UCP1 in adrenergically or fatty acid-induced thermogenesis. *Journal of Biological Chemistry* **275**, 25073-25081 (2000).

163 Nedergaard, J. & Cannon, B. UCP1 mRNA does not produce heat. *Biochimica et Biophysica Acta (BBA)-Molecular and Cell Biology of Lipids* **1831**, 943-949 (2013).

164 Shinoda, K., Luijten, I. H., Hasegawa, Y., Hong, H., Sonne, S. B., Kim, M., Xue, R., Chondronikola, M., Cypess, A. M. & Tseng, Y.-H. Genetic and functional characterization of clonally derived adult human brown adipocytes. *Nature medicine* **21**, 389 (2015).

165 Bartelt, A. & Heeren, J. Adipose tissue browning and metabolic health. *Nature Reviews Endocrinology* **10**, 24 (2014).